PURDUE UNIVERSITY
GRADUATE SCHOOL
Thesis Acceptance

This is to certify that the thesis prepared

By Shang-Da Yang

Entitled

Ultrasensitive Nonlinear Optical Pulse Characterizations by Chirped Quasi-phase Matched Lithium Niobate Waveguides

Complies with University regulations and meets the standards of the Graduate School for originality and quality

For the degree of Doctor of Philosophy

Final examining committee members

A. M. Weiner, Chair

V. Shalaev

C.-L. Chen

S. Savikhin

Approved by Major Professor(s): A. M. Weiner

Approved by Head of Graduate Program: V. Balakrishnan

Date of Graduate Program Head's Approval: 7/7/05

ULTRASENSITIVE NONLINEAR OPTICAL PULSE CHARACTERIZATIONS BY CHIRPED QUASI-PHASE MATCHED LITHIUM NIOBATE WAVEGUIDES

A Thesis

Submitted to the Faculty

of

Purdue University

by

Shang-Da Yang

In Partial Fulfillment of the

Requirements for the Degree

of

Doctor of Philosophy

August 2005

This thesis is dedicated to my parents: Yi-Hsin Yang and Hsueh-E Weng, who educated me how to appreciate the beauty of life.

ACKNOWLEDGMENT

First thank to the precious peace of this era, which permits all my study and work. I would especially like to thank my thesis advisor, Prof. Andrew M. Weiner, for his patience and guidance, which erect an excellent model of leadership. His generous support enables my studying journey in this prestigious school, enriching my life with insight and perspective.

I am also indebted to all the people who directly contributed to my research work: Dr. Krishnan R. Parameswaran (JDS Uniphase), Zhi Jiang, Dr. Daniel E. Leaird, Prof. Martin M. Fejer (Stanford University), Prof. Kevin J. Webb, Rostislav V. Roussev (Stanford University), Jung-Ho Chung, Dr. Zheng Zheng, Dr. Riccardo Fanciulli, and Chuck Harrington. Without their help, I would have not accomplished such an impressive result.

Finally, I appreciate all the friends I made in Purdue. They turn the campus surrounded by cornfields into another lovely hometown.

TABLE OF CONTENTS

Page

Page

LIST OF TABLES

LIST OF FIGURES

Figure Page

Figure Page

LIST OF ABBREVIATIONS

Abbreviation	**Interpretation**
APE	Annealed proton exchange
A-PPLN	Aperiodically poled lithium niobate
BW	Bandwidth
CCD	Charge-coupled device
CW	Continuous-wave
DAQ	Data acquisition
DSF	Dispersion-shifted fiber
FH	Fundamental-harmonic
FIR	Finite-duration impulse response
FROG	Frequency-resolved optical gating
FWHM	Full-width at half-maximum
FWM	Four-wave mixing
GaAs	Gallium arsenide
GRENOUILLE	Grating-eliminated no-nonsense observation of ultrafast incident laser light E-fields
GVD	Group velocity dispersion
GVM	Group velocity mismatch
IAC	Interferometric autocorrelation
InGaAsP	Indium gallium arsenide phosphide
$LiIO_3$	Lithium iodate
$LiNbO_3$	Lithium niobate
LPF	Low-pass filtering
MEFISTO	Measurement of electric field by interferometric spectral trace observation
MI	Michelson interferometer
O-CDMA	Optical code-division multiple-access
OPA	Optical parametric amplification
OSA	Optical spectrum analyzer

Abbreviation	Interpretation
PM	Phase-matching
PMT	Photomultiplier tube
PPLN	Periodically-poled lithium niobate
PZT	Piezoelectric transducer
QPM	Quasi-phase matching
RPE	Reverse proton exchange
RZ	Return-to-zero
SH	Second-harmonic
SHG	Second-harmonic generation
Si:APD	Silicon avalanche photodiode
SMF	Single-mode fiber
SNR	Signal-to-noise ratio
SOA	Semiconductor optical amplifier
SPIDER	Spectral interferometry for direct electric-field reconstruction
SPM	Self-phase modulation
SVEA	Slowly varying envelope approximation
TADPOLE	Temporal analysis by dispersing a pair of light e fields
TPA	Two-photon absorption
WDM	Wavelength division multiplexing

ABSTRACT

Yang, Shang-Da Ph.D., Purdue University, August 2005. Ultrasensitive Nonlinear Optical Pulse Characterizations by Chirped Quasi-phase Matched Lithium Niobate Waveguides. Major Professor: Andrew M. Weiner.

We have realized ultra-sensitive self-referenced nonlinear measurements of subpicosecond optical pulses in the lightwave communication band by using chirped quasi-phase matched (QPM) lithium niobate waveguides. The tightly confined optical beam in the long waveguides and the chirped QPM grating period simultaneously enable high second-harmonic generation (SHG) efficiency and broad SHG phase-matching bandwidth, which are essential for sensitive and accurate pulse measurements. Our experiments of intensity autocorrelation measurement achieve a record sensitivity of **0.32 microwatt square**, about **500** times better than the previous record. We also employed the SHG frequency-resolved optical gating (FROG) technique to completely retrieve intensity and phase of the unknown pulses. The resulting sensitivity is **2.7 microwatt square**, greatly improving on the previous record for FROG schemes by **75,000** times. Our work significantly contributes to system monitoring in ultrafast lightwave communications, nonlinear optical material characterizations, and other experiments using shaped ultrashort optical pulses.

1. INTRODUCTION

The comprehensive applications of ultrafast optics largely rely on the ability of characterizing the ultrashort (10^{-12}~10^{-15} s) signal pulses, especially when nearly bandwidth-limited or precisely shaped pulses are involved, such as those in the high bit-rate telecommunication transmissions [1], optical code-division multiple-access (O-CDMA) systems [2-3], and nonlinear-optical material characterizations [4]. However, measurements of these ultrashort optical pulses are challenging, since the temporal durations of interest are much shorter than any available electronic response. Although Dorrer et. al. demonstrated that longer (30 ps = $30 \bullet 10^{-12}$ s) electronic gating pulse is able to characterize shorter (>2.7 ps) optical signal pulse through iterative retrieval from linear spectrogram traces [5-7], this technique remains inapplicable to ultrashort regime, and requires high-speed (>10 GHz) electronics even in measuring pulses with repetition rate in the order of KHz~MHz. As a result, all-optical techniques using quasi-instantaneous nonlinearities of optical media, such as second-harmonic generation (SHG), two-photon absorption (TPA), and four-wave mixing (FWM), are normally employed to perform optical gating and retrieve the pulse information. Since the nonlinear signal yield diminishes rapidly with the input signal, conventional all-optical nonlinear measurements using bulk crystals are usually insufficient to meet the requirements of limited power budget in optical communication systems and weak signal pulse energy ($<10^{-15}$ J) in material characterizations.

Several sensitive schemes have been proposed to characterize ultraweak optical pulses. The TADPOLE technique has been demonstrated to measure near-infrared signal pulses as weak as 42 zeptojoule ($42 \bullet 10^{-21}$ J) per shot [8], and optical parametric amplification (OPA) cross-correlation frequency-resolved optical gating (X-FROG) permits measurement of sliced white-light continuum pulses around 600-nm wavelength

at 50 attojoule ($50 \bullet 10^{-18}$ J) [9]. The primary limitations of these heterodyne techniques are twofold. First, they require synchronized reference pulses with known intensity/phase profiles and a temporal duration shorter than that of the signal pulses. In some important cases, such as weak pulses at the intermediate or receiving ends of an optical communication link, the required reference is often unavailable. Second, the overall power requirement is actually limited by the sensitivity of the self-referenced measurement scheme used to fully characterize the reference pulses. Therefore, it is more desirable to investigate self-referenced schemes in terms of exploring the limit of measurement sensitivity.

Intensity autocorrelation and FROG measurements utilizing SHG in bulk crystals [10] are widely used in characterizing pulse durations and intensity/phase profiles of ultrashort pulses without the requirement for a reference. Nonetheless, the attainable SHG conversion efficiency is restricted in part by Gaussian beam diffraction, which prevents the coexistence of a small beam cross-sectional area and a long interaction length [10]. When ultrashort pulses are involved, the broad input spectrum should be phase-matched (PM) to avoid distortion of autocorrelation traces [11], and the spectral truncation in FROG spectrograms [12]. Since the SHG PM bandwidth (BW) is inversely proportional to the group velocity mismatch (GVM) walkoff (which is the product of interaction length and GVM between fundamental and second-harmonic waves), thin nonlinear crystals are typically employed (e.g., thickness of $LiNbO_3$ should be less than 1 mm when measuring 300-fs pulses at 1.55-μm band), further limiting the nonlinear conversion efficiency. As a result, bulk SHG crystals offer quadratic sensitivities (defined as the minimum peak-power average-power product needed to generate a detectable nonlinear signal, see Sec. 2.2.3) of ~1 mW^2 for intensity autocorrelation and ~500 mW^2 for SHG FROG, respectively [13, 1].

Extensive efforts have been made to improve the sensitivities of intensity autocorrelation and FROG measurements. Several recent intensity autocorrelation experiments at 1.55-μm wavelength have exploited broadband TPA in silicon avalanche photodiodes (Si:APD) [14], GaAs photomultiplier tubes (PMT) [15], and InGaAsP laser diodes [16]. Measurement sensitivity as low as $\mathbf{1.5 \bullet 10^{-4}\ mW^2}$ has been reported [16],

which is approximately four orders of magnitude better than that obtained with conventional bulk SHG crystals. On the other hand, FWM in a semiconductor optical amplifier (SOA) and in a spool of 22-km-long dispersion-shifted fiber (DSF) have been employed to realize quadratic FROG measurements with record sensitivities of 50 mW^2 and **0.2 mW^2**, respectively [17-18]; improving on the conventional SHG FROG measurements using bulk crystals by 1-3 orders of magnitude. Despite the impressive progresses, the resulting sensitivities of these TPA and FWM approaches still do not meet the requirement for μW-order average powers for 10-Gbit/sec optical communication system monitoring [19].

In this dissertation, we further the intensity autocorrelation and SHG FROG measurements using long quasi-phase-matched (QPM) $LiNbO_3$ waveguides, which permit extremely high SHG efficiency by confining the optical beam within a small area over a long propagation distance [20]. By longitudinally chirping the poling period of the waveguides (aperiodically poled lithium niobate, or A-PPLN) [21], we can controllably broaden the PM BW to circumvent measurement distortion. Furthermore, this spectral broadening can be achieved without substantially sacrificing SHG efficiency of short pulses (see Sec. 3.3) [22]. As a consequence, we greatly push the measurement sensitivities of intensity autocorrelation and SHG FROG down to **$3.2 \cdot 10^{-7}$ mW^2** [22] and **$2.7 \cdot 10^{-6}$ mW^2** [23-24], improving upon previous records [16, 18] by **500** and **75,000** times, respectively (see Tab. 1-2). The QPM $LiNbO_3$ waveguide technique has seen some applications in optical communications with unprecedented low-power requirements, such as chromatic dispersion monitoring for ultrashort pulse transmission (**-45 dBm** for 10-GHz pulse train, see Sec. 3.2) [25-26], and nonlinear waveform discrimination in O-CDMA system (30 fJ/bit for four-user, 10-Gbit/s system) [3]. The complete intensity/phase retrieval in collaboration with the Fourier transform pulse shaper technique [27-28] can accomplish a dynamic optical signal processor, which would be very desirable for a wide range of applications in communications [29], coherent control over quantum-mechanical systems [30], and ultrafast spectroscopy [4].

Table 1.1
Intensity autocorrelation measurement sensitivities achieved by different schemes. SHG: second-harmonic generation, TPA: two-photon absorption.

Autocorrelation scheme	**Sensitivity** (mW^2)	**Reference**
Bulk crystal, SHG	~1	
Silicon avalanche photodiode, TPA	$1.5 \cdot 10^{-3}$	[14]
GaAs photomultiplier tube, TPA	$1.7 \cdot 10^{-4}$	[15]
InGaAsP laser diode, TPA	$1.5 \cdot 10^{-4}$	[16]
Chirped QPM $LiNbO_3$ waveguide, SHG	$3.2 \cdot 10^{-7}$	[22]

Table 1.2
FROG measurement sensitivities achieved by different schemes. SHG: second-harmonic generation, FWM: four-wave mixing.

FROG scheme	**Sensitivity** (mW^2)	**Reference**
Bulk crystal, SHG	~500	[1]
Semiconductor optical amplifier, FWM	50	[17]
22-km dispersion shifted fiber, FWM	0.2	[18]
Chirped QPM $LiNbO_3$ waveguide, SHG	$2.7 \cdot 10^{-6}$	[24]

2. THEORY OF NONLINEAR OPTICAL PULSE CHARACTERIZATIONS

As discussed in Chapter 1, optical gating through some nonlinear process is usually required to characterize sub-picosecond optical pulses, where SHG is mostly employed because of the self-referenced nature and better efficiency. In this chapter, we will first examine the theory of continuous-wave (CW) and pulsed SHG within the extent of certain assumptions valid throughout our experimental studies. The relation between the SHG yield and the chirp of input pulse will be discussed next, which is applicable to chromatic dispersion monitoring. By introducing a variable delay between two replicas of the input pulse, we are able to formulate SHG intensity autocorrelation measurements, which is sufficient to provide a reasonable estimation of pulse durations with an uncertainty of ~10% (provided that the pulse shape is well behaved) [10]. Additional efforts will be made to investigate the relation between the intensity autocorrelation trace and the PM BW of the SHG medium. The result will address the necessity of using chirped QPM devices in our experiments to obtain accurate intensity autocorrelation traces. Finally, we will discuss the conventional SHG FROG theory, which consists of spectrally resolving the nonlinear output signal for each delay, and iterative retrieval algorithm.

2.1 Second-harmonic Generation

2.1.1 Notations and definitions

The notation and general approach that are used here are similar to [10]. We start with some notations and definitions going to be used throughout this dissertation. The scalar electric field of an optical pulse is expressed as:

$$e(t) \equiv \mathrm{Re}\left\{ a(t)\cdot \mathrm{e}^{j\omega_0 t} \right\} = \frac{1}{2}\left\{ a(t)\cdot e^{j\omega_0 t} + a^*(t)\cdot e^{-j\omega_0 t} \right\} \tag{2.1}$$

where $a(t) \equiv |a(t)|\cdot \exp[j\phi_a(t)]$ is the complex field envelope, and ω_0 is the carrier angular frequency. The fringe-resolved instantaneous power is proportional to $e^2(t)$:

$$e^2(t) \propto |a(t)|^2 \cdot [1+\cos(2\omega_0 t + 2\phi_a(t))] \tag{2.2}$$

In most cases of interest where slowly varying envelope approximation (SVEA) holds, the pulse envelope covers a large number of carrier cycles (say 60 cycles for a 300-fs pulse at 1.55-μm wavelength), the fast oscillating carrier in eq. (2.2) is unimportant, and we normally use $|a(t)|^2$ to represent the power averaged over one carrier cycle:

$$P(t) \propto |a(t)|^2 \tag{2.3}$$

Since $P(t)$ remains "instantaneous" in terms of pulse envelope, it will be referred as "instantaneous power" without further explanation. Because currently available optical-to-electrical (O/E) converters (BW<100 GHz) are generally much slower than the ultrashort pulse durations, they only detect pulse energy or the power averaged over one repetition period T_{rep}:

$$U \propto \int_{-\infty}^{\infty} |a(t)|^2 dt \text{, or } \overline{P} \propto \int_{T_{rep}} |a(t)|^2 dt \tag{2.4}$$

For simplicity, $\overline{P}$ will be referred as "averag power" in the subsequent text.

The electric field spectrum is derived by the Fourier transform of $e(t)$:

$$E(\omega) = F_t\{e(t)\} = \frac{1}{2}\left\{ A(\omega-\omega_0) + A^*(-\omega-\omega_0) \right\} \tag{2.5}$$

where $A(\omega) \equiv F_t\{a(t)\}$ is the field envelope spectrum. If SVEA is met, the carrier frequency ω_0 would be much higher than the BW of $A(\omega)$, and the overlap between the two components in eq. (2.5) becomes negligible. The power spectrum can be approximated as:

$$|E(\omega)|^2 \approx \frac{1}{4}\left\{ |A(\omega-\omega_0)|^2 + |A(-\omega-\omega_0)|^2 \right\} \tag{2.6}$$

In the future, we will use the baseband power spectral envelope $|A(\omega)|^2$ in most formulations.

In characterizing pulse duration and spectral BW, we will normally use full-width at half-maximum (FWHM) of intensity envelope $|a(t)|^2$ and power spectrum $|A(\omega)|^2$, denoted as Δt and Δf ($\equiv\Delta\omega/2\pi$), respectively. Since the FWHM neglects all the information outside the mainlobe, root-mean-square (rms) measures are more appropriate when pulse wings become appreciable.

2.1.2 CW SHG

We focus on the cases obeying the following assumptions: (i) the medium in which optical waves propagate is source-free, nonmagnetic, homogeneous, and isotropic for linear properties; (ii) nonlinear polarization is only a perturbation to the system; (iii) both electric field and nonlinear polarization are scalar plane waves; (iv) SVEA holds. As a result, the forced wave equation governing the electric field $E(z,t)$ propagation in the presence of nonlinear polarization $P_{NL}(z,t)$ is [10, 31]:

$$\frac{\partial^2}{\partial z^2}E(z,t)-\mu_0\varepsilon_{(1)}\frac{\partial^2}{\partial t^2}E(z,t)=\mu_0\frac{\partial^2}{\partial t^2}P_{NL}(z,t) \tag{2.7}$$

where $\varepsilon_{(1)}$ represents the linear dielectric constant of the medium (propagation constant $k(\omega)=\omega\sqrt{\mu_0\varepsilon_{(1)}(\omega)}$). For simplicity, we define the complex envelopes $a(z,t)$, $p_{NL}(z,t)$ of the real fields $E(z,t)$, $P_{NL}(z,t)$ as:

$$E(z,t)\equiv\frac{1}{2}\left\{a(z,t)\cdot\exp\left[j\left(\omega_0 t-k_0 z\right)\right]+c.c.\right\} \tag{2.8}$$

$$P_{NL}(z,t)\equiv\frac{1}{2}\left\{p_{NL}(z,t)\cdot\exp\left[j\left(\omega_0 t\right)\right]+c.c.\right\} \tag{2.9}$$

from which eq. (2.7) is transformed into:

$$\frac{\partial}{\partial z}a(z,t)+k_0'\frac{\partial}{\partial t}a(z,t)=-j\frac{\mu_0\omega_0^2}{2k_0}p_{NL}(z,t)\cdot e^{jk_0 z} \tag{2.10}$$

where the propagation constant $k(\omega)$ is approximated as (neglecting GVD effect):

$$k(\omega)\approx k(\omega_0)+\left(\left.\frac{\partial k}{\partial\omega}\right|_{\omega_0}\right)\cdot\left(\omega-\omega_0\right)\equiv k_0+k_0'\cdot\tilde{\omega} \tag{2.11}$$

Considering a CW plane wave $E(z,t)$ consisting of two frequency components of ω_o and $2\omega_o$ propagating through an SHG crystal of length L:

$$E(z,t) = \frac{1}{2}\left\{E_\omega(z)\cdot e^{j(\omega_0 t - k_\omega z)} + E_{2\omega}(z)\cdot e^{j(2\omega_0 t - k_{2\omega} z)} + c.c.\right\} \tag{2.12}$$

where E_ω, $E_{2\omega}$, k_ω, $k_{2\omega}$ correspond to complex field amplitudes (time-independent envelopes) and propagation constants at ω_o, $2\omega_o$, respectively. The quadratic nonlinear polarization $P_{NL}(z,t)$ induced by $E(z,t)$ is written as [10]:

$$P_{NL}(z,t) = 2\varepsilon_0 d_{eff}\cdot E^2(z,t) \tag{2.13}$$

in which the effective nonlinear coefficient d_{eff} is determined by the field polarizations and the $\chi^{(2)}$-tensor of the SHG medium. Substituting eq. (2.12) into eq. (2.13), and extracting complex envelopes from real fields according to equations (2.8-9), we derive two nonlinear polarization components driving waves at the frequencies of ω_o, $2\omega_o$, respectively:

$$p_{NL,\omega}(z,t) \approx 2\varepsilon_0 d_{eff}\cdot E_{2\omega}(z)\cdot E_\omega^*(z)e^{j(k_{2\omega}-k_\omega)z} \tag{2.14}$$

$$p_{NL,2\omega}(z,t) \approx \varepsilon_0 d_{eff}\cdot E_\omega^2(z)e^{-j2k_\omega z} \tag{2.15}$$

Substituting equations (2.14-15) into eq. (2.10) gives rise to a system of coupled equations:

$$\frac{\partial E_\omega}{\partial z} = -j\frac{\omega_0 d_{eff}}{n_\omega c}E_{2\omega}E_\omega^*\cdot e^{-j(\Delta k)z} \tag{2.16}$$

$$\frac{\partial E_{2\omega}}{\partial z} = -j\frac{\omega_0 d_{eff}}{n_{2\omega} c}E_\omega^2\cdot e^{j(\Delta k)z} \tag{2.17}$$

where

$$\Delta k \equiv k_{2\omega} - 2k_\omega \tag{2.18}$$

is the phase mismatch between the fundamental-harmonic (FH) and second-harmonic (SH) waves, and $n_\omega \equiv n(\omega_o)$, $n_{2\omega} \equiv n(2\omega_o)$ correspond to their refractive indexes. The coupled system can be simplified when FH pump is non-depleted (i.e. $E_\omega(z) \approx E_\omega(0)$):

$$\frac{\partial}{\partial z}E_{2\omega}(z) = -j\kappa d_{eff}E_\omega^2(0)\cdot e^{j(\Delta k)z}, \qquad \kappa \equiv \frac{\omega_0}{n_{2\omega}c} \tag{2.19}$$

Solution to eq. (2.19) elucidates the key concepts of CW SHG with non-depleted pump:

(a) Perfect phase-matching (Δk=0):

The right hand side of eq. (2.19) becomes a constant, and integration of eq. (2.19) with respect to z produces a linear function:

$$E_{2\omega}(z) = -j\kappa d_{eff} E_{\omega}^{2}(0) \cdot z \tag{2.20}$$

which implies that SH intensity grows quadratically with the interaction distance L:

$$I_{2\omega}(L) = \frac{1}{2}\varepsilon_0 c n_{2\omega} \left|E_{2\omega}(L)\right|^2 = \Gamma^2 L^2 I_{\omega}^2, \qquad \Gamma^2 \equiv \frac{2\omega_0^2 d_{eff}^2}{\varepsilon_0 c^3 n_{2\omega} n_{\omega}^2} \tag{2.21}$$

CW SHG efficiency is normally defined as the intensity ratio between SH and FH waves:

$$\eta_{SHG} \equiv \frac{I_{2\omega}}{I_{\omega}} = \Gamma^2 L^2 I_{\omega} = \Gamma^2 \left(\frac{L^2}{A_{eff}}\right) \overline{P}_{\omega} \tag{2.22}$$

where A_{eff} is the effective beam cross-sectional area, and $\overline{P}_{\omega}$ is the average FH power. As a result, one usually uses the SHG efficiency normalized to average FH power ($\eta_{SHG}/\overline{P}_{\omega}$) in the unit of %/W to characterize the CW conversion efficiency of a nonlinear media (with fixed Γ, A_{eff}, and L, e.g. our QPM $LiNbO_3$ waveguide). Eq. (2.22) also addresses the universal requirements for efficient SHG: high input power $\overline{P}_{\omega}$, small beam size A_{eff}, and long interaction length L; though the scales may change when the CW plane wave approximation is violated [10].

(b) Phase mismatch ($\Delta k \neq 0$):

Directly integrating eq. (2.19) from z=0 to z=L results in:

$$E_{2\omega}(L) = -j\left(\frac{2\kappa d_{eff}}{\Delta k}\right) E_{\omega}^{2}(0) \cdot \sin\left(\frac{\Delta k \cdot L}{2}\right) \cdot e^{j\left(\frac{\Delta k L}{2}\right)} \tag{2.23}$$

$$\eta_{SHG} \equiv \frac{I_{2\omega}(L)}{I_{\omega}} = \Gamma^2 L^2 I_{\omega} \cdot \mathrm{sinc}^2\left(\frac{\Delta k \cdot L}{2}\right) \tag{2.24}$$

where $\mathrm{sinc}(x) \equiv \sin(x)/x$. One can visualize the importance of phase-matching by Fig. 2.1, in which SHG efficiencies η_{SHG} versus normalized interaction length L/l_c ($l_c \equiv \pi/\Delta k$) are plotted for both Δk=0 (solid) and $\Delta k \neq 0$ (dashed) cases. The latter shows that the

direction of energy conversion reverses in every coherence length l_c, therefore, prevents the continuous growth of SH power. Eq. (2.24) suggests that SHG efficiency arising from a fixed interaction length L is critically damped by a $sinc^2$ function of Δk. This further highlights the necessity of PM in achieving highly efficient SHG.

2.1.3 Pulsed SHG

From equations (2.22, 24), we know that SHG efficiency scales linearly with the input FH intensity I_ω. Short pulse with large peak intensity is thus preferable to CW source in terms of stronger SHG yield. We will simply address key formulations of pulsed SHG without pump depletion and spatial walkoff [10, 21]. A more detailed analysis is referred to [32].

The forced wave equation in frequency domain is derived by taking Fourier transform of eq. (2.7):

$$\frac{\partial^2}{\partial z^2}\tilde{E}(z,\omega)+\mu_0\varepsilon_{(1)}\omega^2\tilde{E}(z,\omega)=-\mu_0\omega^2\tilde{P}_{NL}(z,\omega) \tag{2.25}$$

where $\tilde{E}(z,\omega)$, $\tilde{P}_{NL}(z,\omega)$ are complex spectra of $E(z,t)$, $P_{NL}(z,t)$, respectively. For simplicity, we separate the positive and negative frequency components:

$$\tilde{E}(z,\omega)\equiv\frac{1}{2}\left\{\varepsilon(z,\omega)e^{-jk(\omega)z}+\varepsilon^*(z,-\omega)e^{jk(-\omega)z}\right\} \tag{2.26}$$

$$\tilde{P}_{NL}(z,\omega)\equiv\frac{1}{2}\left\{P_{NL}(z,\omega)+P^*_{NL}(z,-\omega)\right\} \tag{2.27}$$

In this way, the linear medium dispersion has been considered by the term $exp[-jk(\omega)z]$, and $\varepsilon(z,\omega)$ represents the pulse evolution due to nonlinearity. By using equations (2.26-27) and SVEA, eq. (2.25) can be simplified as:

$$\frac{\partial}{\partial z}\varepsilon(z,\omega)\approx -j\frac{\omega\mu_0 c}{2n(\omega)}P_{NL}(z,\omega)e^{jk(\omega)z} \tag{2.28}$$

Eq. (2.28) is the frequency-domain counterpart of eq. (2.10), except that the frequency-domain approach takes GVD effect into account.

By assuming the FH pump is non-depleted, and expressing the spectrum of nonlinear polarization driving SH field with the integral relation (frequency-domain analogy to eq. (2.15)):

$$P_{NL,2\omega}(z,\Omega) = \varepsilon_0 d_{eff} \cdot \left\{\left(\varepsilon_\omega e^{-jkz}\right) \otimes \left(\varepsilon_\omega e^{-jkz}\right)\right\} \tag{2.29}$$

$$= \varepsilon_0 d_{eff} \left\{\int_{-\infty}^{\infty} \varepsilon_\omega(\Omega-\omega')\varepsilon_\omega(\omega') e^{-j[k(\Omega-\omega')+k(\omega')]z} d\omega'\right\}$$

eq. (2.28) results in a de-coupled equation governing the SH field evolution:

$$\frac{\partial}{\partial z}\varepsilon_{2\omega}(z,\Omega) \approx -j\kappa d_{eff} \left\{\int_0^{\infty} \varepsilon_\omega(\omega')\varepsilon_\omega(\Omega-\omega') e^{j\Delta k(\Omega,\omega')z} d\omega'\right\} \tag{2.30}$$

where κ is defined in eq. (2.19). The phase mismatch factor is defined as:

$$\Delta k(\Omega,\omega') = k(\Omega) - k(\omega') - k(\Omega-\omega') \tag{2.31}$$

which is a function of both Ω (SH band) and ω′ (FH band) in general. By integrating eq. (2.30) from *z*=-*L/2* to *z*=*L/2* (equivalent to *z*=[*0*, *L*] except for an unimportant linear phase; while the output position is still denoted as *z*=*L* for convenience), we can express the SH spectrum at the output of a crystal with length *L* as:

$$\varepsilon_{2\omega}(L,\Omega) \approx -j\kappa \left\{\int_0^{\infty} \varepsilon_\omega(\omega')\varepsilon_\omega(\Omega-\omega') \left[d_{eff} L \cdot \mathrm{sinc}\left(\frac{\Delta k \cdot L}{2}\right)\right] d\omega'\right\} \tag{2.32}$$

where the nonlinear coefficient d_{eff} is assumed to be *z*-independent. If the GVD effect is negligible, $\Delta k(\Omega,\omega')$ reduces to a function of Ω:

$$\Delta k(\Omega,\omega') \approx \Delta k + \Delta\left(v_g^{-1}\right)\cdot(\Omega - 2\omega_0) \equiv \Delta k(\Omega) \tag{2.33}$$

where the carrier phase mismatch Δk is defined in eq. (2.18), and

$$\Delta\left(v_g^{-1}\right) \equiv k'_{2\omega} - k'_{\omega} \tag{2.34}$$

characterizes the group velocity mismatch (GVM) between FH and SH pulses. The ω'-independent phase mismatch due to the negligible GVD separates the contributions of input FH field and nonlinear medium in SHG process:

$$\varepsilon_{2\omega}(L,\Omega) \approx -j\kappa\{\varepsilon_\omega \otimes \varepsilon_\omega(\Omega)\}\cdot\{H_{2\omega}(\Omega)\} \tag{2.35}$$

$$H_{2\omega}(\Omega) = d_{eff} L \cdot \mathrm{sinc}\left(\frac{T_s[\Omega - 2\omega_0 - \delta]}{2}\right) \tag{2.36}$$

where ⊗ means convolution. The GVM walkoff T_s within the SHG crystal, and the frequency detuning δ of $H_{2\omega}(\Omega)$ due to carrier phase mismatch ($\Delta k \neq 0$) are defined as:

$$T_s \equiv \Delta\left(v_g^{-1}\right)L \tag{2.37}$$

$$\delta \equiv -\frac{\Delta k}{\Delta\left(v_g^{-1}\right)} \tag{2.38}$$

Fig. 2.2 visualizes the spectral manipulations in equations (2.35-36) (assume zero detuning δ=0). The output SH spectrum $\varepsilon_{2\omega}(L,\Omega)$ is simply the product of input FH spectral autoconvolution $\varepsilon_\omega \otimes \varepsilon_\omega(\Omega)$, and PM spectrum $H_{2\omega}(\Omega)$ (both are centered at $2\omega_o$). In Fig. 2.2a, the autoconvolution term implies that each SH frequency component Ω is actually driven by various combinations of FH frequency pairs ω' and $\Omega - \omega'$, instead of solely by Ω/2. Fig. 2.2b shows that only frequency components Ω's satisfying $|\Omega - 2\omega_o| \leq 2\pi/T_s \equiv \Delta\omega_{PM}/2$ are well phase-matched by the crystal. As a result, the output SH spectrum $\varepsilon_{2\omega}(L,\Omega)$ could be distorted from the ideal $\varepsilon_\omega \otimes \varepsilon_\omega(\Omega)$ if the PM BW ($\Delta\omega_{PM}$) of $H_{2\omega}(\Omega)$ is narrower than the BW of $\varepsilon_\omega \otimes \varepsilon_\omega(\Omega)$ ($\Delta\omega_{NLP}$, not FH spectral width $\Delta\omega$).

The baseband representation of eq. (2.35) turns out to be:

$$A_{2\omega}(L,\omega) = -j\kappa \cdot P_{NL}(\omega) \cdot H(\omega) \tag{2.39}$$

where

$$A_{2\omega}(L,\omega) \equiv \varepsilon_{2\omega}(L,\omega + 2\omega_0), \quad A_\omega(\omega) \equiv \varepsilon_\omega(\omega + \omega_0);$$

$$P_{NL}(\omega) \equiv \left(A_\omega \otimes A_\omega\right)(\omega) \tag{2.40}$$

$$H(\omega) \equiv d_{eff} L \cdot \mathrm{sinc}\left[T_s(\omega - \delta)/2\right] \tag{2.41}$$

The corresponding SH pulse energy $U_{2\omega}$ and average power $\overline{P}_{2\omega}$ can be derived by power spectral integration of eq. (2.39):

$$\overline{P}_{2\omega} \equiv \left(U_{2\omega}/T_{rep}\right) \propto \int_{-\infty}^{\infty} \left|A_{2\omega}(L,\omega)\right|^2 d\omega = \int_{-\infty}^{\infty} \left|P_{NL}(\omega)\right|^2 \cdot \left|H(\omega)\right|^2 d\omega \tag{2.42}$$

where T_{rep} is the repetition period of the pulse train. Equations (2.39-41) are the governing equations normally used to characterize pulsed SHG under the assumptions of: (i) uniform nonlinear coefficient d_{eff}, (ii) negligible GVD effect, (iii) non-depleted pump.

Modifications of PM response $H(\omega)$ due to spatially dependent $d_{eff}(z)$ will be discussed in Sec. 3.1.

The waveform and energy of SH pulse highly depend on the PM BW of the SHG crystal. We simply demonstrate this fact by investigating three special cases illustrated in Fig. 2.3 (assuming zero frequency detuning δ=0 for simplicity):

(a) Extremely broad PM BW ($\Delta\omega_{PM}$>>$\Delta\omega_{NLP}$):

This case normally takes place in conventional SHG using thin birefringence bulk crystals. As shown in Fig. 2.3a, the narrowband nonlinear polarization spectrum $P_{NL}(\omega)$ only interacts with the PM spectrum around its peak $H(0)$, where the amplitude and phase of $H(\omega)$ are nearly constant within the band of interest ($|\omega|$<$\Delta\omega_{NLP}/2$):

$$A_{2\omega}(L,\omega) \approx -j\kappa P_{NL}(\omega)H(0) = -j\kappa L d_{eff} P_{NL}(\omega) \tag{2.43}$$

$$a_{2\omega}(L,t) \equiv F_{\omega}^{-1}\{A_{2\omega}(L,\omega)\} = -j\kappa L d_{eff} a_{\omega}^2(t), \quad I_{2\omega}(L,t) = \Gamma^2 L^2 I_{\omega}^2(t) \tag{2.44}$$

where Γ is defined in eq. (2.21). As a result, the complex field and intensity envelopes of output SH pulse are just the square of their input FH counterparts.

The SH pulse energy $U_{2\omega}$ ($\propto$ average power $\overline{P}_{2\omega}$) detected by a slow power meter can be characterized as:

$$U_{2\omega} = A_{eff}\left(\int I_{2\omega}(L,t)dt\right) = A_{eff}\Gamma^2 L^2\left(\int I_{\omega}^2(t)dt\right) = A_{eff}\Gamma^2 L^2 \frac{\left(\int I_{\omega}(t)dt\right)^2}{\Delta t_{eff}} = \frac{\Gamma^2 L^2 U_{\omega}^2}{A_{eff}\cdot\Delta t_{eff}} \tag{2.45}$$

$$\overline{P}_{2\omega} \equiv \frac{U_{2\omega}}{T_{rep}} = \Gamma^2\left(\frac{L^2}{A_{eff}}\right)\cdot\left(\hat{P}_{\omega}\cdot\overline{P}_{\omega}\right) \tag{2.46}$$

where A_{eff} indicates the effective cross-sectional area of both FH and SH beams, $\hat{P}_{\omega}, \overline{P}_{\omega}$ represent the peak and average FH powers, and Δt_{eff} is the effective FH pulse duration defined as:

$$\Delta t_{eff} \equiv \left(\int I_{\omega}(t)dt\right)^2 \Big/ \left(\int I_{\omega}^2(t)dt\right) \tag{2.47}$$

Eq. (2.46) implies that to generate some detectable average SH power $\overline{P}_{2\omega}$, lower requirement of FH peak power – averaged power product $\left(\hat{P}_{\omega}\cdot\overline{P}_{\omega}\right)$ corresponds to

better detection sensitivity. This justifies the widely used definition of quadratic measurement sensitivity:

$$S \equiv \left(\hat{P}_\omega \cdot \overline{P}_\omega\right) \tag{2.48}$$

The pulsed SHG efficiency is usually defined as the ratio between the FH and SH pulse energies:

$$\eta_{SHG} \equiv \frac{U_{2\omega}}{U_\omega} = \Gamma^2\left(\frac{L^2}{A_{eff}}\right)\hat{P}_\omega = \Gamma^2\left(\frac{L^2}{A_{eff}}\right)\overline{P}_\omega \cdot \left(\frac{T_{rep}}{\Delta t_{eff}}\right) \tag{2.49}$$

Comparing eq. (2.49) with eq. (2.22), we found that short pulse enhances the SHG efficiency by a large factor of $T_{rep}/\Delta t_{eff}$ over that of CW source. SHG efficiency normalized to peak FH power ($\eta_{SHG}/\hat{P}_\omega$) in the unit of **%/W** can be used to characterize the efficiency of extremely broadband ($\Delta\omega_{PM} >> \Delta\omega_{NLP}$) nonlinear media. Moreover, chirped pulses generate less SH power, for the non-uniform spectral phase profile broadens the pulse width Δt_{eff} and reduces the peak power $\hat{P}_\omega$.

(b) Extremely narrow PM BW ($\Delta\omega_{PM} << \Delta\omega_{NLP}$):

This case usually happens when thick nonlinear crystals are used in pulsed SHG (assuming the optical beam does not diverge during the propagation). As shown in Fig. 2.3b, SH spectrum $A_{2\omega}(L,\omega)$ is dominated by the narrow PM response $H(\omega)$ of the crystal, instead of the nonlinear polarization $P_{NL}(\omega)$ caused by the input FH pulse:

$$A_{2\omega}(L,\omega) \approx -j\kappa \cdot P_{NL}(0) \cdot H(\omega) \tag{2.50}$$

$$a_{2\omega}(L,t) = -j\frac{\kappa d_{eff} P_{NL}(0)}{\Delta\left(v_g^{-1}\right)}\Pi\left(\frac{t}{T_s}\right), \quad I_{2\omega}(L,t) = s \cdot \frac{\left|P_{NL}(0)\right|^2}{\left[\Delta\left(v_g^{-1}\right)\right]^2}\Pi\left(\frac{t}{T_s}\right) \tag{2.51}$$

where $s \equiv \left(\varepsilon_o \omega_o^2 d_{eff}^2 / 2cn_{2\omega}\right)$, and the square function $\Pi(x)$ is defined as:

$$\Pi(x) = 1, \text{ for } |x| \le \frac{1}{2}; = 0, \text{otherwise} \tag{2.52}$$

Eq. (2.51) indicates that the shape of output SH pulse is always square with a duration T_s, regardless of the input FH pulse.

The input field $a_\omega(t)$, however, can influence the output SH intensity $I_{2\omega}(L,t)$ and pulse energy $U_{2\omega}$ through $P_{NL}(0)=\int a_\omega^2(t)dt$:

$$U_{2\omega}(\propto \overline{P}_{2\omega}) = A_{eff}\left(\int I_{2\omega}(L,t)dt\right) = A_{eff}\cdot s\cdot\frac{\left|P_{NL}(0)\right|^2}{\left[\Delta\left(v_g^{-1}\right)\right]^2}T_s = \frac{A_{eff}\cdot s\cdot L}{\Delta\left(v_g^{-1}\right)}\left|\int a_\omega^2(t)dt\right|^2 \qquad (2.53)$$

If the FH input pulse is BW-limited ($I_\omega(t)=\varepsilon_o c n_\omega a_\omega^2(t)/2$), we can get closed forms to describe the SH pulse energy, average power, and conversion efficiency:

$$U_{2\omega} = \frac{A_{eff}\cdot s\cdot L}{\Delta\left(v_g^{-1}\right)}\left(\int I_\omega(t)dt\right)^2\left(\frac{2}{\varepsilon_o c n_\omega}\right)^2 = \frac{\Gamma^2}{\Delta\left(v_g^{-1}\right)}\cdot\left(\frac{L}{A_{eff}}\right)\cdot U_\omega^2$$

$$\overline{P}_{2\omega} \equiv \frac{U_{2\omega}}{T_{rep}} = \frac{\Gamma^2}{\Delta\left(v_g^{-1}\right)}\left(\frac{L}{A_{eff}}\right)\cdot\left(U_\omega\cdot\overline{P}_\omega\right) \qquad (2.54)$$

$$\eta_{SHG} \equiv \frac{U_{2\omega}}{U_\omega} = \frac{\Gamma^2}{\Delta\left(v_g^{-1}\right)}\left(\frac{L}{A_{eff}}\right)\cdot U_\omega = \Gamma^2\left(\frac{L^2}{A_{eff}}\right)\cdot\hat{P}_\omega\cdot\left(\frac{\Delta t_{eff}}{T_s}\right) \qquad (2.55)$$

Comparing equations (2.54-55) with equations (2.46, 49), we can find that the narrowband SHG has several distinct features: (i) the average SH power $\overline{P}_{2\omega}$ does not scale with $\left(\hat{P}_\omega\cdot\overline{P}_\omega\right)$, but $\left(U_\omega\cdot\overline{P}_\omega\right)$. Therefore, eq. (2.48) is not a valid measure for quadratic measurement sensitivity using narrow PM BW. (ii) η_{SHG} scales with L, instead of L^2. (iii) η_{SHG} does not depend on input peak power $\hat{P}_\omega$, but input pulse energy U_ω. (iv) in comparison with eq. (2.49), η_{SHG} degrades by a factor of $\Delta t_{eff}/T_s$. As a result, normalized SHG efficiency η_{SHG}/U_ω in the unit of **%/pJ** is normally used to characterize the efficiency of narrowband ($\Delta\omega_{PM}<<\Delta\omega_{NLP}$) nonlinear media (e.g. long unchirped QPM waveguides). For chirped input pulses, η_{SHG} is lower than the estimation of eq. (2.55), because $\left|\int a_\omega^2(t)dt\right| < \int\left|a_\omega(t)\right|^2 dt$ when the temporal phase of $a_\omega(t)$ is not uniform.

(c) Constant PM BW ($\Delta\omega_{PM}>\Delta\omega_{NLP}$):

As will be further discussed in Sec. 3.1.2, QPM crystals with chirped periods can produce PM spectrum $H(\omega)$ other than the conventional *sinc*-function defined in eq. (2.41) by introducing some phase modulation on the nonlinear coefficient distribution $d_{eff}(z)$.

We are especially interested in the case (shown in Fig. 2.3c) where $|H(\omega)|$ is flat within a fixed BW of $\Delta\omega_{PM}$ ($>\Delta\omega_{NLP}$). Note that the PM spectral phase $\angle H(\omega)$ can be made uniform only if $d_{eff}(z)$ is a *sinc*-function (see eq. (3.8)), which is not desirable in terms of efficiency and fabrication. If the nonlinear strength $|d_{eff}(z)|$ is kept constant, the overall nonlinearity ($\propto \int |H(\omega)|^2 d\omega$) scales with crystal length L as in the cases of (a) and (b), leading to $|H(\omega)| \propto \sqrt{L}$ in the pass-band. We can characterize the SH pulse by:

$$A_{2\omega}(L,\omega) \propto \sqrt{L} \cdot P_{NL}(\omega) e^{j\angle H(\omega)} \tag{2.56}$$

Eq. (2.56) implies that $a_{2\omega}(L,t)$ is deviated from $a_{\omega}^2(t)$ due to the spectral phase modulation $\angle H(\omega)$ imposing on $P_{NL}(\omega)$. In general, the non-uniform $\angle H(\omega)$ makes the SH pulse highly chirped and substantially broader than $I_{\omega}^2(t)$.

As far as SH power and conversion efficiency are concerned, PM spectral phase $\angle H(\omega)$ is unimportant:

$$U_{2\omega}, \overline{P}_{2\omega} \propto A_{eff} L\left(\int |P_{NL}(\omega)|^2 d\omega\right) \propto A_{eff} L\left(\int I_{\omega}^2(t) dt\right) = \frac{L U_{\omega}^2}{A_{eff} \Delta t_{eff}} \tag{2.57}$$

$$\overline{P}_{2\omega} \equiv \frac{U_{2\omega}}{T_{rep}} \propto \left(\frac{L}{A_{eff}}\right) \cdot \left(\hat{P}_{\omega} \cdot \overline{P}_{\omega}\right) \tag{2.58}$$

$$\eta_{SHG} \equiv \frac{U_{2\omega}}{U_{\omega}} \propto \left(\frac{L}{A_{eff}}\right) \cdot \hat{P}_{\omega} \tag{2.59}$$

Equations (2.58-59) reveal the properties of SHG with constant PM BW: (i) $\overline{P}_{2\omega}$ scales with $\left(\hat{P}_{\omega} \cdot \overline{P}_{\omega}\right)$, therefore, eq. (2.48) is valid for measurement sensitivity. (ii) η_{SHG} scales with L, instead of L^2. (iii) η_{SHG} normalized to peak power $\hat{P}_{\omega}$ in the unit of **%/W** can be used to characterize the efficiency of a nonlinear medium with a flat $|H(\omega)|$ covering the entire bandwidth of $P_{NL}(\omega)$.

2.2 Chromatic Dispersion Monitoring

Optical pulses tend to be temporally broadened (spectrally phase modulated, or chirped) when propagating through a dispersive medium, for the different frequency components of the pulses travel with different speeds. This phenomenon, namely chromatic dispersion of optical media, can seriously restrict the delivery of short optical pulses. Sensing the chirp for ultrashort pulses is not straightforward, for it distorts the temporal waveforms without changing their averaged powers. Extremely high-speed (BW>1 THz) oscilloscopes would be required to electronically resolve the intensity variation of ultrashort pulses.

One way to diagnose pulse chirp (medium dispersion) without high-speed electronics is employing the chirp-dependent SHG yield. For simplicity, we deduce a quantitative description for this detecting scheme by Gaussian pulse model [25-26]. The complex spectrum of a linearly chirped Gaussian pulse envelope is:

$$A_\omega(\omega) = \exp\left[-\omega^2/(\Delta\omega)^2\right]\cdot\exp\left[j\alpha\omega^2\right] \tag{2.60}$$

where the quadratic spectral phase parameter α corresponds to the dispersion strength (dispersion-length product) in a real medium. The temporal intensity profile $I_\omega(t)$ corresponding to eq. (2.60) is:

$$I_\omega(t) \propto \left(1\Big/\sqrt{1+\alpha^2(\Delta\omega)^4}\right)\times\exp\left[-(\Delta\omega)^2 t^2/2(1+\alpha^2(\Delta\omega)^4)\right] \tag{2.61}$$

For simplicity, we formulate the chirp-dependent average SHG power $\overline{P}_{2\omega}(\alpha)$ for two special cases:

(a) Flat PM response with broad BW ($\Delta\omega_{PM} > \Delta\omega_{NLP}$):

This case is illustrated in Figures 2.3a and 2.3c. According to the equations (2.45, 57), the energy and average power of SH pulse are proportional to $\int I_\omega^2(t)dt$:

$$\overline{P}_{2\omega}(\alpha) \propto \int\left|P_{NL}(\omega)\right|^2 d\omega \propto \int I_\omega^2(t)dt \propto \overline{P}_{2\omega}(0)\Big/\sqrt{1+\alpha^2(\Delta\omega)^4} \tag{2.62}$$

(b) Narrow PM BW ($\Delta\omega_{PM} << \Delta\omega_{NLP}$):

This case is illustrated in Fig. 2.3b. As indicated by eq. (2.53), the chirp strength α of the input FH pulse can influence the SHG yield $\overline{P}_{2\omega}$ through nonlinear polarization term $P_{NL}(0)$:

$$P_{NL}(0)=\int A_{\omega}(-\omega)A_{\omega}(\omega)d\omega=\int\exp\left[-\frac{2\omega^2}{(\Delta\omega)^2}+j2\alpha\omega^2\right]d\omega=\sqrt{\frac{\pi}{2}}\left(\frac{1}{(\Delta\omega)^2}-j\alpha\right)^{-1/2}$$

$$\overline{P}_{2\omega}(\alpha)\propto\left|P_{NL}(0)\right|^2\propto\overline{P}_{2\omega}(0)\Big/\sqrt{1+\alpha^2(\Delta\omega)^4} \tag{2.63}$$

Although the SH pulses generated by broadband and narrowband nonlinear crystals are very different in shape, equations (2.62-63) show that their SHG yields happen to have identical chirp-dependence. Equations (2.61-63) also indicate that a common chirp-dependent factor $\sqrt{1+\alpha^2(\Delta\omega)^4}$ governs FH pulse broadening, FH peak intensity reduction, and SH power degradation. Consequently, the product of FH pulse duration Δt and average SH power $\overline{P}_{2\omega}$ should be a constant for different chirp (dispersion) strength α, which is useful in checking the experimental results.

The coincidence between equations (2.62-63) is only valid for even-order spectral phases. We examine this fact by using a Gaussian pulse with purely cubic spectral phase:

$$A_{\omega}(\omega)=\exp\left[-\omega^2/(\Delta\omega)^2\right]\cdot\exp\left[j\beta\omega^3\right] \tag{2.64}$$

The corresponding intensity profile $I_{\omega}(t)$ is generally broadened with β and has an oscillatory tail (see inset of Fig. 2.4b). Since crystals with broad PM BW produce SHG yield $\overline{P}_{2\omega}$ in favor of higher peak intensity ($\overline{P}_{2\omega}\propto\int I_{\omega}^2(t)dt$), $\overline{P}_{2\omega}$ will monotonically degrade with β. In the case of narrow PM BW, however, $\overline{P}_{2\omega}$ is entirely insensitive to β, for the cubic phases cancel with each other in the formation of $P_{NL}(0)$:

$$P_{NL}(0)=\int A_{\omega}(-\omega)\cdot A_{\omega}(\omega)d\omega=\int\exp\left[-\frac{2\omega^2}{(\Delta\omega)^2}+j(\beta-\beta)\omega^3\right]d\omega$$

$$\Rightarrow\overline{P}_{2\omega}(\beta)\propto\left|P_{NL}(0)\right|^2=\overline{P}_{2\omega}(0) \tag{2.65}$$

As a result, it is more desirable to use a SHG crystal with flat PM response and broad BW in diagnosing signal distortion caused by arbitrary spectral phase modulation.

Fig. 2.4 illustrates the simulations of SHG yield $\overline{P}_{2\omega}$ versus quadratic and/or cubic spectral phases under the assumptions of Gaussian power spectrum (central wavelength λ_0=1542 nm, FWHM=1.2 nm) and broad PM BW, where $\overline{P}_{2\omega}$ generally

decreases from its maximum whenever quadratic or cubic phase is applied. Dynamic dispersion compensation, therefore, can be realized by maximizing the monitoring signal $\overline{P}_{2\omega}$.

2.3 Intensity Autocorrelation

Intensity autocorrelation technique was widely used to estimate the ultrashort pulse durations during the early days when other advanced measurement techniques remained inapplicable. In this section, we will formulate the autocorrelation traces obtained by SHG crystals with broad and narrow PM BWs, respectively. Detailed investigation about the interrelations among autocorrelation trace, PM BW, and pulse shape is referred to [11].

2.3.1 Intensity autocorrelation with broad PM BW

The collinear geometry of intensity autocorrelation measurement scheme is illustrated in Fig. 2.5. The Michelson interferometer (MI) split and recombine the input pulse envelope $a_{in}(t) \propto a(t)$ to produce a pulse pair:

$$a_{out}(t,\tau) \propto a(t) + a(t-\tau)e^{-j\omega_o\tau} \tag{2.66}$$

where the two pulse replicas are assumed to have equal powers. When the PM BW is extremely broad ($\Delta\omega_{PM} >> \Delta\omega_{NLP}$, case (a) in Sec. 2.1.3) the instantaneous SH power is simply proportional to the square of the instantaneous FH power (see eq. (2.44)):

$$\begin{aligned} P_{2\omega}(t,\tau) &\propto P_{out}^2(t,\tau) \propto \left|a_{out}(t)\right|^4 \propto \left|a(t)\right|^4 + \left|a(t-\tau)\right|^4 + 4\left|a(t)a(t-\tau)\right|^2 \\ &+ \left\{2\left[\left(\left|a(t)\right|^2 + \left|a(t-\tau)\right|^2\right)a(t)a^*(t-\tau)\right]e^{j\omega_0\tau} + \left[a(t)a^*(t-\tau)\right]^2 e^{j2\omega_0\tau} + c.c.\right\} \end{aligned} \tag{2.67}$$

The slow power meter simply measures the t-integration of eq. (2.67):

$$\begin{aligned} \overline{P}_{2\omega,IAC}(\tau) &\propto 2\left\langle\left|a(t)\right|^4\right\rangle + 4\left\langle\left|a(t)a(t-\tau)\right|^2\right\rangle \\ &+ \left\{2\left\langle\left(\left|a(t)\right|^2 + \left|a(t-\tau)\right|^2\right)a(t)a^*(t-\tau)\right\rangle e^{j\omega_0\tau} + \left\langle\left[a(t)a^*(t-\tau)\right]^2\right\rangle e^{j2\omega_0\tau} + c.c.\right\} \end{aligned} \tag{2.68}$$

Eq. (2.68) represents the interferometric autocorrelation (IAC) trace, which contains fringes corresponding to frequencies of ω_o and $2\omega_o$. Note that according to case (c) in Sec. 2.1.3, chirped QPM crystals with flat PM strength $|H(\omega)|$ within the entire nonlinear polarization spectrum $P_{NL}(\omega)$ can produce the same SH average power and IAC trace described by eq. (2.68), although the instantaneous SH power $P_{2\omega}(t,\tau)$ is different from eq. (2.67). The IAC trace $\overline{P}_{2\omega,IAC}(\tau)$ can be low-pass filtered (LPF) with respect to τ by a software routine to remove the interferometric fringes:

$$\overline{P}_{2\omega}(\tau) \propto \left\langle |a(t)|^4 \right\rangle + 2\left\langle |a(t)a(t-\tau)|^2 \right\rangle = \left\langle I^2(t) \right\rangle + 2\left\langle I(t)I(t-\tau) \right\rangle \propto 1 + 2G_2(\tau) \tag{2.69}$$

$$G_2(\tau) \equiv \frac{\left\langle I(t)I(t-\tau) \right\rangle}{\left\langle I^2(t) \right\rangle} \tag{2.70}$$

where $I(t) \propto |a(t)|^2$, and $G_2(\tau)$ is the normalized intensity autocorrelation function. Since $G_2(\tau) \le G_2(0) = 1$, $G_2(\tau) \to 0$ as $|\tau| >> \Delta t$ (duration of $I(t)$), fringe-free autocorrelation trace $\overline{P}_{2\omega}(\tau)$ is a curve with a 3:1 peak-to-background contrast ratio. Background-free $G_2(\tau)$ can be obtained by subtracting $\overline{P}_{2\omega}(|\tau| >> \Delta t)$ from $\overline{P}_{2\omega}(\tau)$.

When the power ratio r of the two split pulses from the MI is unbalanced ($r \neq 1$), autocorrelation trace $\overline{P}_{2\omega}(\tau)$ still preserves the $G_2(\tau)$ information except that the contrast ratio is reduced:

$$a_{out}(t,\tau) \propto \sqrt{r} \cdot a(t) + a(t-\tau)e^{-j\omega_o \tau} \tag{2.71}$$

$$\overline{P}_{2\omega}(\tau) \propto 1 + \left(\frac{4r}{1+r^2} \right) G_2(\tau) \tag{2.72}$$

In real experiments, balanced power ($r=1$) is preferred to maximize the signal-to-background ratio.

In general, the width of $G_2(\tau)$ (defining the FWHM of $G_2(\tau)$ as correlation width $\Delta\tau$) roughly approximates the pulse duration Δt, for the overlap integral $\left\langle I(t)I(t-\tau) \right\rangle$ vanishes as $|\tau| >> \Delta t$. The exact deconvolution factor R_{dec} (defined as $\Delta\tau/\Delta t$), however, depends on the pulse shape. For example, the R_{dec} values are 1.41 and 1.54 for chirpless Gaussian and sech^2 pulses, respectively. For most well-behaved pulse shapes, the

variation of R_{dec}'s remains in the order of 10% [10]. This allows experimentalists to roughly estimate pulse duration Δt by the measured correlation width $\Delta\tau$ and a deconvolution factor R_{dec} corresponding to some presumed pulse shape. Large pulse chirp can also be identified if the product of $\Delta\tau$ and power spectral width Δf (measured by an optical spectrum analyzer) is considerable (>>1).

Retrieving more pulse information from $G_2(\tau)$, however, is strictly limited by the following reasons:

(i) $G_2(\tau)$ has no temporal phase information, for eq. (2.70) only deals with temporal intensity profile $I(t)$.

(ii) A large number of intensity profiles can give rise to the same $G_2(\tau)$. Complicated waveforms are usually left unnoticed in intensity autocorrelation measurements, for $G_2(\tau)$ has poor sensitivity to the fine structure of $I(t)$ (see Fig. 2.6) [12].

(iii) $G_2(\tau)$ can not identify any pulse asymmetry, because it is always an even function:

$$\langle I(t)I(t-\tau)\rangle = \int_{-\infty}^{\infty} I(t)I(t-\tau)dt = \int_{-\infty}^{\infty} I(t'+\tau)I(t')dt' = \langle I(t)I(t+\tau)\rangle$$

However, processing IAC traces obtained by unbalanced power ratio ($r\neq 1$) can detect small pulse asymmetry without the direction-of-time ambiguity [33].

(iv) Complete retrieval of $I(t)$ from $G_2(\tau)$ is possible only if $I(t)$ is symmetric. We can examine this fact by Fourier transform:

$$F_\tau\{G_2(\tau)\} \propto \int_{-\infty}^{\infty}\left(\int_{-\infty}^{\infty} I(t)I(t-\tau)dt\right)\cdot e^{-j\omega\tau}d\tau, \quad \text{let} \quad t-\tau \equiv \tau',$$

$$= \left(\int_{-\infty}^{\infty} I(t)\cdot e^{-j\omega t}dt\right)\cdot\left(\int_{-\infty}^{\infty} I(\tau')\cdot e^{j\omega\tau'}d\tau\right) = \tilde{I}(\omega)\cdot\tilde{I}(-\omega) = \left|\tilde{I}(\omega)\right|^2 \qquad (2.73)$$

where $\tilde{I}(\omega) \equiv F_t\{I(t)\}$, and $\tilde{I}(-\omega) = \tilde{I}^*(\omega)$ is guaranteed by real $I(t)$. If $I(t)$ is further known to be symmetric, $I(\omega)$ must be real, and can be derived by taking square root of eq. (2.73). Another inverse Fourier transform is sufficient to obtain the complete $I(t)$ profile.

In conclusion, $G_2(\tau)$ obtained by intensity autocorrelation measurements only provides a rough estimation about the pulse duration. Estimation error can be appreciable for lack of the pre-knowledge about the ill-behaved shape and high chirp of the input

pulse. More sophisticated techniques, such as frequency-resolved optical gating (FROG) [12, 34-36] and spectral interferometry for direct electric-field reconstruction (SPIDER) [37-39], are required to realize complete pulse characterizations.

2.3.2 Modified field autocorrelation intensity with narrow PM BW

In Sec. 2.1.3 we found that extremely narrow PM BW ($\Delta\omega_{PM} << \Delta\omega_{NLP}$) can seriously stretch the output SH pulse (eq. (2.51)) and change the SHG efficiency (eq. (2.55)) for a single input pulse. In this subsection, we will analytically prove that autocorrelation traces resulting from a δ-like PM spectrum $H(\omega)$ give rise to the modified field autocorrelation intensity $|G'_1(\tau)|^2$ (see eq. (2.74)), instead of the traditional $G_2(\tau)$. To our best knowledge, this is the first **analytical** formulation describing the autocorrelation trace distortion due to insufficient PM BW. Detailed (numerical) analysis dealing with finite PM BW is referred to [11]. The results will justify the necessity of using an SHG crystal with sufficiently broad PM BW to obtain ideal intensity autocorrelation traces.

In the presence of a δ-like PM spectrum $H(\omega)$, the output SH average power is governed by: $\overline{P}_{2\omega} \propto |P_{NL}(0)|^2 = \left|\int_{-\infty}^{\infty} a_\omega^2(t)dt\right|^2$ (see eq. (2.53)). In an intensity autocorrelation measurement setup (see Fig. 2.5), the input FH pulse $a_\omega(t)$ is the recombined pulse pair $a_{out}(t,\tau)$ defined in eq. (2.66). Henceforth, we can deduce a distorted intensity autocorrelation trace as follows:

$$
\begin{aligned}
P_{NL}(0) &= \int_{-\infty}^{\infty} a_\omega^2(t)dt = \int_{-\infty}^{\infty} \left[a(t) + a(t-\tau)e^{-j\omega_0\tau}\right]^2 dt \\
&= \left(\int_{-\infty}^{\infty} a^2(t)dt\right) + e^{-j2\omega_0\tau}\left(\int_{-\infty}^{\infty} a^2(t-\tau)dt\right) + 2e^{-j\omega_0\tau}\left(\int_{-\infty}^{\infty} a(t)a(t-\tau)dt\right) \\
&= 2e^{-j\omega_0\tau}\left(\int_{-\infty}^{\infty} a^2(t)dt\right)\cdot\left[\cos(\omega_0\tau) + G'_1(\tau)\right];
\end{aligned}
$$

where $G'_1(\tau)$ is defined as the modified field autocorrelation function:

$$
G'_1(\tau) \equiv \frac{\int_{-\infty}^{\infty} a(t)a(t-\tau)dt}{\int_{-\infty}^{\infty} a^2(t)dt} \tag{2.74}
$$

which is distinct from the conventional field autocorrelation function:

$$\Gamma(\tau) \equiv \frac{\int_{-\infty}^{\infty} a(t)a^*(t-\tau)dt}{\int_{-\infty}^{\infty} |a(t)|^2 dt} \tag{2.75}$$

Note that both $G'_1(\tau)$ and $\Gamma(\tau)$ are complex. The interferometric trace $\overline{P}_{2\omega,IAC}(\tau)$ is:

$$\begin{aligned}\overline{P}_{2\omega,IAC}(\tau) &\propto \left|\cos(\omega_0\tau) + G'_1(\tau)\right|^2 \\ &= \frac{1+\cos(2\omega_0\tau)}{2} + 2\,\mathrm{Re}\{G'_1(\tau)\}\cos(\omega_0\tau) + \left|G'_1(\tau)\right|^2\end{aligned} \tag{2.76}$$

By low-pass filtering eq. (2.76) with respect to τ, we obtain the fringe-free trace analogous to eq. (2.69):

$$\overline{P}_{2\omega}(\tau) \propto 1 + 2\left|G'_1(\tau)\right|^2 \tag{2.77}$$

When the power ratio is unbalanced ($r \neq 1$), eq. (2.77) is modified in the same way as that of eq. (2.72):

$$\overline{P}_{2\omega}(\tau) \propto 1 + \left(\frac{4r}{1+r^2}\right) \cdot \left|G'_1(\tau)\right|^2 \tag{2.78}$$

For some specific pulse shapes, such as linearly chirped Gaussian and chirpless single-sided exponential pulses, $|G'_1(\tau)|^2$ happens to be identical to $G_2(\tau)$ [11]. However, this coincidence does not exist for most cases. For example, $|G'_1(\tau)|^2$ is sensitive to temporal phase of $a(t)$, which is entirely lost in $G_2(\tau)$. Even $a(t)$ has no temporal phase, $|G'_1(\tau)|^2 \neq G_2(\tau)$ because of the discrepancy between $\left(\int a(t)a(t-\tau)dt\right)^2$ and $\int a^2(t)a^2(t-\tau)dt$. Fig. 2.7 gives a numerical example to show the discrepancy between $G_2(\tau)$ and $|G'_1(\tau)|^2$ quantitatively. A BW-limited *sech*^{2} pulse (intensity FWHM Δt=220 fs) is traced with infinitely broad (dashed) and δ-like (solid) PM spectra, resulting in ideal intensity autocorrelation function $G_2(\tau)$ and modified field autocorrelation intensity $|G'_1(\tau)|^2$, respectively. The deconvolution factor corresponding to the $G_2(\tau)$ trace is 1.54, in agreement with the theoretical predication. The correlation width $\Delta\tau$ of $|G'_1(\tau)|^2$ curve, however, is 32-fs (+9.4%) wider than that of ideal $G_2(\tau)$, which is not negligible.

For highly chirped pulses, the deviation due to insufficient PM BW could be even more evident. Fig. 2.7 illustrates the simulated correlation width (FWHM) $\Delta\tau$ of a

chirped pulse as a function of PM tuning curve width $\Delta\lambda_{PM}$. The spectral intensity of the pulse is a $sech^2$ function (centered at λ_o=1550 nm, FWHM $\Delta\lambda$=15 nm), and the cubic spectral phase is denoted as $\psi(\lambda) = \pi\left[(\lambda - \lambda_o)/\Delta\lambda\right]^3$. The corresponding temporal intensity $I(t)$ (inset) has an FWHM of 338 fs, and the single-sided oscillating tail is noticeable. We assumed that the PM tuning curve $|H_\omega(\lambda)|^2$ is a $sinc^2$ function centered at λ_o=1550 nm and has an FWHM of $\Delta\lambda_{PM}$, where $|H_\omega(\lambda)|^2$ is related to the (baseband) PM power spectrum $|H(\omega)|^2$ (eq. (2.41)) via:

$$|H_\omega(\lambda)|^2 = \left|H\left(2\pi c(\lambda^{-1} - \lambda_o^{-1})\right)\right|^2, \quad c \text{ is the speed of light} \tag{2.79}$$

In this specific case, the correlation width obtained by an extremely narrow PM BW is substantially deviated from that arising from broad PM BW by 180 fs, corresponding to an error of –37.5%. The opposite signs of $\Delta\tau$-deviation in the simulations of Fig. 2.7 and Fig. 2.8 indicate that the insufficient PM BW can either increase or decrease the measured correlation width. The curve of $\Delta\tau$ versus $\Delta\lambda_{PM}$ in Fig. 2.8 converges to a constant, when $\Delta\lambda_{PM}$ starts to be greater than $\Delta\lambda$=15 nm. This result suggests that the ideal intensity autocorrelation function $G_2(\tau)$ can be approached if PM BW is close to or greater than input spectral width:

$$\Delta\lambda_{PM} \geq \Delta\lambda \tag{2.80}$$

In conclusion, we need sufficiently broad PM BW to get accurate intensity autocorrelation measurements. For a bulk crystal with uniform nonlinear coefficient d_{eff}, the available PM BW is inversely proportional to the GVM walkoff T_s or crystal length L (see eq. (2.41)). To accurately characterize sub-picosecond pulses, L is normally restricted to be in the order of millimeter or less. By eq. (2.49), short L may degrade the SHG efficiency (and the measurement sensitivity) with a quadratic scaling. The trade-off between PM BW and SHG efficiency restricts the sensitivity of intensity autocorrelation measurements using bulk crystals to be around 1 mW^2. In Sec. 3.1, we will discuss the chirped quasi-phase match (QPM) technique, which broadens the PM BW without sacrificing the SHG efficiency of short pulses, and contributes to the record sensitivity of $3.2 \bullet 10^{-7}$ mW^2 [22].

2.4 Conventional SHG FROG

As discussed in Sec. 2.3.1, intensity autocorrelation measurements fail to retrieve complete pulse information. Instead, the widely used SHG FROG can meet this goal with low power requirement in the absence of synchronized reference pulse. The general strategy of FROG measurements is recording much more data than the degrees of freedom, and then retrieving the unknown complex field envelope by iterative algorithm. In this section, we will only review the fundamentals of conventional SHG FROG scheme. The technical difficulties and solutions with regard to using chirped QPM $LiNbO_3$ waveguides in SHG FROG would be investigated in Chapter 4.

Fig. 2.9 illustrates schematic setup of the conventional noncollinear SHG FROG. The unknown laser pulse $a(t)$ is sent into a noncollinear Michelson interferometer (MI) to produce two pulse replicas spatially parallel and temporally separated by delay τ with each other. They are focused into a nonlinear bulk crystal with some specific angle to meet the birefringence PM conditions [31-32]. This will result in SHG pulses emitted in three different directions, in which only that driven by a nonlinear polarization $P_{NL}^{X}(\omega,\tau)$ associated with the self-gated field $a(t)\cdot a(t-\tau)$ is spatially selected by an iris:

$$P_{NL}^{X}(\omega,\tau) \propto F_t\{a(t)\cdot a(t-\tau)\} \tag{2.81}$$

where the superscript X emphasizes the crossed-beam geometry. Assuming that the crystal is thin enough that the PM spectrum is broad and uniform within the band where $\left|P_{NL}^{X}(\omega,\tau)\right|$ is not negligible, SH spectrum $A_{2\omega}(\omega,\tau)$ is proportional to $P_{NL}^{X}(\omega,\tau)$:

$$A_{2\omega}(\omega,\tau) \equiv A_{sig}(\omega,\tau) \propto P_{NL}^{X}(\omega,\tau) = F_t\{a(t)\cdot a(t-\tau)\} \tag{2.82}$$

$$a_{2\omega}(t,\tau) \equiv a_{sig}(t,\tau) \propto a(t)\cdot a(t-\tau) \tag{2.83}$$

Eq. (2.83) points out that the desired optical gating is carried out by the unknown pulse $a(t)$ itself in an ultrafast time scale. A combination of a spectrometer and a CCD camera are usually employed to record the output SH power spectrum for each delay τ, resulting a 2-D FROG trace $I_{FROG}(\omega,\tau)$:

$$I_{FROG}(\omega,\tau) \equiv \left|A_{2\omega}(\omega,\tau)\right|^2 = \left|A_{sig}(\omega,\tau)\right|^2 \propto \left|F_t\left\{a(t)\cdot a(t-\tau)\right\}\right|^2 \tag{2.84}$$

The next step we need to do is applying some iterative algorithm to retrieve the unknown pulse $a(t)$ from the measured FROG trace $I_{FROG}(\omega,\tau)$. Fig. 2.10 describes the iterative Fourier transform algorithm used for pulse reconstruction [10, 12, 34]. We start with an initial guess about the complex field envelope $a(t)$, the gated signal field $a_{sig}(t,\tau)$ is generated from eq. (2.83). By Fourier transforming $a_{sig}(t,\tau)$ with respect to t for each delay τ, we get a complex spectrogram $A_{sig}(\omega,\tau)$ corresponding to the current guess $a(t)$:

$$A_{sig}(\omega,\tau) \equiv F_t\left\{a_{sig}(t,\tau)\right\} \equiv \left|A_{sig}(\omega,\tau)\right| \cdot e^{j\psi_{sig}(\omega,\tau)} \tag{2.85}$$

According to eq. (2.84), the measured FROG trace $I_{FROG}(\omega,\tau)$ can be used to improve the spectral amplitude $|A_{sig}(\omega,\tau)|$ of eq. (2.85), while leaving the spectral phase $\psi_{sig}(\omega,\tau)$ intact:

$$A'_{sig}(\omega,\tau) = \sqrt{I_{FROG}(\omega,\tau)} \cdot e^{j\psi_{sig}(\omega,\tau)} \tag{2.86}$$

The improved complex spectrogram $A'_{sig}(\omega,\tau)$ is inversely transformed back into the time domain, resulting in an improved gated signal field $a'_{sig}(t,\tau)$. Subsequently, a simple integration over the delay τ gives rise to the new guess of complex field envelope $a(t)$:

$$\int_{-\infty}^{\infty} a_{sig}(t,\tau)d\tau = a(t)\cdot\left(\int_{-\infty}^{\infty} a(\tau')d\tau'\right) \propto a(t) \tag{2.87}$$

The process is repeated until the FROG error $G^{(k)}$ between the measured trace $I_{FROG}(\omega,\tau)$ and the retrieved trace in the k-th iteration $I^{(k)}_{FROG}(\omega,\tau)$ is lower than an acceptable tolerance [12]:

$$G^{(k)} \equiv \sqrt{\frac{1}{N}\sum_{i,j=1}^{N}\left|I_{FROG}(\omega_i,\tau_j) - \mu I^{(k)}_{FROG}(\omega_i,\tau_j)\right|^2} \tag{2.88}$$

where μ is a real normalization constant used for minimizing the FROG error $G^{(k)}$. The iterative Fourier transform algorithm is simple and fast, however, it is unstable in the presence of noise, and fails to converge for pulses with fine structure [12]. More advanced algorithms, such as generalized projections [40], and principal component generalized projections [41-42], have been developed to improve the convergence and speed. Real-time femtosecond oscilloscope based on SHG FROG and principal

component generalized projections algorithm permits a display update of 1.25 Hz for a 64x64 data grid [42].

The uniqueness of the retrieved pulse field from SHG FROG trace is another critical issue. In addition to trivial ambiguities for general FROG schemes (e.g. absolute phase), SHG FROG has the time-reversal ambiguity (i.e. $a(t)$ and $a^*(-t)$; or equivalently $A(\omega)$ and $A^*(\omega)$, produce the same trace) due to the τ-symmetry [12]:

$$A'_{sig}(\omega,\tau) \equiv F_t\left\{a^*(-t)\cdot a^*(-(t-\tau))\right\} = A^*_{sig}(\omega,-\tau)$$

$$\Rightarrow I'_{FROG}(\omega,\tau) = \left|A'_{sig}(\omega,\tau)\right|^2 = I_{FROG}(\omega,-\tau) = I_{FROG}(\omega,\tau) \qquad (2.89)$$

This ambiguity can be easily removed by a couple of ways. For example, making another measurement for pulses distorted by some known dispersion helps to determine the sign of the retrieved spectral phase. On the other hand, surface reflections from a thin piece of glass introduce a weak tailing satellite pulse, which can uniquely identify the direction of time [35]. SHG FROG is also vulnerable to approximative ambiguity when the pulse consists of two or more well-separated sub-pulses [12]. In this case, the phases corresponding to the low-intensity valleys have a π-uncertainty, causing the iterative retrieval to stagnate. [43] discusses the uniqueness of FROG measurements in more detail.

Despite the ambiguities, SHG FROG remains attractive in complete pulse characterizations because [12, 35]:

(i) It is self-referenced. No synchronized reference signal is required.

(ii) Better sensitivity: SHG takes advantage of the strongest $\chi^{(2)}$ nonlinearity.

(iii) Better signal-to-noise ratio: the signal spectrum is well separated from that of source spectrum, so the scattered light is easily filtered out.

(iv) Self-consistency checks can help to correct the systematic errors in the experiments.

(v) Redundancy built into the FROG trace reduces the reconstruction error due to noise contamination of the experimental data.

In Chapter 4, we will demonstrate how to realize record-sensitive SHG FROG measurements by using a chirped QPM waveguide with broad, yet uneven, PM spectrum, and operated in collinear geometry.

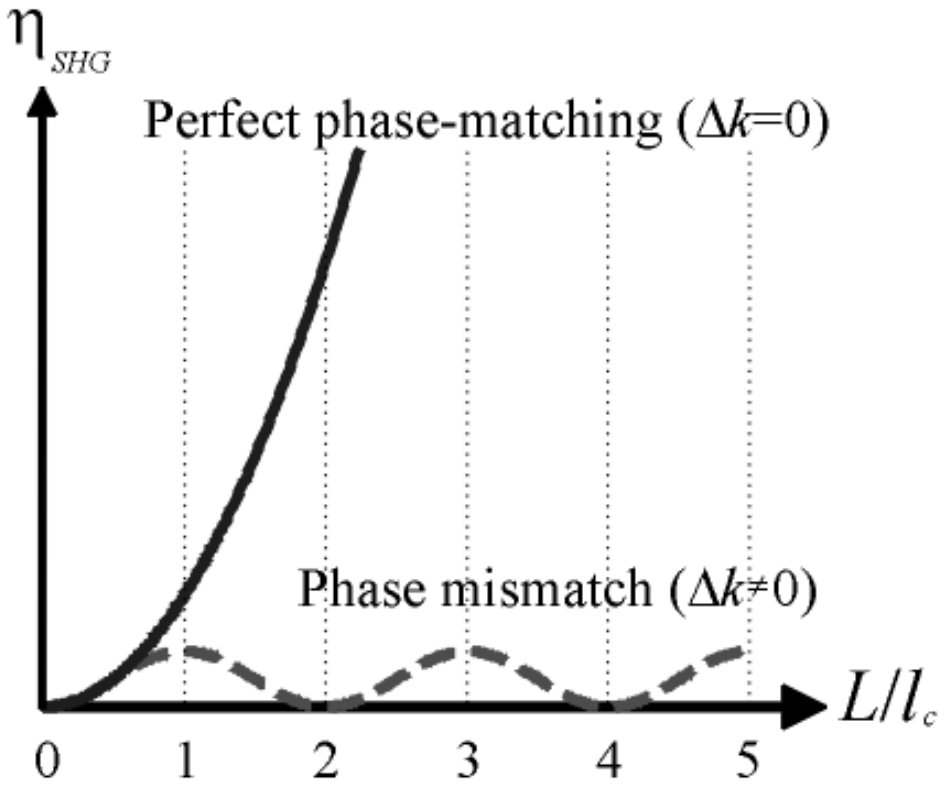

Fig. 2.1. SHG efficiencies η_{SHG} versus normalized interaction length L/l_c for perfect (Δk=0, solid) and imperfect ($\Delta k \neq 0$, dashed) phase-matching conditions. $l_c \equiv \pi/\Delta k$ is the coherence length in the presence of phase mismatch.

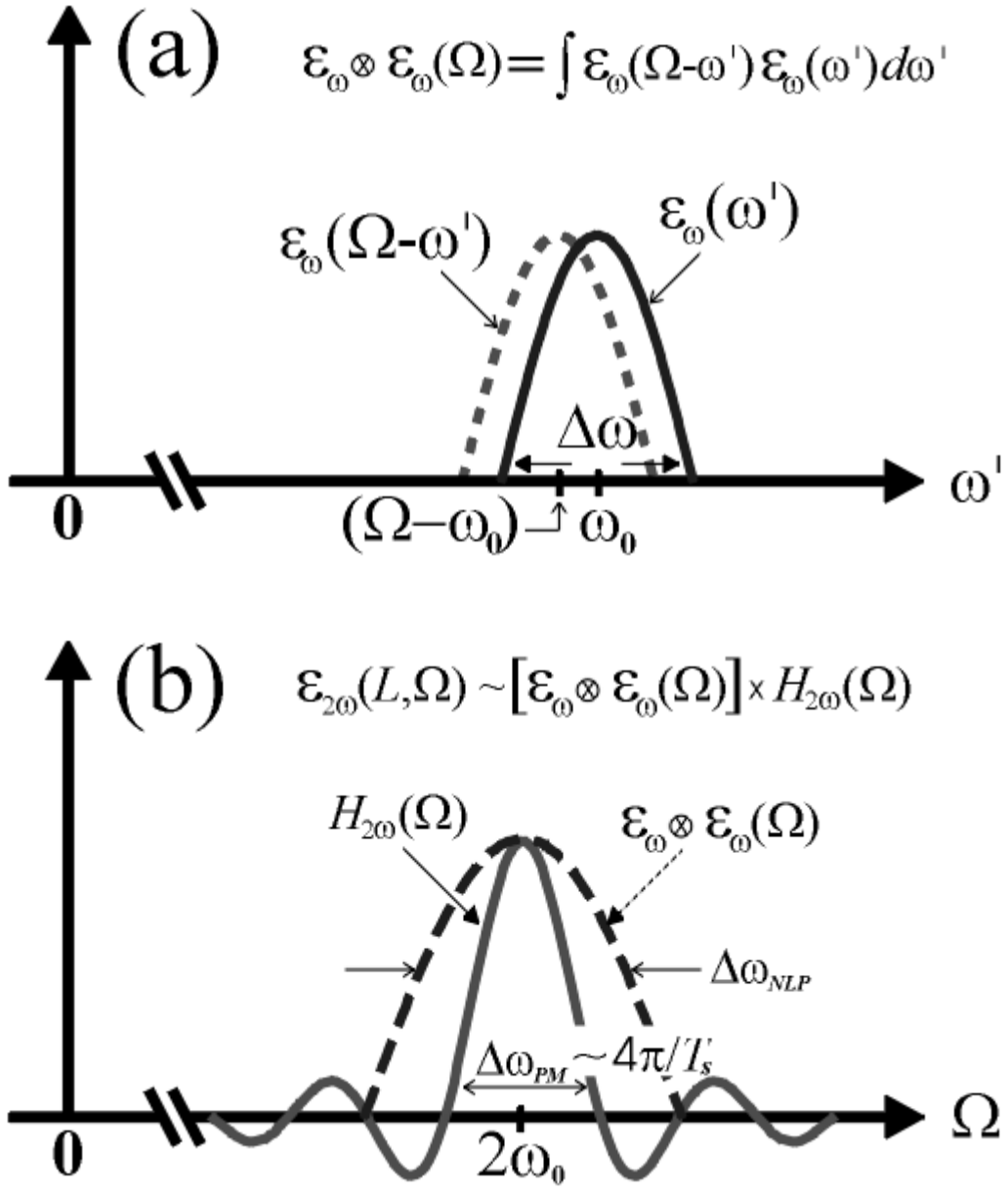

Fig. 2.2. Spectral manipulations of pulsed SHG: (a) spectral autoconvolution $\varepsilon_\omega \otimes \varepsilon_\omega(\Omega) = \int \varepsilon_\omega(\omega')\varepsilon_\omega(\Omega-\omega')d\omega'$ implies that each SH frequency component Ω is driven by various combinations of FH frequency pairs ω' and $\Omega-\omega'$. (b) Spectral components of $\varepsilon_\omega \otimes \varepsilon_\omega(\Omega)$ outside the $H_{2\omega}(\Omega)$ curve can not be phased matched., which can distort the output SH spectrum $\varepsilon_{2\omega}(L,\Omega)$ from the ideal $\varepsilon_\omega \otimes \varepsilon_\omega(\Omega)$. T_s is the GVM walkoff.

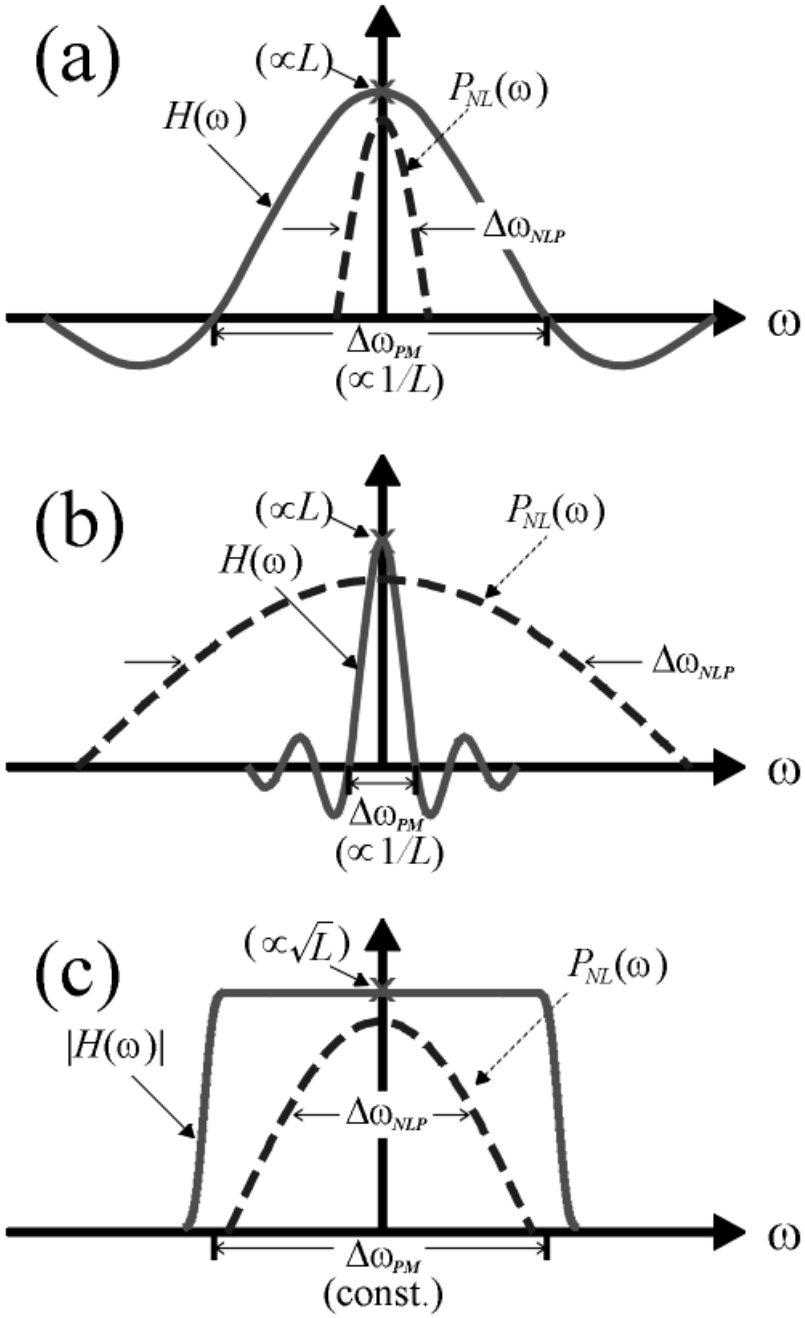

Fig. 2.3. Nonlinear polarization $P_{NL}(\omega)$ and PM spectrum $H(\omega)$ for pulsed SHG using: (a) extremely broad PM BW ($\Delta\omega_{PM} >> \Delta\omega_{NLP}$) from a thin crystal, (b) extremely narrow PM BW ($\Delta\omega_{PM} << \Delta\omega_{NLP}$) from a thick crystal, (c) constant PM BW ($\Delta\omega_{PM} > \Delta\omega_{NLP}$) from a thick QPM crystal with chirped periods. L denotes the crystal length.

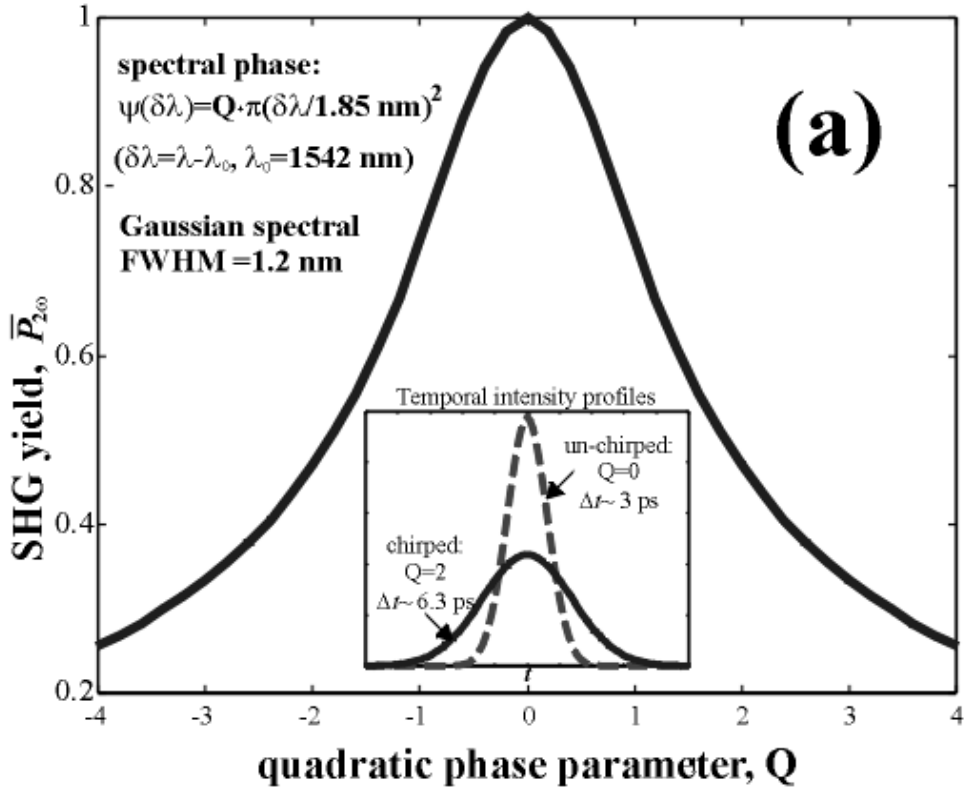
spectral phase:
ψ(δλ)=Q·π(δλ/1.85 nm)²
(δλ=λ-λ₀, λ₀=1542 nm)
Gaussian spectral
FWHM =1.2 nm
(a)
Temporal intensity profiles
un-chirped:
Q=0
Δt~ 3 ps
chirped:
Q=2
Δt~ 6.3 ps
SHG yield, P̄2ω
quadratic phase parameter, Q

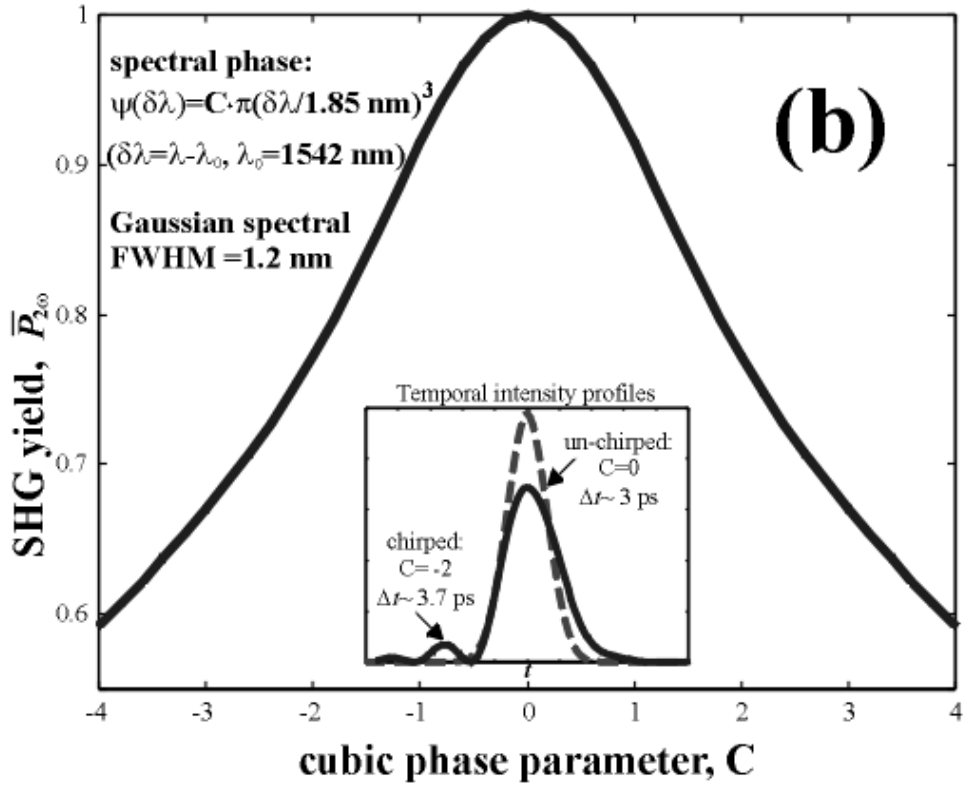
spectral phase:
ψ(δλ)=C·π(δλ/1.85 nm)³
(δλ=λ-λ₀, λ₀=1542 nm)
Gaussian spectral
FWHM =1.2 nm
(b)
Temporal intensity profiles
un-chirped:
C=0
Δt~ 3 ps
chirped:
C=-2
Δt~ 3.7 ps
SHG yield, P̄2ω
cubic phase parameter, C

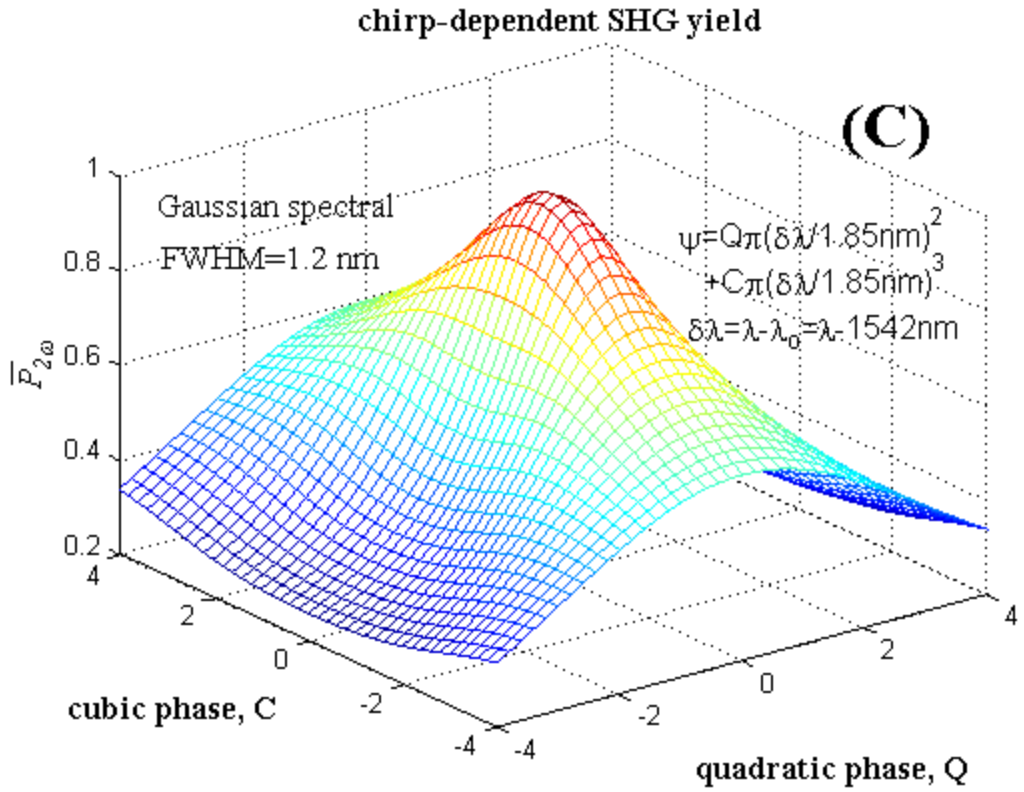

Fig. 2.4. SHG yields $\overline{P}_{2\omega}$ versus quadratic and/or cubic spectral phases under the assumptions of Gaussian power spectrum (central wavelength λ_o=1542 nm, FWHM=1.2 nm) and broad PM BW. The spectral phase profile $\psi(\delta\lambda)$ ($\delta\lambda \equiv \lambda-\lambda_o$) is characterized as: (a) quadratic function $\psi(\delta\lambda)=Q\cdot\pi\cdot(\delta\lambda/1.85\text{nm})^2$; (b) purely cubic function $\psi(\delta\lambda)=C\cdot\pi\cdot(\delta\lambda/1.85\text{nm})^3$; (c) a function with quadratic and cubic components simultaneously. The insets in (a-b) show the pulse shapes corresponding to Q=2 and C=-2, respectively.

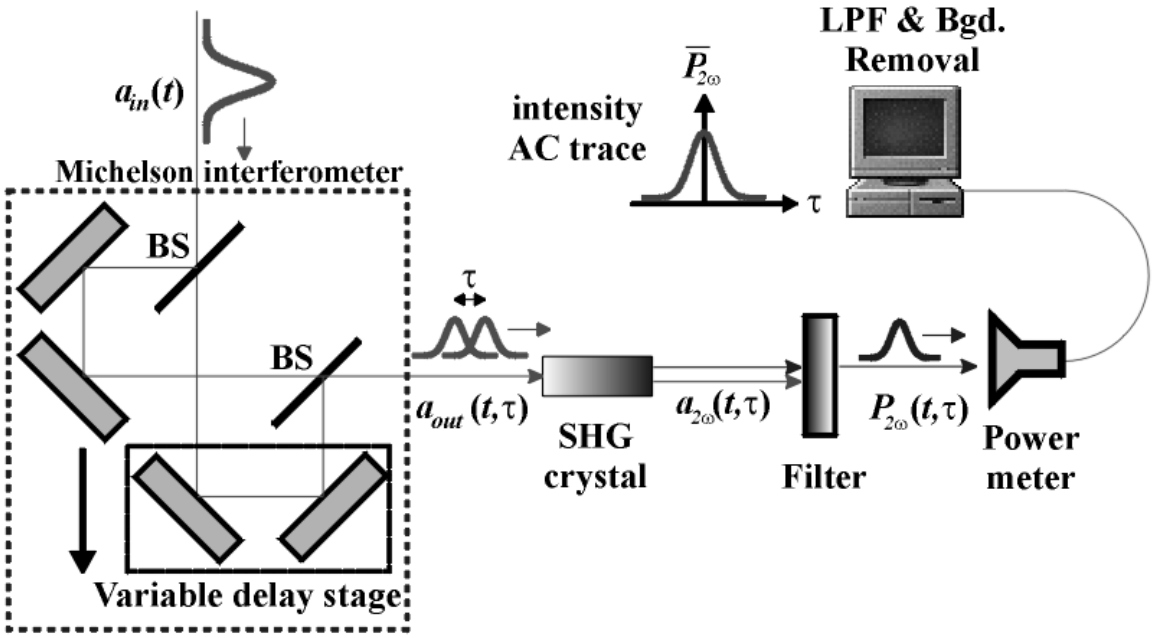

Fig. 2.5. Schematic diagram of collinear intensity autocorrelation measurements. BS: beam splitter.

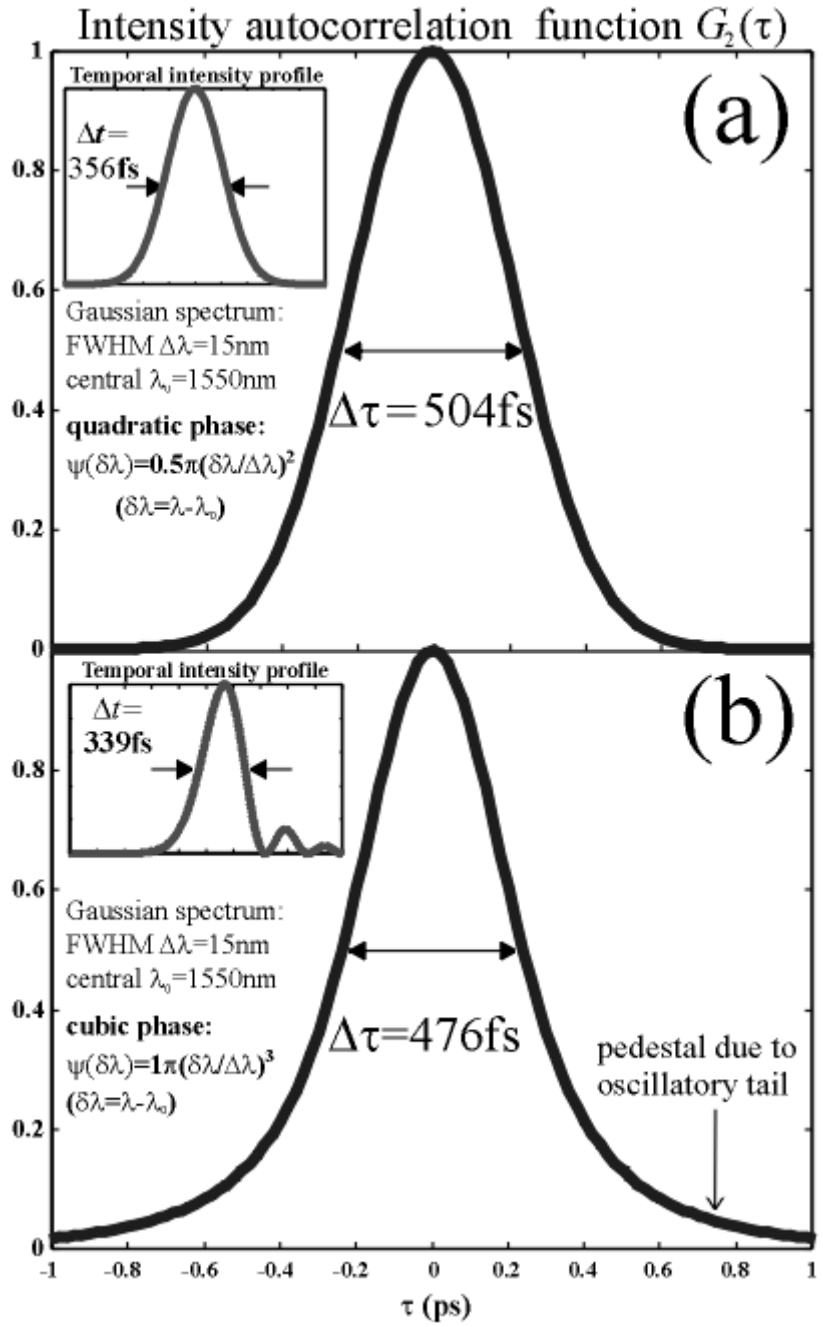

Fig. 2.6. Simulated intensity autocorrelation function $G_2(\tau)$ for pulses with Gaussian power spectrum (centered at λ_o=1550 nm, FWHM $\Delta\lambda$=15 nm) and (a) quadratic phase: $\psi(\delta\lambda)=0.5\pi\cdot(\delta\lambda/\Delta\lambda)^2$, (b) purely cubic phases: $\psi(\delta\lambda)=\pi\cdot(\delta\lambda/\Delta\lambda)^3$. The insets show the corresponding intensity profiles. $G_2(\tau)$ remains smooth in (b), while the oscillatory tail of intensity profile causes a slight pedestal in $G_2(\tau)$.

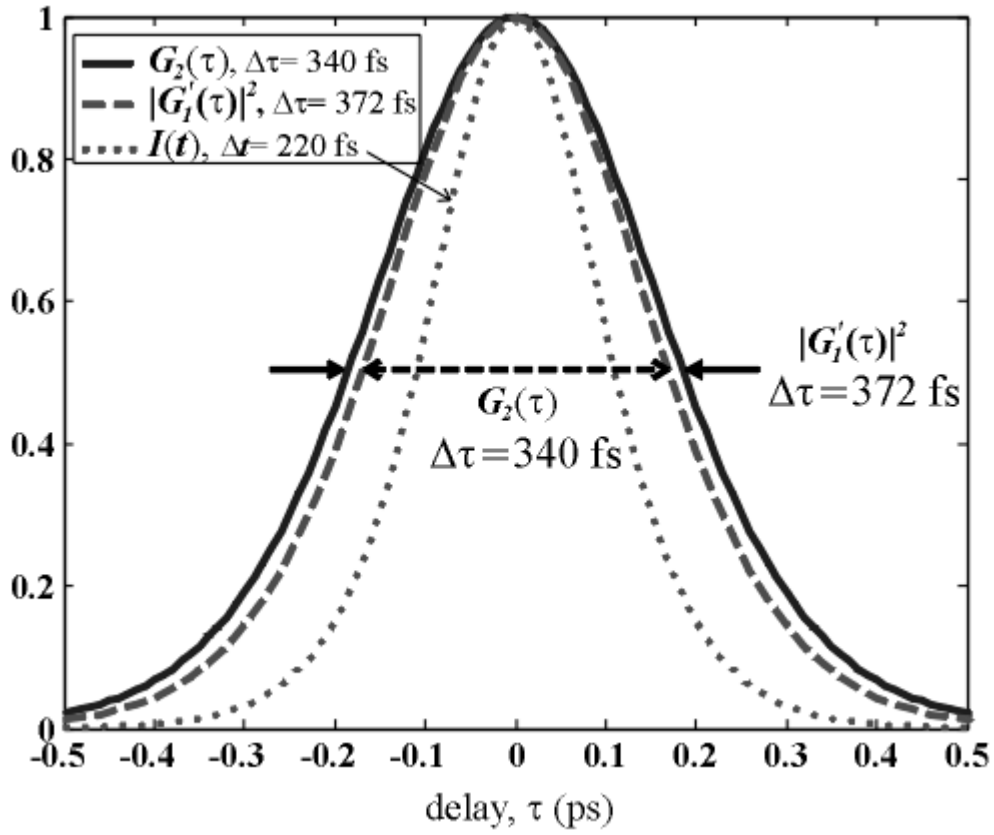

Fig. 2.7. Simulated autocorrelation traces of a chirpless *sech*^{2} pulse (dotted curve represents the intensity profile with 220-fs FWHM). The dashed curve is the ideal intensity autocorrelation function $G_2(\tau)$ obtained by a broad PM BW, while the solid curve is the modified field autocorrelation intensity $|G'_1(\tau)|^2$ arising from a narrow PM BW. In this specific case, the narrow PM BW broadens the correlation width $\Delta\tau$ by 32 fs (+9.4 %).

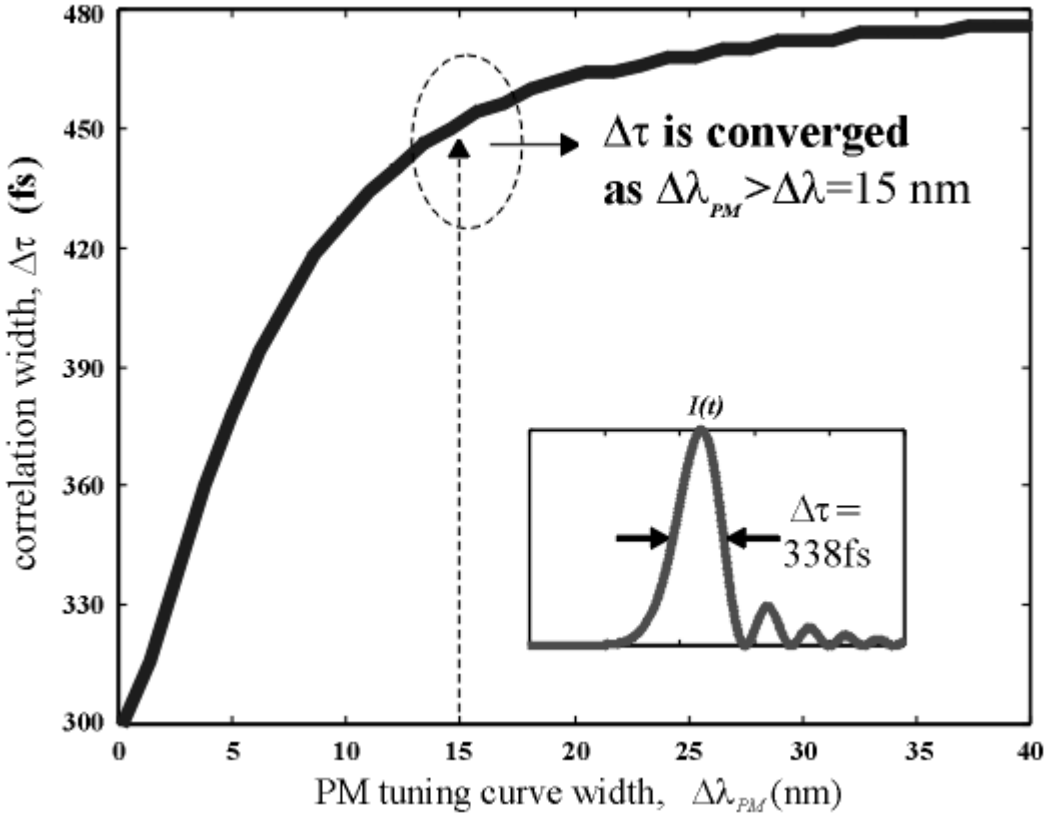

Fig. 2.8. Simulated correlation width $\Delta\tau$ as a function of PM tuning curve BW $\Delta\lambda_{PM}$. The input pulse (intensity profile is shown in the inset) has a $sech^2$ power spectrum with central wavelength λ_o=1550 nm, spectral FWHM $\Delta\lambda$=15 nm, and a cubic spectral phase $\psi(\lambda) = \pi\left[(\lambda - \lambda_o)/\Delta\lambda\right]^3$. As $\Delta\lambda_{PM}$ increases from 0.2 nm to 40 nm, $\Delta\tau$ varies from 300 fs to 480 fs, where convergence is approached when $\Delta\lambda_{PM} \geq \Delta\lambda$=15 nm.

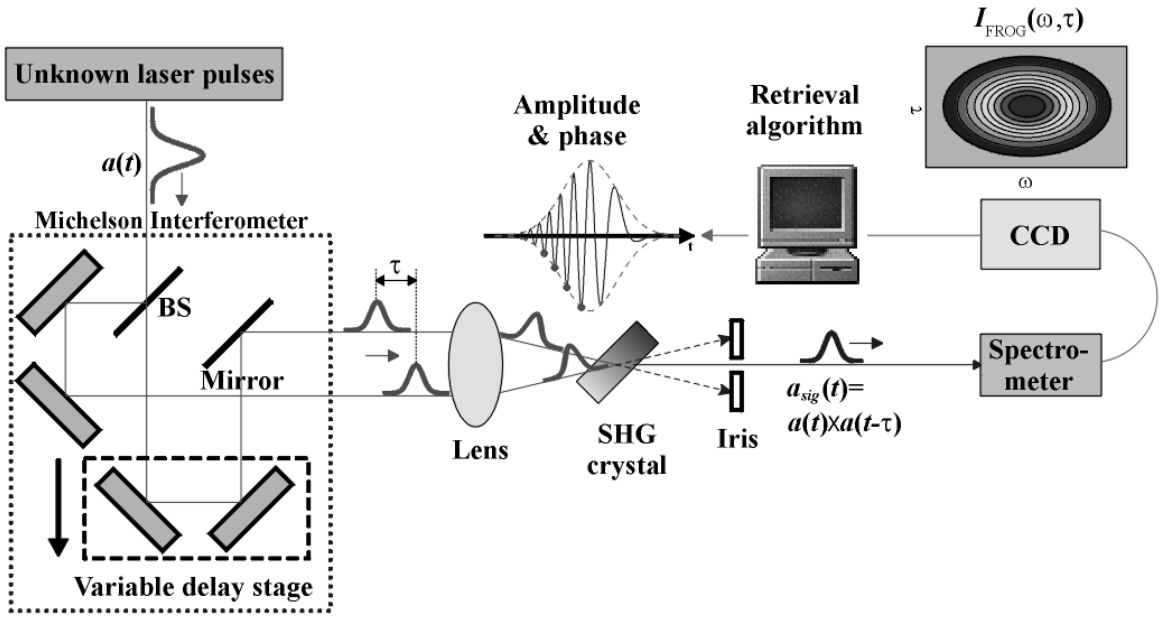

Fig. 2.9. Schematic diagram of conventional non-collinear SHG FROG measurements. BS represents beam splitter.

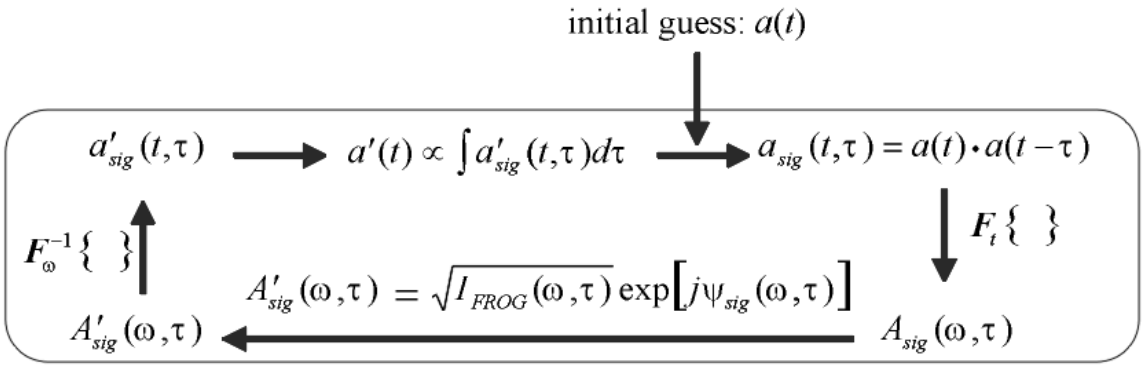

Fig. 2.10. Iterative Fourier transform algorithm for FROG signal reconstruction.

3. QPM $LiNbO_3$ WAVEGUIDES AND EXPERIMENTAL STUDIES OF CHROMATIC DISPERSION MONITORING AND INTENSITY AUTOCORRELATION

The capability of engineering SHG PM spectrum in quasi-phase matching (QPM) technique is applicable to eliminate the trade-off between SHG efficiency and PM BW encountered by bulk crystals. In this chapter, we will summarize the QPM formalism and the specifications of our uniform and chirped QPM $LiNbO_3$ waveguides. Experimental results in chromatic dispersion monitoring and intensity autocorrelation measurements will then be presented to confirm the extraordinary sensitivity performance achieved by our schemes.

3.1 Quasi-phase Matching (QPM)

3.1.1 Uniform QPM gratings

Eq. (2.24) shows that the CW SHG efficiency drops rapidly ($sinc^2$ scale) with phase mismatch Δk (defined in eq. (2.18)), which is generally nonzero because of the intrinsic material dispersion:

$$\Delta k \equiv k_{2\omega} - 2k_{\omega} = \frac{2\omega_0}{c}\left(n_{2\omega} - n_{\omega}\right) \tag{3.1}$$

Instead of playing with crystal birefringence and input beam polarizations to equate $n_{2\omega}$ and n_{ω} [31], uniform QPM gratings can compensate the intrinsic Δk by introducing an artificial wave number K_{QPM} arising from periodically modulating the nonlinear coefficient d_{eff} with some specific period Λ_o:

$$d_{eff}(z) = \sum_{m=-\infty}^{\infty} d_{eff}^{(m)} \cdot e^{jmK_0 z}, \qquad K_0 \equiv 2\pi/\Lambda_0 \tag{3.2}$$

$$K_{QPM} = m'K_0 = -\Delta k \tag{3.3}$$

where m' (integer) denotes the order of Fourier series component actually used in phase matching. If all the non-phase-matched components ($m \neq m'$) are neglected, we can formulate CW and pulsed SHG arising from uniform QPM gratings by replacing the effective nonlinear coefficient d_{eff} in Sec. 2.1 with the m'-th order projection $d_{eff}^{(m')}$, and validating perfect phase matching ($\Delta k=0$). In real applications, first-order QPM ($m'=\pm 1$) is preferred to maximize the effective nonlinearity as long as the modulation period Λ_o is practically achievable.

As in birefringence crystals, long uniform QPM gratings become problematic in generating ultrashort SH pulses. The output SH pulses can be spectrally truncated (equations (2. 39, 41)) and temporally stretched (eq. (2.51)) when the grating length L is too long to provide sufficient PM BW. As discussed in Sec. 2.2 and Sec. 2.3, the spectral truncation due to insufficient PM BW is detrimental in chromatic dispersion monitoring and intensity autocorrelation measurements. It is also understandable that FROG trace would be inappropriately filtered in the presence of narrow PM BW. As a consequence, we resort to manipulating the QPM grating function to broaden the PM BW without reducing the interaction length and SHG efficiency.

3.1.2 Chirped QPM gratings

We start with the generalized pulsed SHG theory capable of dealing with non-uniform effective nonlinear coefficient $d_{eff}(z)$, which was beyond the discussion of Sec. 2.1. For simplicity, we ignore the GVD effect, such that the output SH spectrum $\varepsilon_{2\omega}(L,\Omega)$ can be expressed as the product of nonlinear polarization spectrum $\varepsilon_\omega \otimes \varepsilon_\omega(\Omega)$ and PM spectrum $H_{2\omega}(\Omega)$ (eq (2.35)). The $sinc(\Delta kL/2)$ term in eq. (2.32) comes from integrating eq. (2.30) over the crystal length L (we use z=[-$L/2$, $L/2$] in the integration to eliminate the unimportant linear phase term, while still denoting the output position as $z=L$ for convenience) under the assumption of a constant d_{eff}:

$$\varepsilon_{2\omega}(L,\Omega) \propto \int_{-L/2}^{L/2} d_{eff} \cdot e^{j\Delta k(\Omega)\cdot z} dz \equiv H_{2\omega}(\Omega) \tag{3.4}$$

where $\Delta k(\Omega)$ is defined in eq. (2.33). In the presence of non-uniform $d_{eff}(z)$, eq. (3.4) can be generalized as a spatial Fourier transform relation:

$$\begin{aligned} H_{2\omega}(\Omega) &\propto \int_{-L/2}^{L/2} d_{eff}(z)\cdot e^{j\Delta k(\Omega)\cdot z}dz \\ &= F_z\left\{\Pi\left(\frac{z}{L}\right)\cdot d_{eff}(z)\right\}\Big|_{\substack{\eta\to \\ -\Delta k(\Omega)}} = \left\{L\widetilde{\Pi}(L\eta)\otimes \widetilde{d}_{eff}(\eta)\right\}\Big|_{\substack{\eta\to \\ -\Delta k(\Omega)}} \end{aligned} \tag{3.5}$$

where the square function Π is defined in eq. (2.52), $\widetilde{\Pi}(\eta)$ and $\widetilde{d}_{eff}(\eta)$ are spatial spectrum of $\Pi(z)$ and $d_{eff}(z)$, respectively.

We are especially interested in the case when $d_{eff}(z)$ is essentially periodic (with central period Λ_o), but has a slightly modulated envelope $d'_{eff}(z)$:

$$d_{eff}(z) \equiv d'_{eff}(z)\cdot e^{-jK_0 z} + c.c., \quad K_0 \equiv 2\pi/\Lambda_0 \tag{3.6}$$

If Λ_o is properly chosen such that K_o nearly cancels the intrinsic phase mismatch Δk, we can neglect the non-phase-matched term arising from $\left(d'_{eff}(z)\right)^*\cdot e^{jK_0 z}$:

$$\begin{aligned} H_{2\omega}(\Omega) &\propto \left\{L\widetilde{\Pi}(L\eta)\otimes \widetilde{d}'_{eff}(\eta+K_0)\right\}\Big|_{\substack{\eta\to \\ -\Delta k(\Omega)}} \\ &= \left\{L\cdot sinc(L\eta/2)\otimes \widetilde{d}'_{eff}(\eta)\right\}\Big|_{\substack{\eta\to K_0-\Delta k(\Omega) \\ =K_0-\Delta k-\Delta\left(v_g^{-1}\right)(\Omega-2\omega_0)}} \end{aligned} \tag{3.7}$$

where GVM factor $\Delta\left(v_g^{-1}\right)$ is defined in eq. (2.34), $\widetilde{d}'_{eff}(\eta)$ is the spatial spectrum of envelope pattern $d'_{eff}(z)$. The baseband PM spectrum $H(\omega)$ governing the SH spectral envelope $A_{2\omega}(L,\omega)$ (eq. (2.39)) is derived by shifting $H_{2\omega}(\Omega)$ for $2\omega_0$:

$$H(\omega) \propto \left\{L\cdot sinc(L\eta/2)\otimes \widetilde{d}'_{eff}(\eta)\right\}\Big|_{\substack{\eta\to \\ -\Delta\left(v_g^{-1}\right)(\omega-\widetilde{\delta})}} = F_z\left\{\Pi\left(\frac{z}{L}\right)\cdot d'_{eff}(z)\right\}\Big|_{\substack{\eta\to \\ -\Delta\left(v_g^{-1}\right)(\omega-\widetilde{\delta})}} \tag{3.8}$$

where the modified frequency detuning $\widetilde{\delta}$ due to residual phase mismatch is defined as:

$$\widetilde{\delta} \equiv \frac{K_0-\Delta k}{\Delta\left(v_g^{-1}\right)} \tag{3.9}$$

Eq. (3.8) indicates that PM spectrum $H(\omega)$ can be engineered by controlling $d'_{eff}(z)$, from which SH pulses with specified amplitude and phase can be generated (provided that input FH spectrum is broader than that of the SH output). For example,

one can compress SH pulses by engineering phase of $H(\omega)$ to compensate the chirped input FH pulses [21, 44-46]. In our applications, however, we do not care about the SH spectral phase but only about the SH power spectrum. In other words, technical effort should be dedicated to creating a broad PM power spectrum $|H(\omega)|^2$ by controlling $d'_{eff}(z)$. To this end, we can longitudinally change the QPM grating period, such that every local period $\Lambda(z)$ (with length l) contributes to a constituent PM spectrum $H_l(z,\omega)$ detuned by an angular frequency $\tilde{\delta}(z)$:

$$H_l(z,\omega) \propto l \cdot sinc\left(\frac{lT_s}{2L}(\omega - \tilde{\delta}(z))\right) \cdot e^{-j\left[\Delta\left(v_g^{-1}\right)z\omega/2\right]} \tag{3.10}$$

$$\tilde{\delta}(z) = \frac{K(z) - \Delta k}{\Delta\left(v_g^{-1}\right)} = \frac{2\pi}{\Delta\left(v_g^{-1}\right)}\left[\frac{1}{\Lambda(z)} - \frac{1}{\Lambda_0}\right] \tag{3.11}$$

where T_s is the GVM walk-off due to the entire grating length L (see eq. (2.37)), and the phase term in eq. (3.10) accounts for the local grating position, which is important in terms of complex superposition. As illustrated in Fig. 3.1 (using $\Delta\left(v_g^{-1}\right) < 0$ as in the case of $LiNbO_3$), shorter local period maps to a lower PM frequency component, while longer local period maps to a higher PM frequency component. The overall complex PM spectrum $H(\omega)$ is the superposition of all constituent spectra, which could be much broader than that of a uniform QPM grating of length L.

Fig. 3.2 demonstrates the simulation of the PM power spectrum $|H(\mathrm{f})|^2$ ($\mathrm{f} \equiv \omega/2\pi$) resulting from a linearly chirped QPM grating. The QPM period function is:

$$\Lambda(z) = \Lambda_0\left[1 + \left(\frac{\Delta\Lambda}{\Lambda_0}\right)\cdot\left(\frac{z}{L}\right)\right], \text{ for } |z| < L/2 \tag{3.12}$$

We use the following parameters in the simulation: central period Λ_0=14.74 μm, period modulation depth $\Delta\Lambda/\Lambda_0$= 0.0185, grating length L=59.5 mm, GVM parameter $\Delta\left(v_g^{-1}\right)$= −0.37 ps/mm. The resulting $|H(\mathrm{f})|^2$ has a BW Δf_{PM} of ~6.35 THz, corresponding to a PM tuning curve $|H_\omega(\lambda)|^2$ (see eq. (2.79)) centered at 1550 nm and having a BW $\Delta\lambda_{PM}$ of ~25 nm. Comparing with the spectral FWHM derived by a uniform QPM grating with identical length (Δf_{PM} ~40 GHz, $\Delta\lambda_{PM}$ ~0.17 nm), a relatively weak modulation depth

($\Delta\Lambda/\Lambda_0$=0.02) is sufficient to broaden the PM BW significantly (150 times). Consequently, chirped QPM grating technique is applicable to measuring ultrashort pulses with the detectable duration primarily limited by the GVD-induced input pulse distortion (see Chapter 5).

The ripple feature of Fig. 3.2 is attributed to the interference among the constituent PM spectra $H_l(z,\omega)$ (see eq. (3.10)) originated from different local positions z. Intuitively, the fine structure in $|H(\omega)|^2$ is associated with some sharp edge in $d'_{eff}(z)$. This is true in a QPM grating with finite length L and constant nonlinear strength d_{eff}, where $|d'_{eff}(z)|=d_{eff}\cdot\Pi(z/L)$. Imposing some apodization function on the nonlinear strength $|d_{eff}(z)|=|d'_{eff}(z)|$ (normally achieved by changing the duty cycle, [21]) can suppress the spectral fluctuation. For example, we can borrow the well-developed digital filter design technique to find a suitable $|d_{eff}(z)|$ profile with gradual transition from the "pass-band" ($|d_{eff}(z)|= d_{eff}$, for $|z|<z_p$) to the "stop-band" ($|d_{eff}(z)|= 0$, for $z_s<|z|<L/2$). Fig. 3.3a shows the simulated PM power spectrum $|H(\mathrm{f})|^2$ (solid curve) of a chirped QPM grating using an apodized $|d_{eff}(z)|$ derived by an M-th order finite-duration impulse response (FIR) digital low-pass filer (LPF) function with Hamming window [47]. We choose overlapped pass-band and stop-band edges ($z_p= z_s= 0.45L$), as well as a large filter order (M=100) to produce an apodization profile $|d_{eff}(z)|$ with steep yet smooth transition (see inset). Since the apodized $|d_{eff}(z)|$ can suppress the constituent PM spectra corresponding to grating periods outside the pass-band ($|z|>z_p$), the resulting PM BW $\Delta\mathrm{f}_{PM}$ of a linearly chirped QPM grating is expected to be reduced with apodization. The PM BW reduction, however, can be compensated by increasing the modulation depth ($\Delta\Lambda/\Lambda_0= 0.02$ in this case) of the linearly chirped period function $\Lambda(z)$ defined in eq. (3.12). Compared with the non-apodized case illustrated in Fig. 3.2 (shown as dotted curve in Fig. 3.3a), the resulting PM power spectrum $|H(\mathrm{f})|^2$ (solid curve) has a similar BW ($\Delta\mathrm{f}_{PM}$ ~6.3 THz) but is nearly ripple-free except for the two residual "ears" at the edges. The slight tilt between the "ears" is simply a result of nonlinear wave number distribution $K(z)=2\pi/\Lambda(z)$, though the QPM period $\Lambda(z)$ is linear. Further suppression of these spectral "ears" can be achieved by introducing a wider transition-band ($z_p<|z|<z_s$) for the apodization function

$|d_{eff}(z)|$. The PM power spectrum $|H(\mathrm{f})|^2$ (solid curve) shown in Fig. 3.3b is derived by using a $|d_{eff}(z)|$ (see inset) with z_p=0.2L, z_s= 0.4L, and M=100; while the modulation depth is increased to $\Delta\Lambda/\Lambda_0$= 0.033. We found that the spectral "ears" are significantly suppressed at the costs of wider transition (waste of PM BW) and smaller area (worse efficiency, as will be discussed in the following paragraph) in $|H(\mathrm{f})|^2$. In general, the ripple feature of $|H(\mathrm{f})|^2$ only has weak effect on the intensity autocorrelation measurement, for we only detect the spectral integral for each delay τ: $\overline{P}_{2\omega}(\tau) \propto \int_{-\infty}^{\infty} \left|P_{NL}(\omega,\tau)\right|^2 \cdot \left|H(\omega)\right|^2 d\omega$ (see eq. (2.42)). However, the nonlinear strength apodization is helpful in FROG measurements where any fluctuation of $|H(\mathrm{f})|^2$ may distort the measured spectrograms (see Sec. 4.1).

As far as efficiency is concerned, the QPM period chirping (without nonlinear strength apodization) still preserves the overall nonlinearity as the PM BW is broadened [48]. This is because the non-uniform QPM period $\Lambda(\mathrm{z})$ produces a distribution of wave number $K(z)$, which is equivalent to modulating the phase of effective nonlinear polarization:

$$d_{eff}(z) \approx d_{eff} \cdot e^{-jK(z)\cdot z} = d_{eff} \cdot e^{-j[2\pi z/\Lambda(z)]} \tag{3.13}$$
$$\Rightarrow d'_{eff}(z) = d_{eff} \cdot exp\left[2\pi z\left(\Lambda^{-1}(z) - \Lambda_0^{-1}\right)\right]$$

Although the PM spectrum $H(\omega)$ formulated in eq. (3.8) is changed due to this phase modulation, the area of $|H(\omega)|^2$ is invariant (Parseval's relation):

$$\int_{-\infty}^{\infty} \left|H(\omega)\right|^2 d\omega \propto \int_{-\infty}^{\infty} \left|\Pi(z/L)\cdot d'_{eff}(z)\right|^2 dz = L \cdot d_{eff}^2 = \text{constant} \tag{3.14}$$

The average SHG power $\overline{P}_{2\omega} \propto \int_{-\infty}^{\infty} \left|P_{NL}(\omega)\right|^2 \cdot \left|H(\omega)\right|^2 d\omega$ (see eq. (2.42)) is therefore independent of the period chirping, as long as the BW of $|H(\omega)|^2$ does not exceed that of $|P_{NL}(\omega)|^2$. This is entirely distinct from the traditional method of achieving broad PM BW by using shorter nonlinear crystal. As shown in equations (2.37, 41), decreasing the crystal length L by a factor of N will simultaneously broaden the PM BW ($\propto 1/T_S$) and degrade the PM spectral amplitude $|H(\omega)|$ by the same factor of N. Consequently, the underlying spectral area of $|H(\omega)|^2$ turns out to be decreased by a factor of N. Fig. 3.4

compares the difference between the two schemes. As a result, the QPM period chirping in collaboration with the waveguide structure distinguish our scheme from the conventional techniques by orders of magnitude in terms of sensitivity improvement.

We should notice, however, the nonlinear strength apodization can reduce the overall nonlinearity due to the lesser area under $|d_{eff}(z)|^2$ ($\propto$ area under $|H(\omega)|^2$). This efficiency reduction paid for suppressing the ripple feature of PM power spectrum $|H(\omega)|^2$ is usually not large. For example, the area under the curve in Fig. 3.3a-b remain 88% and 54% of that in Fig. 3.2, while the spectral fluctuations have been nearly eliminated.

3.1.3 QPM $LiNbO_3$ waveguide sample

The waveguide sample used in our experiments was fabricated by Krishnan R. Parameswaran in the E. L. Ginzton Laboratory of Stanford University, Stanford, California. It was made by periodic electric field poling [49] and annealed proton exchange (APE) [20] in a z-cut $LiNbO_3$ substrate, in which only extraordinary index is increased ($\Delta n_e \approx 0.09$) and supports a single TM (z-polarized) mode. More advanced reverse proton exchange (RPE) process [50] has been developed to form a buried waveguide with symmetric index profile in depth, which can improve the SHG efficiency over that of the APE guides by more than threefold. Mode filters and tapers are used to match the mode size of single mode fiber at the two ends for better coupling efficiency, and downsize the mode in the grating region to increase the nonlinear interaction (see Fig. 3.5) [20]. Considering the coupling loss and propagation loss (~0.43 dB/cm at 1550-nm wavelength), our free-space-coupled waveguide sample has a total loss of ~8.5 dB. Newer fiber-pigtailed waveguide device like that used in [2] can reduce the value to 2~3 dB.

The largest nonlinear tensor component of $LiNbO_3$ (d_{33}=27 pm/V) is exploited for SHG by coupling a z-polarized beam (s-wave) into the waveguide, and producing an SH beam also polarized in z-direction. The central poling period Λ_o is about 14 μm, designed for phase matching a fundamental wavelength λ_{PM} =1538 nm in room temperature. Heating the sample with a temperature-controlled oven can shift the central PM wavelength longer (~0.1 nm/^{o}C). This is attributed to temperature-dependent effective

index of waveguide mode and the thermal expansion of the QPM grating [51]. The poling region of the waveguides is 5.95-cm-long, contributing to a 22-ps GVM walkoff (GVM parameter $\Delta\left(v_g^{-1}\right)$ in waveguides is -0.37 ps/mm).

Fig. 3.5 shows the experimental setup for characterizing the SHG PM tuning curve (eq. (2.79)). We coupled the optical beam from a tunable CW laser into the waveguide, and measured the output SHG power as a function of input wavelength. Fig. 3.6a demonstrates that an unchirped QPM $LiNbO_3$ (or periodically-poled lithium niobate, PPLN) waveguide has a $sinc^2$ PM tuning curve with a peak response near 2000 %/W and an FWHM of 0.17 nm, (PM BW Δf_{PM} working on the SH band is 42 GHz, consistent with the 22-ps GVM walkoff). Measurements of subpicosecond pulses with such a waveguide would be subject to serious distortion [11]. A series of chirped QPM $LiNbO_3$ (or aperiodically-poled lithium niobate, A-PPLN) waveguides are fabricated on the same $LiNbO_3$ sample with PM tuning curve widths ($\Delta\lambda_{PM}$) of 5-, 10-, 15-, 20-, and 25-nm, depending on the modulation depth of the linear QPM period chirping function. Fig. 3.6b–c illustrate the PM tuning curves of two differently chirped QPM $LiNbO_3$ waveguides used in chromatic dispersion monitoring and intensity autocorrelation experiments, respectively. Their widths are 5 nm and 25 nm, which are sufficient to accurately characterize BW-limited pulses with durations longer than ~700 fs and ~140 fs, respectively. By considering the spectral width and height in these three PM tuning curves, we found that the spectral area is roughly independent of the QPM period chirping, which is in agreement with the conclusion in Sec. 3.1.

3.2 Chromatic Dispersion Monitoring Experiments

Chromatic dispersion monitoring and dynamic compensation in optical fiber communication systems become essential as the channel bandwidth exceeds 40 Gbit/s, for the environmental perturbations along a long fiber link and dynamic change of optical path in a reconfigurable network can change the accumulated dispersion of a channel beyond the limited tolerance [52-53]. In real applications, monitoring should tap off less

than 1-3% of the transmitted power, and the detection response should be faster than the time scale of dispersion variation (~100 ms) to support real-time performance recovery [19]. In previous discussions, we showed that SHG yield of short pulses is sensitive to the nonlinear spectral phase, and the chirped QPM $LiNbO_3$ waveguides have very high SHG efficiency. In this section, we would like to experimentally demonstrate dispersion monitoring of 10-GHz, 3-ps pulse train at –45 dBm coupled average power and 100-ms sampling period using our chirped QPM $LiNbO_3$ waveguides [25-26].

Fig. 3.7 shows the experimental apparatus. An actively mode-locked fiber laser produces 10-GHz, 3-ps (duty cycle d ~3%), nearly BW-limited pulses centered at λ_0 = 1542 nm. We use a Fourier transform pulse shaper (constructed by Zhi Jiang, with a resolution of ~17-GHz/pixel) [27-28] to apply variable quadratic spectral phases $\exp[j\alpha\omega^2]$ to the optical pulses in order to simulate the accumulated dispersion D of real fiber links, where D is related to α via:

$$D \approx -4\pi c\alpha/\lambda_o^2 \text{ , } c \text{ is the speed of light} \qquad (3.15)$$

The pulses are coupled into a chirped QPM waveguide with PM tuning curve width $\Delta\lambda_{PM}$ ~5 nm (PM BW Δf_{PM} ~1.25 THz, see Fig. 3.6b), which is sufficient to cover the entire nonlinear polarization spectrum (FWHM ~300 GHz). We use a polarization controller to maximize the nonlinear yield; however, polarization-insensitive schemes can be achieved by either a configuration consisting of double waveguides and polarization beam splitters [54], or a fast polarization scrambler incorporated prior to the waveguide at the cost of small decrease in sensitivity. The output SHG signal is detected by a PMT along with a lock-in amplifier at a sampling period of 100-ms.

To illustrate the ultimate sensitivity of this scheme, we measured the SHG power $P_{2\omega}$ using dispersion-free pulses (shaper inactive) at different coupled input powers P_ω. The log-log plot (Fig. 3.8) is fit well by a line with a slope of 1.95 over the 14.7-dB range of input powers, in good agreement with the expected slope of 2 for SHG. The fit line indicates that we can get a PMT dark-noise-limited signal-to-noise ratio (SNR) of 10 dB with less than –47 dBm input power and 100-ms sampling period. In our experiments, the

residual background light, input power fluctuations, and a margin for dispersion measurement slightly increase the required power.

The constant slope of 2 in Fig. 3.8 (the quadratic relation of $P_{2\omega} \propto P_{\omega}^2$) is expected to be valid for higher input power until (i) the SHG conversion efficiency η_{SHG} is no longer weak, which partially depletes the power of input pulse; or (ii) the induced self-phase modulation (SPM) becomes noticeable, which changes the spectrum of the input pulse. Our data predict that the quadratic relation of $P_{2\omega} \propto P_{\omega}^2$ still holds at a maximum input power P_{ω} of ~ 0 dBm, if the typical criterion of η_{SHG} <1% is applied [12, 55]. This permits a much larger (>45 dB) input power bias range for dispersion monitoring than those using TPA in Si:APD (< 20 dB) [14] and GaAs PMT (< 30 dB) [15].

Fig. 3.9 shows normalized SHG power $P_{2\omega}$ (circles) generated by the differently chirped pulses as a function of accumulated dispersion D, at fixed –45 dBm input power. The measurement SNR (at 10-Hz sampling BW) is about 13 dB (see error bar) for the dispersion-free pulses. We also measured the pulse widths Δt (asterisks) using intensity autocorrelation, and the product of $P_{2\omega}$ and Δt nearly remains constant for all dispersion values, confirming the integrity of our experimental data. The asymmetric feature of Fig. 3.9 is attributed to the uneven PM spectrum of the chirped QPM waveguide, as well as the residual cubic phase and spectral asymmetry of the input pulses.

In real communication systems, signal pulses with duty cycle d larger than 3% are normally used to improve the spectral efficiency. Quantitatively, the required average power $\overline{P}_{\omega}$ to generate detectable SHG signal depends on the sensitivity S (in mW^2) of the detection scheme (defined in eq. (2.48)) and the duty cycle d via:

$$\overline{P}_{\omega} \approx \sqrt{S \cdot d} \tag{3.16}$$

According to the discussions in Sec. 2.2 and Sec. 3.1.2, a PM BW Δf_{PM} (controlled by the QPM chirp rate) just covering the nonlinear polarization spectrum $P_{NL}(\omega)$ would avoid SHG signal distortion due to insufficient PM BW and give rise to the best sensitivity S (requiring the least power $\overline{P}_{\omega}$). Overextending the PM BW by a factor of N allows diagnosis of ~N distinct wavelength division multiplexing (WDM) channels

(one at a time) at the cost of $\sqrt{N}$ times more $\overline{P}_{\omega}$. If the sensitivity *S* is kept constant by properly choosing PM BW Δf_{PM}, we can easily estimate that the required $\overline{P}_{\omega}$ would increase to –40 dBm when the pulse duration is increased to 24 ps (*d*~24%) at the same (10-GHz) repetition rate. In this case, however, the spectral resolution of our pulse shaper (~17 GHz/pixel) is insufficient to noticeably affect the SHG signal by quadratic phase modulation. Alternatively, we verified the power requirement $\overline{P}_{\omega}$ at *d*~24% by performing intensity autocorrelation measurements, where the 24-ps pulse train is produced by spectrally filtering the laser source using the amplitude modulation functionality of the pulse shaper. Fig. 3.10 illustrates two autocorrelation traces obtained by an unchirped QPM waveguide (PM BW Δf_{PM} is somewhat broadened to ~63-GHz due to non-uniform temperature distribution) with coupled powers of –31 dBm (solid) and –40 dBm (dashed), respectively. The deconvolved pulse durations (assuming a Gaussian profile) are in good agreement: 23.5 ps and 24.4 ps, respectively. We measured a PMT dark-noise-limited SNR of 13 dB at 10-Hz sampling BW for –40.5 dBm unchirped pulses. These results agree with the theoretical prediction based on eq. (3.16).

In conclusion, we have used QPM $LiNbO_3$ waveguides to demonstrate ultra-sensitive dispersion monitoring for 10-GHz, 3-ps pulse train at an unprecedented low input power level of **–45 dBm** (**32 nW**) and **100-ms** sampling period. The feasibility of monitoring 10-GHz, 24-ps pulses is also experimentally verified by intensity autocorrelation at **–40 dBm** (TPA in Si/APD only permits dispersion monitoring at average power of –16 dBm [56]). The QPM waveguide scheme is bit-rate transparent, applicable to return-to-zero (RZ) and carrier-suppressed-RZ modulation formats [56], and can monitor distinct WDM channels with a single device by choosing adequate PM BW. It can also be applied together with previously reported techniques to identify the sign of dispersion [57], and for more generalized optical performance monitoring [56].

3.3 Intensity Autocorrelation Experiments

Fig. 3.11 illustrates the experimental setup for intensity autocorrelation measurements. A passively mode-locked fiber laser produces a ~220-fs pulse train, with 50-MHz repetition rate, 1545-nm central wavelength, and ~11-nm spectral width. Spectral amplitude and phase modulations of the pulses are applied by using a reflective type Fourier pulse shaper [27-28] right after the laser output. The pulses are relayed through a dispersion compensated fiber link into a collinear-type autocorrelator with a time delay resolution of 0.67 fs. Polarization of the pulses is controlled to be z-polarized (along the optical axis of $LiNbO_3$) before being coupled into the selected waveguide. The sample is heated to 84^{o}C to shift the central PM wavelength to 1545 nm (Fig. 3.6c). A non-cooled photomultiplier tube (PMT) along with a lock-in amplifier are used to detect the average SHG power down to the order of femtowatt. The typical data acquisition (DAQ) time for each trace is less than 3 minutes. The interferometric fringes and the collinear signal background of the raw trace are removed by software to yield background-free autocorrelation function $G_2(\tau)$.

Fig. 3.12 illustrates two autocorrelation traces obtained by a chirped QPM $LiNbO_3$ waveguide with a PM tuning curve width $\Delta\lambda_{PM}$ ~25 nm. The energies per pulse coupled into the waveguide U (referring to the total of those from both autocorrelator arms) are 12 fJ (solid) and **52 aJ** (dotted), respectively. The latter corresponds to **400-photons per pulse** (photon energy ~0.128 aJ at 1545-nm wavelength), 0.24-mW peak power, and 1.3-nW average power. This corresponds to an unprecedented measurement sensitivity of $\mathbf{3.2 \cdot 10^{-7}\ mW^2}$. Even with a 23-dB input power difference (46-dB difference for SHG powers), these two curves agree extremely well. The deconvolved pulse durations Δt (assuming a $sech^2$-profile) are essentially identical: 215 fs and 214 fs, respectively.

To further confirm the accuracy of our traces, we also performed autocorrelation measurements using a standard bulk nonlinear crystal: a 1-mm-thick lithium iodate ($LiIO_3$) crystal with 88-fs GVM walkoff and 40-nm PM tuning curve BW. Since the temporal walkoff is less than the input pulse duration, the resulting trace should have

negligible distortion. Fig. 3.13 compares autocorrelation traces obtained by the bulk $LiIO_3$ (dashed) and our chirped QPM $LiNbO_3$ waveguide ($\Delta\lambda_{PM}$ ~25 nm, dotted). There is no noticeable difference between them even though the chirped QPM $LiNbO_3$ waveguide has an enormous GVM walkoff (22 ps). This is attributed to the fact that accurate autocorrelation measurements require only sufficient PM BW regardless of the GVM, a concept similar to that which has been applied in the GRENOUILLE scheme [58] of frequency-resolved optical gating (FROG).

We also experimentally demonstrated that insufficient PM BW could distort the autocorrelation traces. Fig. 3.14 illustrates the deconvolved pulse durations Δt at several temperature values T for both unchirped (circle) and chirped (cross) QPM $LiNbO_3$ waveguides. Traces of unchirped QPM waveguide show strong temperature dependence, where Δt ranges from 235 fs to 166 fs during a temperature change of 55°C. In contrast, chirped QPM waveguide is almost insensitive to the temperature variation (Δt only differ by a few fs). This result reflects that a narrowband PM spectrum $H(\omega)$ cannot sense the entire nonlinear polarization spectrum $P_{NL}(\omega)$, which is essential to retrieve the correct intensity autocorrelation function. As the central PM wavelength λ_{PM} changes with crystal temperature, the narrow PM spectrum $H(\omega)$ "samples" different frequency bands of $P_{NL}(\omega)$, from which distinct pulse information and correlation widths are derived.

Another evidence is illustrated in Fig. 3.15, where the deconvolved pulse durations derived by both unchirped and chirped QPM $LiNbO_3$ waveguides are shown for different chirping strengths of input pulse. We used a pulse shaper to generate a nonlinearly chirped Gaussian spectrum:

$$A(\lambda) = exp\left[-\left(\frac{\lambda-\lambda_o}{\Delta\lambda}\right)^2\right]\cdot exp\left[j\beta\pi\left(\frac{\lambda-\lambda_o}{\Delta\lambda_{shaper}}\right)^3\right] \tag{3.17}$$

where central wavelength λ_o=1542 nm, spectral intensity FWHM = $\Delta\lambda\cdot\sqrt{2\cdot\ln 2}$ = 9 nm, shaper BW $\Delta\lambda_{shaper}$= 9.2 nm, β represents the cubic phase modulation depth. The shaped pulse is temporally broadened with the increase of chirping strength β (see the squares in the figure derived by simulation assuming infinite PM BW). This trend is sensed by

chirped QPM waveguide ($\Delta\lambda_{PM}$ ~25 nm) where the deconvolved Δt (cross) considerably increases (460 fs → 810 fs) with β (0 → 2). In contrast, Δt (circle) is only slightly changed (460 fs → 490 fs) when using unchirped QPM waveguide ($\Delta\lambda_{PM}$ ~0.17 nm). This result agrees with the fact that autocorrelation traces with narrow PM BW are insensitive to the any odd-order spectral phases (cubic in our experiment). The deviation (~14%) between the simulation and chirped QPM experiment at large chirp (β=2) is attributed to: (i) imperfect Gaussian spectrum generated by the shaper, (ii) finite PM BW ($\Delta\lambda_{PM}$ ~25 nm), (iii) uneven PM curve of the chirped QPM waveguide; which are no longer negligible for highly chirped pulses.

Another important observation is that the chirped QPM waveguides retain almost the same efficiency for short pulses as the unchirped QPM guide, which has been preliminarily discussed in Sec. 3.1.2. Recalling eq. (2.42), the SH pulse energy $U_{2\omega}$ is proportional to the overlap integral of two power spectra: $|P_{NL}(\omega)|^2$ and $|H(\omega)|^2$. If the nonlinear polarization power spectrum $|P_{NL}(\omega)|^2$ is constant, $U_{2\omega}$ is simply proportional to the area under the PM power spectrum $|H(\omega)|^2$. As indicated before, chirping the poling period ideally does not change this area (eq. (3.14)); therefore $U_{2\omega}$ is independent of the PM BW broadening caused by the chirped QPM grating. In practice $U_{2\omega}$ may decrease slowly with the PM BW broadening due to the gradual roll-off of $|P_{NL}(\omega)|^2$. However, this efficiency degradation remains weak provided that the PM BW is not made much broader than the nonlinear polarization spectral width. Fig. 3.16 demonstrates the dependence of SHG efficiency on PM BW, obtained experimentally by using QPM waveguides with different chirps. For example, with a PM tuning curve BW $\Delta\lambda_{PM}$ ~15 nm (broader than the FH power spectral FWHM $\Delta\lambda$~13 nm), the SHG efficiency is still ~60% compared to an unchirped QPM waveguide, though the BW is broadened by 60 times. Even with further broadening the $\Delta\lambda_{PM}$ to 25 nm (150 times wider than the unchirped QPM counterpart), a relative SHG efficiency of ~40% is retained. This trend agrees with simulations (shown as circles in Fig. 3.16), where we assumed the pulse is BW-limited with a power spectrum identical with that measured in the experiment, and the PM power spectrum $|H(\omega)|^2$ has a square shape. In general, using a chirped QPM

waveguide with $\Delta\lambda_{PM} \approx \Delta\lambda$ would enable accurate traces and best efficiency. As a consequence, one has to characterize the PM tuning curves and FH power spectrum to select an optimal (available) QPM waveguide for real measurements.

In conclusion, our experiments demonstrate the record sensitivity (**$3.2 \cdot 10^{-7}$ mW^2**) for intensity autocorrelation measurements by chirped QPM $LiNbO_3$ waveguides, improving on the previous record by **500 times**. The obtained trace is in good agreement with that from a bulk $LiIO_3$. Measurement distortion due to insufficient PM BW is demonstrated by the strong temperature dependence of deconvolved pulse duration and the insensitivity to the cubic spectral phase of the input pulses. We also demonstrate that PM BW broadening by chirping QPM periods does not significantly sacrifice the SHG efficiency until it is much broader than the BW of nonlinear polarization, making the chirped QPM waveguides extremely suitable for pulse measurements.

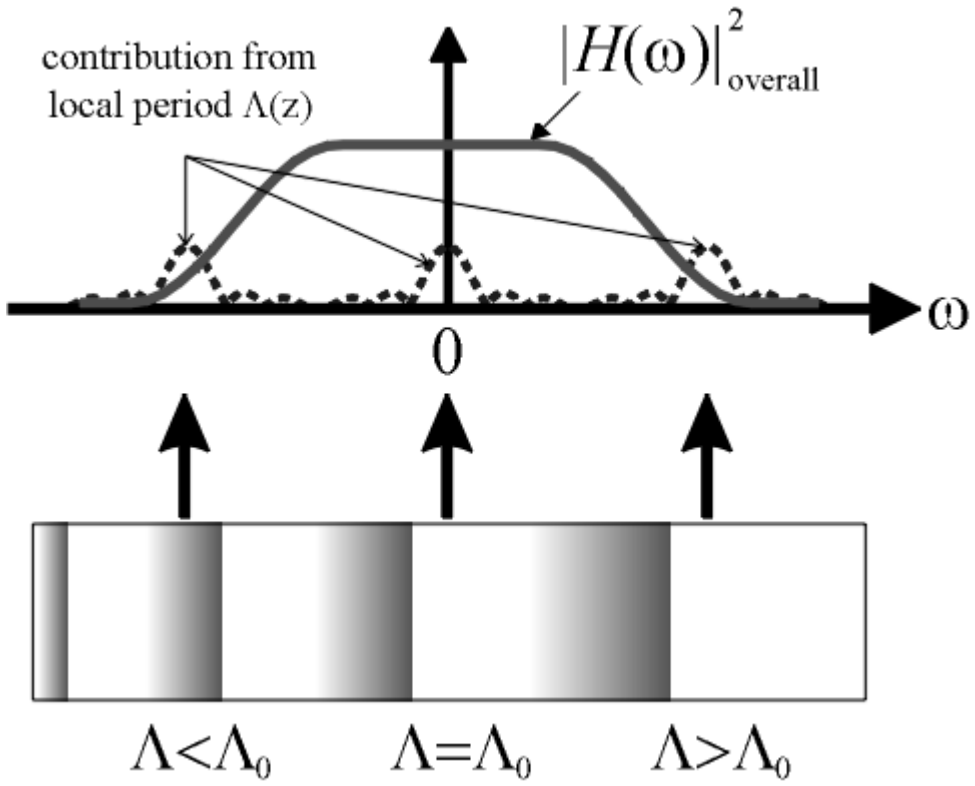

Fig. 3.1. Concept of PM BW broadening by longitudinally changing the QPM grating period $\Lambda(z)$. Λ_0 is the central QPM period used to compensate the intrinsic phase mismatch Δk. The dashed curves represent the constituent spectra corresponding to three different local periods. The solid curve is the overall PM power spectrum of the chirped QPM grating. We assume $\Delta\left(v_g^{-1}\right) < 0$, as in the case of $LiNbO_3$.

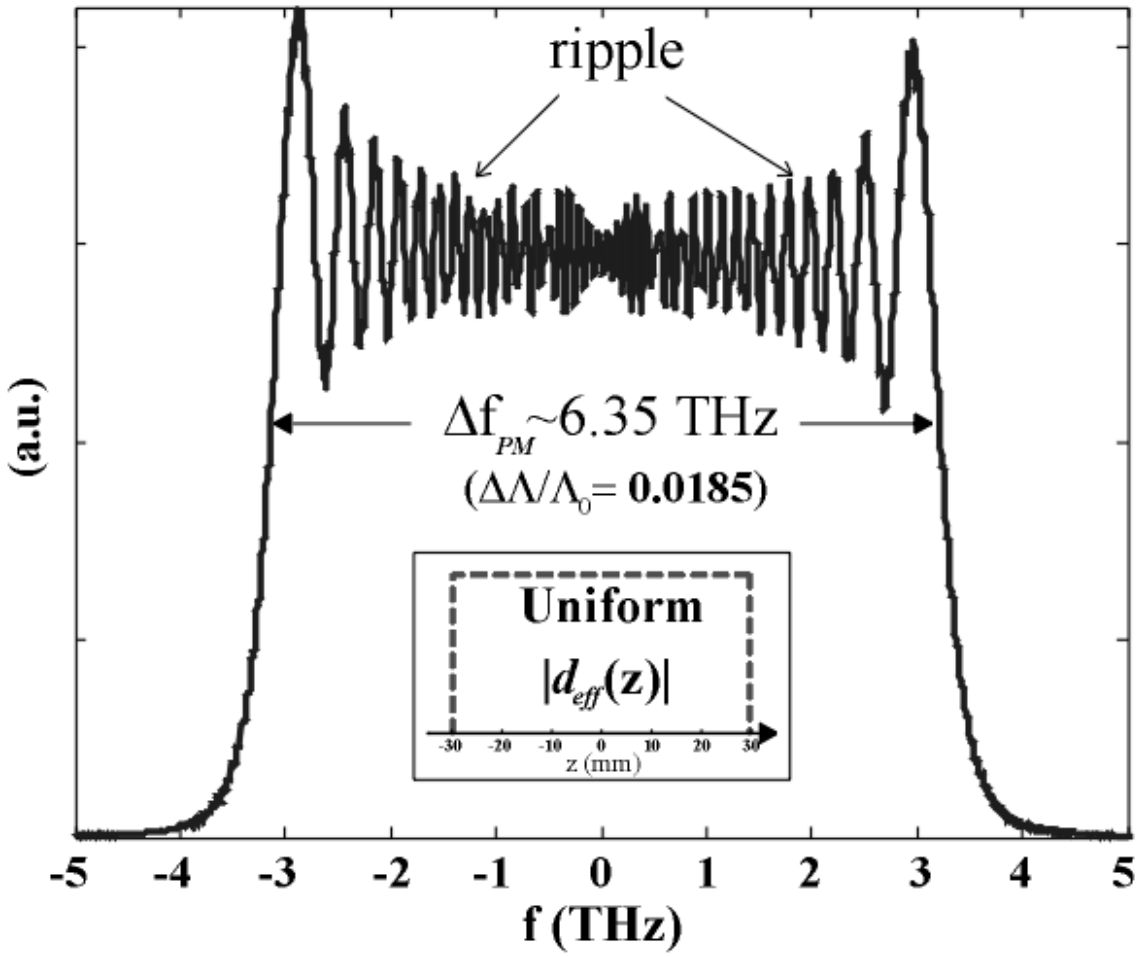

Fig. 3.2. PM power spectrum $|H(\mathrm{f})|^2$ resulting from a QPM grating with uniform nonlinear strength $|d_{eff}(z)| \propto \Pi(z/L)$ (see inset) and linearly chirped period $\Lambda(z)= \Lambda_0\cdot[1+(\Delta\Lambda/\Lambda_0)\cdot(z/L)]$, where $\Lambda_0 = 14.75$ μm, $\Delta\Lambda/\Lambda_0 = 0.0185$, $L = 59.5$ mm. The GVM parameter of the crystal is assumed as $\Delta\left(v_g^{-1}\right) = -0.37$ ps/mm. The resulting PM BW Δf_{PM} is ~6.35 THz, which is ~150 times broader than that derived by a uniform QPM grating ($\Lambda(z)= \Lambda_0$, Δf_{PM} ~40 GHz). The ripple feature is attributed to the sharp edges of $|d_{eff}(\mathrm{z})|$ at $z = \pm L/2$, and interference among the constituent PM spectra originated from different local positions z.

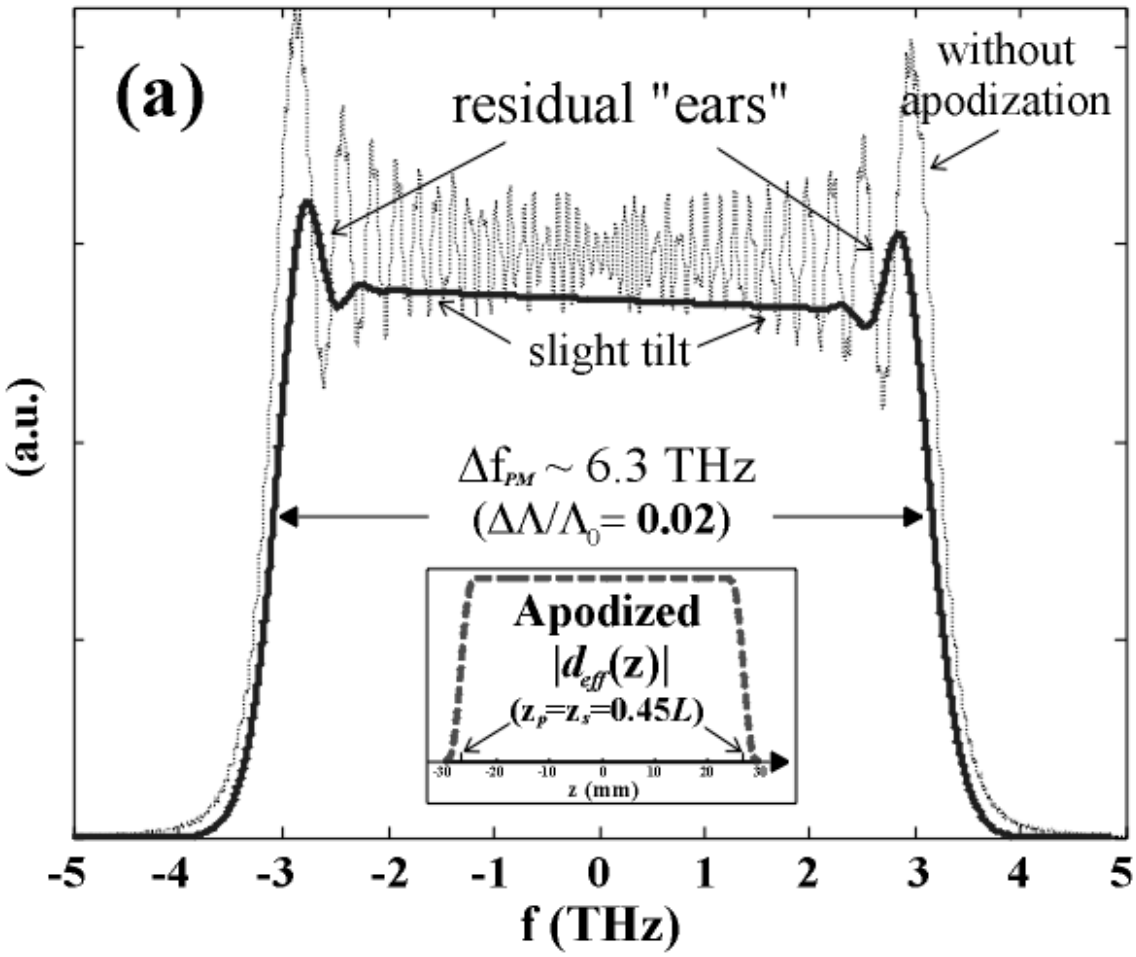

Fig. 3.3a. PM power spectrum $|H(\mathrm{f})|^2$ (solid curve) of a QPM grating with apodized nonlinear strength $|d_{eff}(z)|$ and linearly chirped period $\Lambda(z)= \Lambda_0\cdot[1+(\Delta\Lambda/\Lambda_0)\cdot(z/L)]$, where $\Lambda_0 = 14.75$ μm, $\Delta\Lambda/\Lambda_0 = 0.02$, $L= 59.5$ mm. The GVM parameter $\Delta\left(v_g^{-1}\right)$ is assumed as −0.37 ps/mm. The $|d_{eff}(z)|$ is derived by a 100-th order finite-duration impulse response (FIR) digital low-pass filter (LPF) function with "cut-off" at $|z|= z_p= z_s=0.45L$ and a Hamming window (inset). Compared with the non-apodized case in Fig. 3.2 (shown as dotted curve here), the PM BW Δf_{PM} remains ~6.3 THz, but the ripple feature in Fig. 3.2 is suppressed except for the two residual "ears" at the band edges. The slight tilt between the "ears" arises from the nonlinear wave number distribution $K(z)=2\pi/\Lambda(z)$, though $\Lambda(z)$ is linear. The overall nonlinearity ($\propto$ area under $|H(\mathrm{f})|^2$) remains 88% of that in Fig. 3.2 (the solid and dotted curves use the same vertical scale).

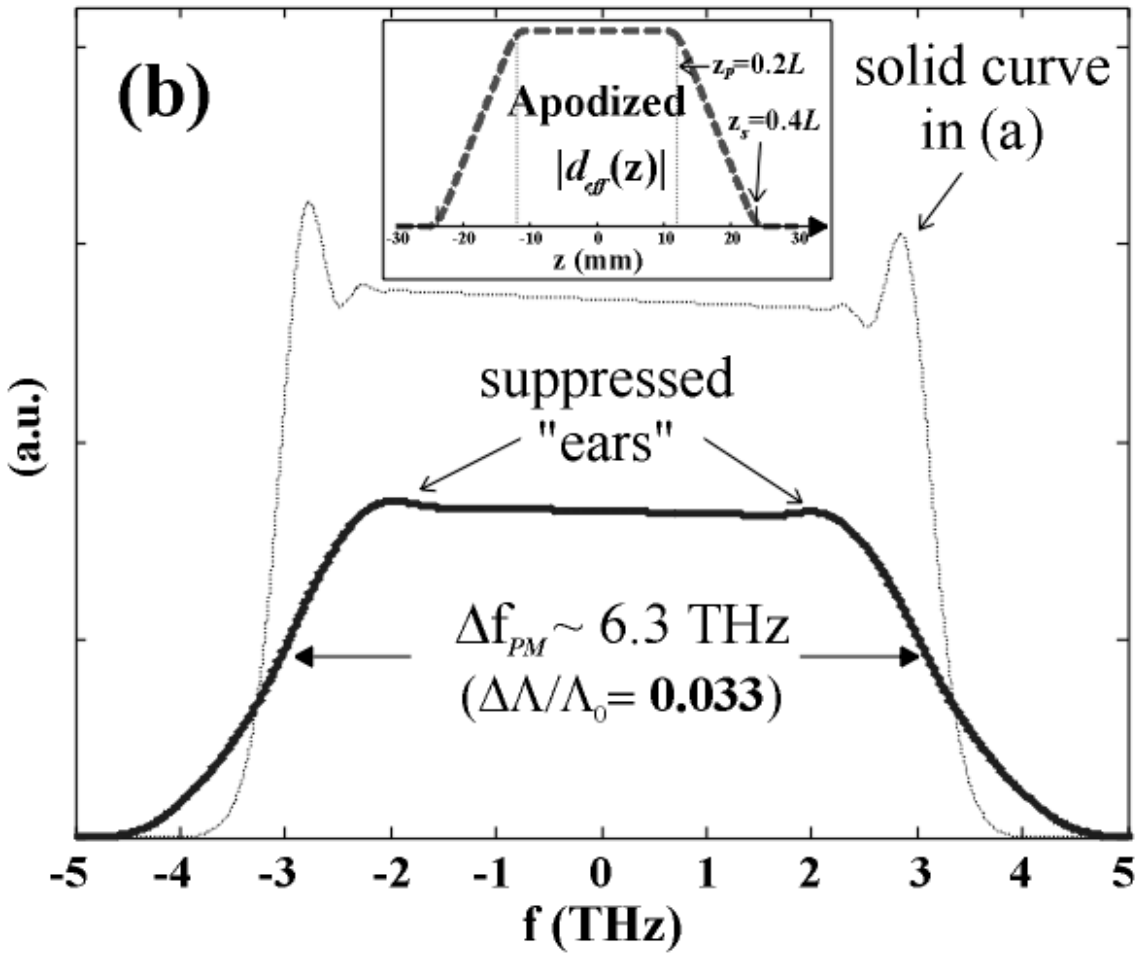

Fig. 3.3b. PM power spectrum $|H(f)|^2$ (solid curve) of a chirped QPM grating with nonlinear strength apodization. The grating parameters are identical with those in Fig. 3.3a, except for: (i) larger grating period modulation depth $\Delta\Lambda/\Lambda_0 = 0.033$, and (ii) wider transition-band ($z_p<|z|<z_s$, $z_p = 0.2L$, $z_s=0.4L$) in apodization profile $|d_{eff}(z)|$ (inset). Compared with Fig. 3.3a (shown as dotted curve here), the spectral "ears" are significantly suppressed, but $|H(f)|^2$ has wider transition and smaller overall nonlinearity (54% of that in Fig. 3.2).

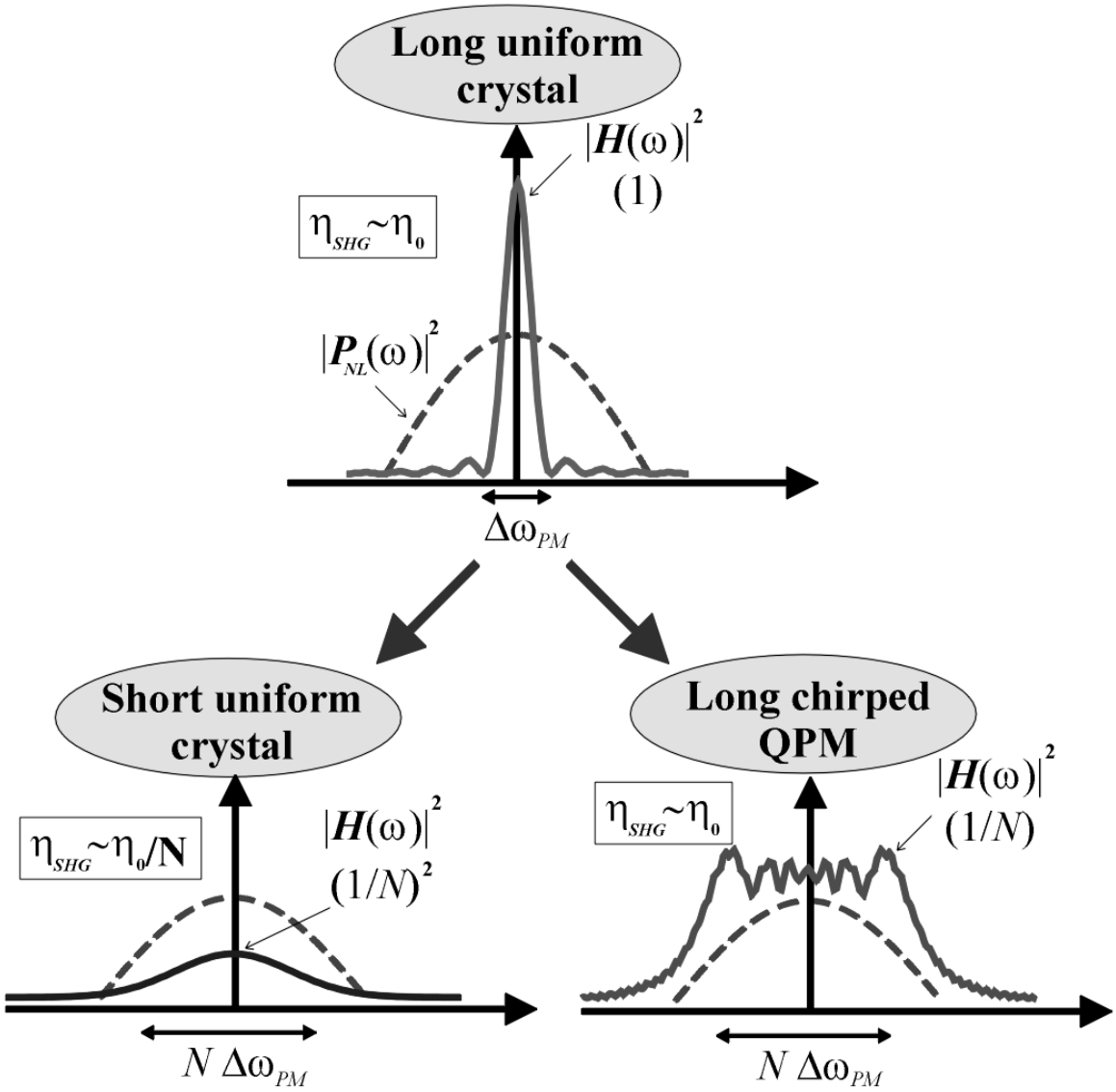

Fig. 3.4. Concept of PM BW broadening with (lower left) and without (lower right) SHG efficiency η_{SHG} degradation in two different schemes. A long uniform crystal (upper subfigure) produces a PM power spectrum $|H(\omega)|^2$ with large peak (1) but narrow BW ($\Delta\omega_{PM}$). Shortening the crystal length by a factor of N would decrease the peak of $|H(\omega)|^2$ to $(1/N)^2$ and broaden the BW to $N\Delta\omega_{PM}$, resulting in an efficiency reduction of N times. In contrast, using a long chirped QPM grating designed for a PM BW of $N\Delta\omega_{PM}$ simply decreases the peak $|H(\omega)|^2$ to $1/N$, and preserves the efficiency.

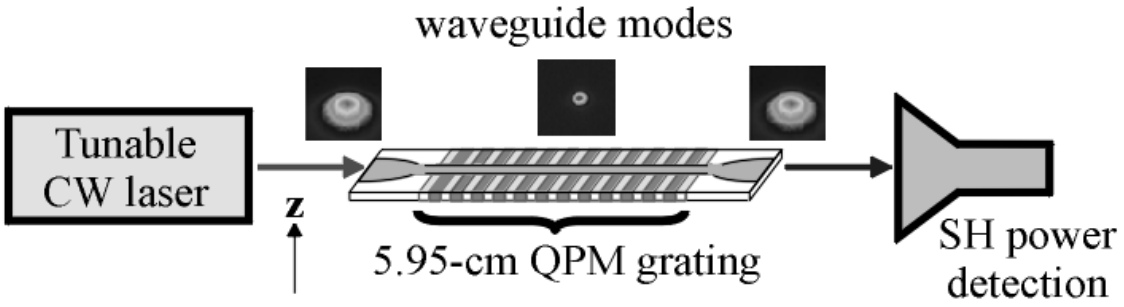

Fig. 3.5. Experimental setup for characterizing the PM tuning curve of the QPM $LiNbO_3$ waveguides. The waveguide modes are larger at the two ends to match that of the single mode fiber, while smaller during the grating region to increase the nonlinear interaction. Both FH and SH waves are z-polarized (direction is shown in the figure).

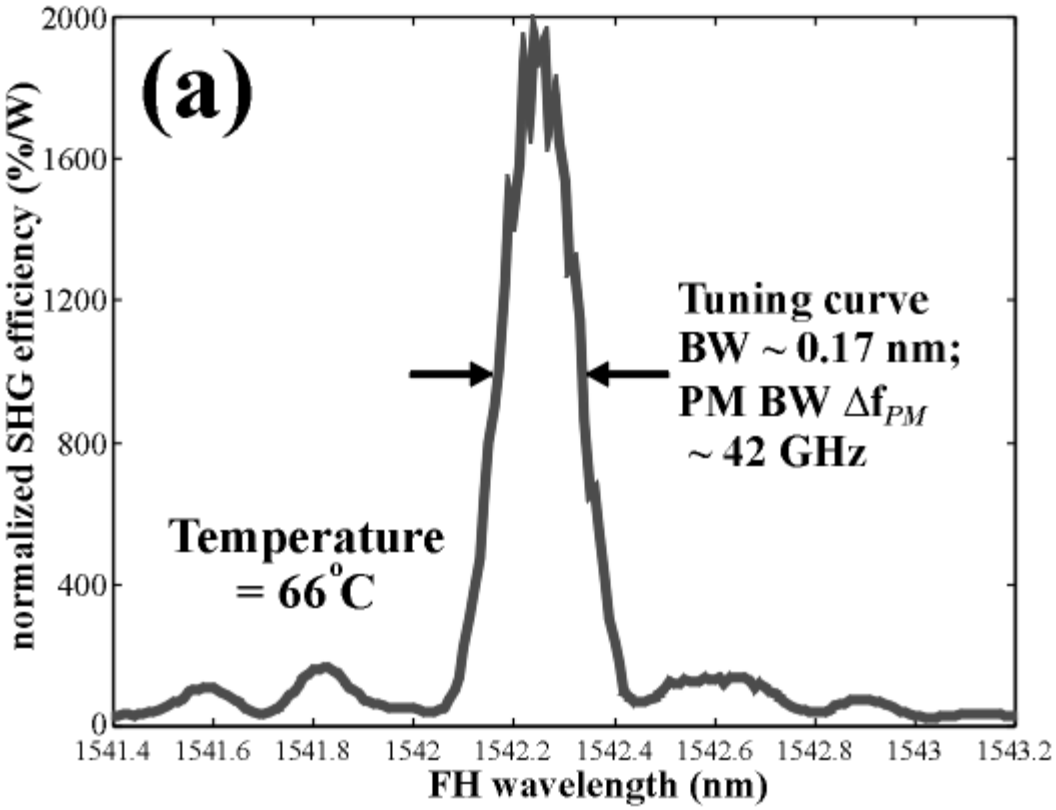
(a)
normalized SHG efficiency (%/W)
2000
1600
1200
800
400
0
Tuning curve
BW ~ 0.17 nm;
PM BW Δf_PM
~ 42 GHz
Temperature
= 66°C
1541.4
1541.6
1541.8
1542
1542.2
1542.4
1542.6
1542.8
1543
1543.2
FH wavelength (nm)

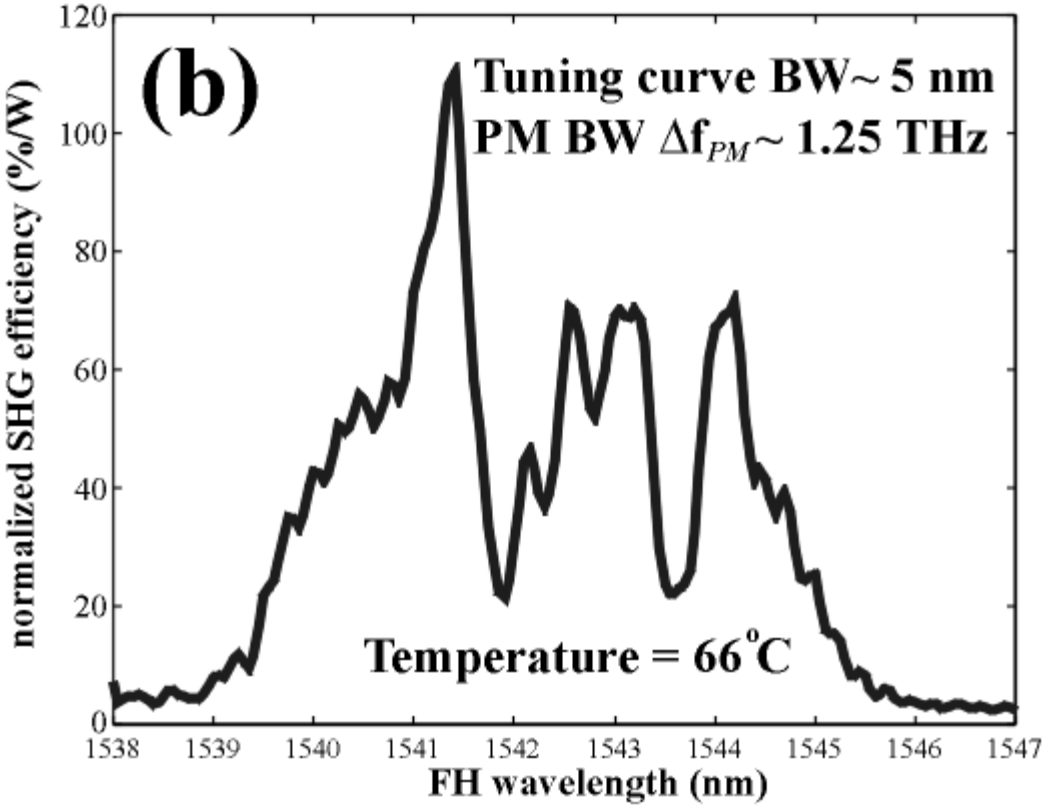
(b)
Tuning curve BW~ 5 nm
PM BW Δf_PM~ 1.25 THz
normalized SHG efficiency (%/W)
120
100
80
60
40
20
0
Temperature = 66°C
1538
1539
1540
1541
1542
1543
1544
1545
1546
1547
FH wavelength (nm)

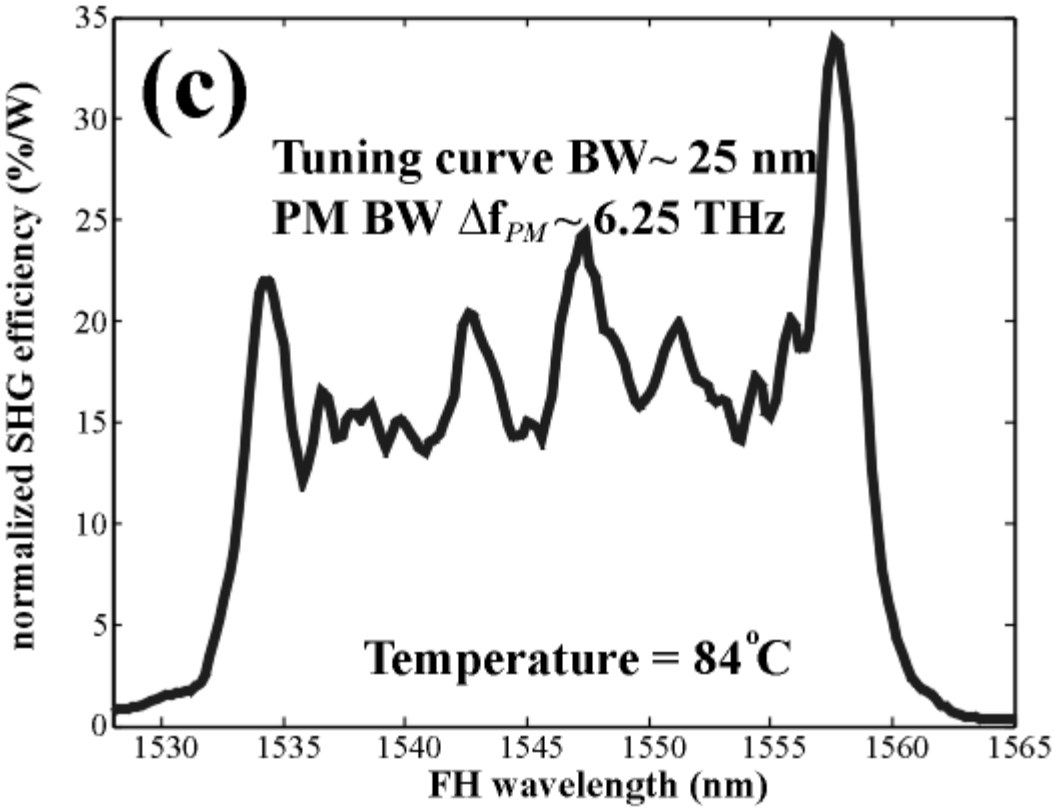

Fig. 3.6. Measured PM tuning curves of QPM $LiNbO_3$ waveguides with: (a) uniform, and (b-c) linearly chirped periods. The sample temperatures are: (a-b) 66°C, and (c) 84°C, shifting the central PM wavelengths to 1542 nm and 1545 nm, respectively. The vertical axis gives the normalized SHG efficiency in (%/Watt). The tuning curve bandwidths (0.17 nm, 5 nm, 25 nm) are increased with QPM period chirping, while the overall nonlinearities (proportional to the spectral area of the curve) are roughly the same.

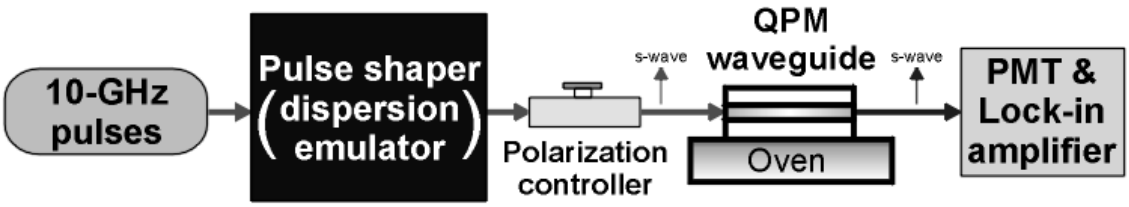

Fig. 3.7. Experimental apparatus for chromatic dispersion monitoring. PMT stands for photomultiplier tube.

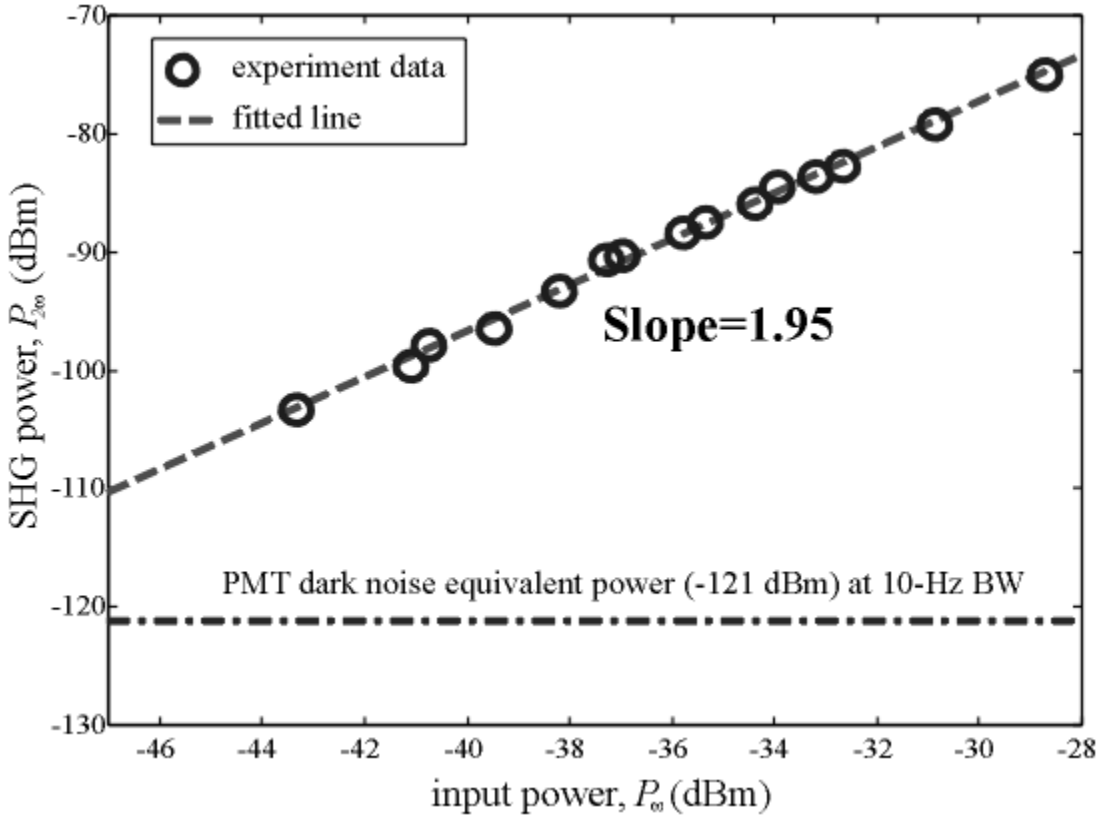

Fig. 3.8. Log-log plot of SHG power $P_{2\omega}$ versus coupled input power P_{ω} when dispersion-free pulses are sent into the chirped QPM waveguide.

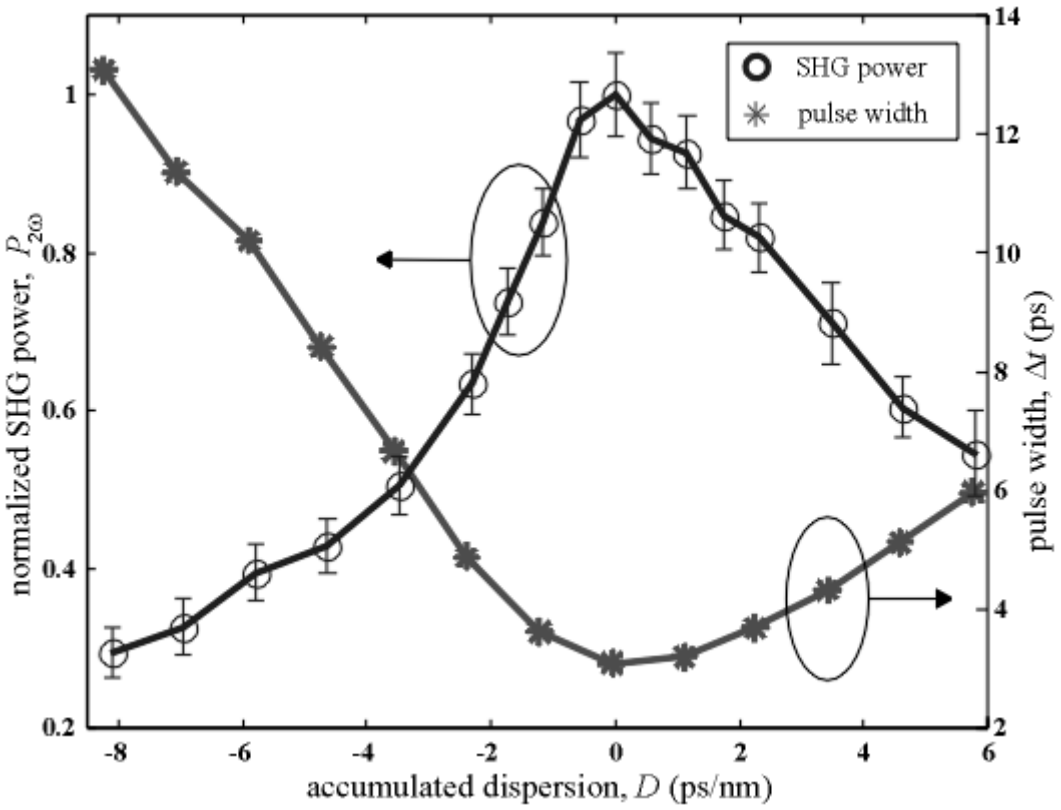

Fig. 3.9. Normalized SHG power $P_{2\omega}$ with error bars (± one standard deviation, left scale) and measured pulse width Δt (right scale) versus accumulated dispersion D.

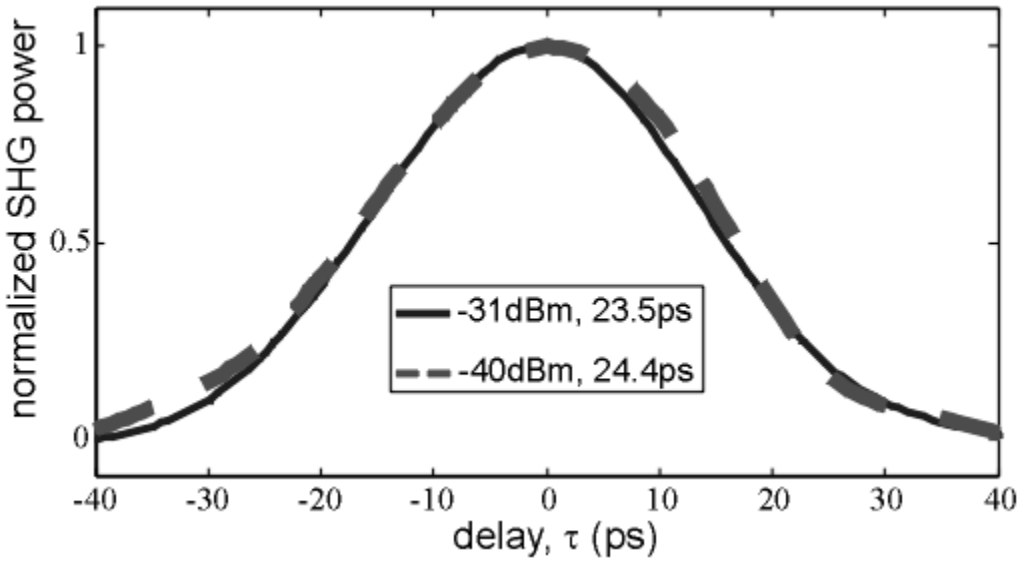

Fig. 3.10. Intensity autocorrelation traces of 10-GHz, 24-ps pulses at -31 dBm (solid) and -40 dBm (dashed) coupled power levels obtained by an unchirped QPM waveguide with PM BW Δf_{PM} ~63 GHz..

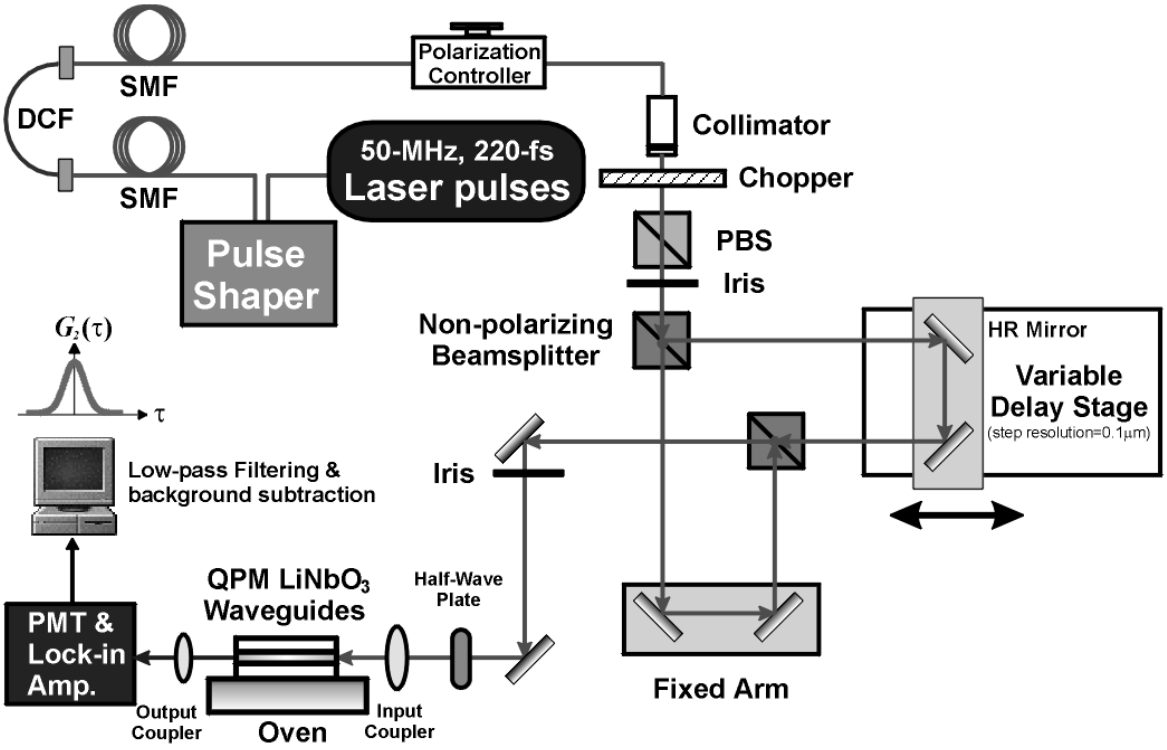

Fig. 3.11. Experimental setup for intensity autocorrelation measurements. SMF: single mode fiber, DCF: dispersion compensation fiber, PBS: polarization beamsplitter, HR: high reflection, PMT: photomultiplier tube.

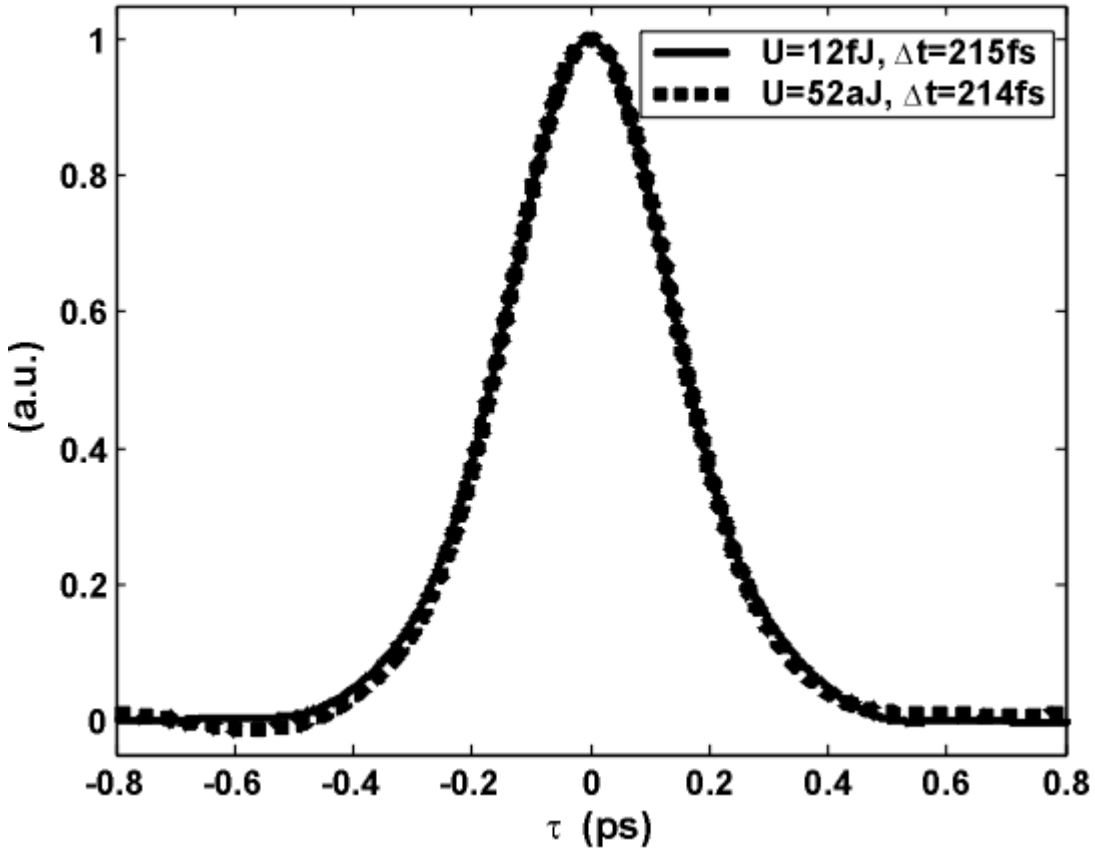

Fig. 3.12. Measured intensity autocorrelation functions $G_2(\tau)$ using a chirped QPM $LiNbO_3$ waveguide (PM tuning curve BW $\Delta\lambda_{PM}$ ~25 nm) at coupled input pulse energies of 12 fJ (solid) and 52 aJ (dotted), respectively.

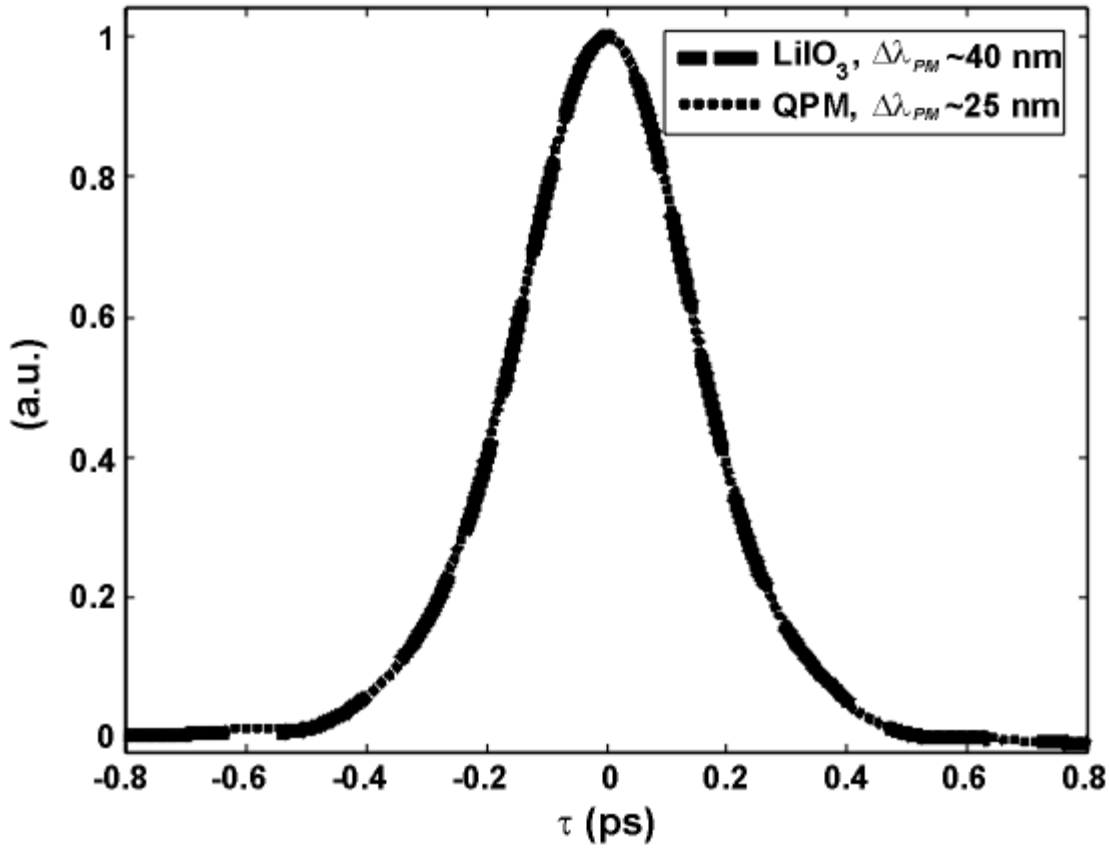

Fig. 3.13. Measured intensity autocorrelation functions $G_2(\tau)$ using a 1-mm-long bulk $LiIO_3$ ($\Delta\lambda_{PM}$ ~40 nm, dashed) and a chirped QPM $LiNbO_3$ waveguide ($\Delta\lambda_{PM}$ ~25 nm, dotted), respectively.

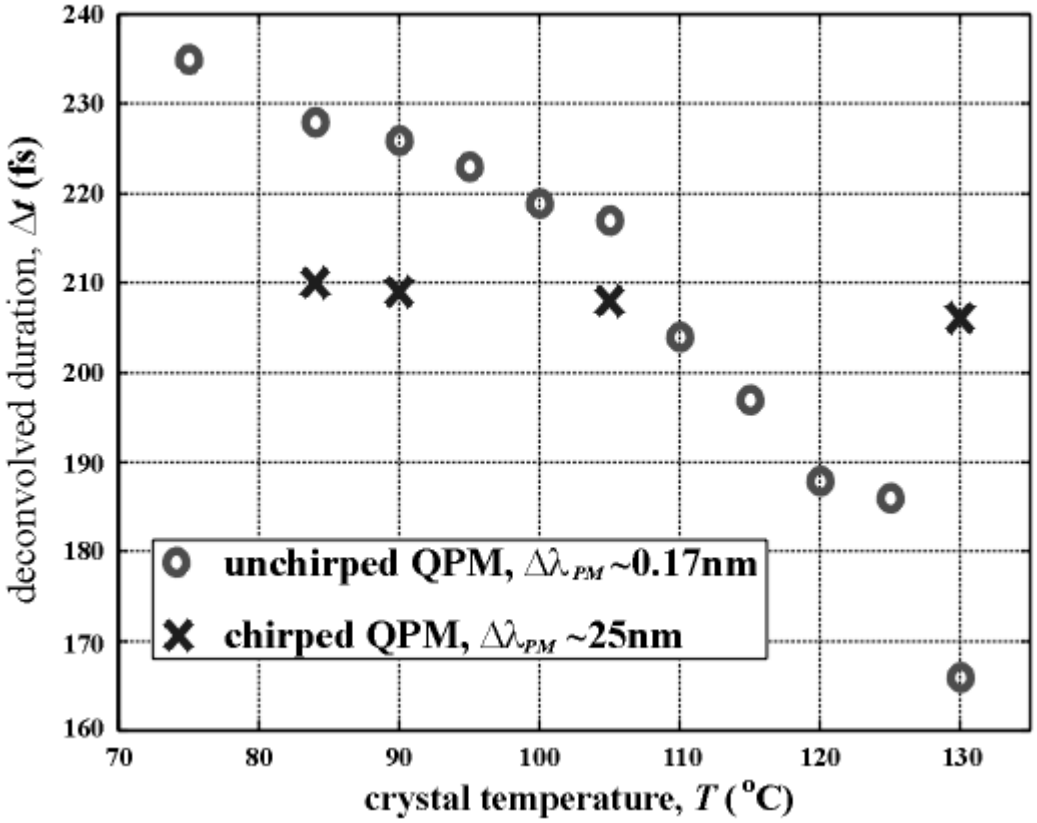

Fig. 3.14. Deconvolved pulse duration Δt as a function of crystal temperature T, for both unchirped (circle) and chirped (cross) QPM $LiNbO_3$ waveguides.

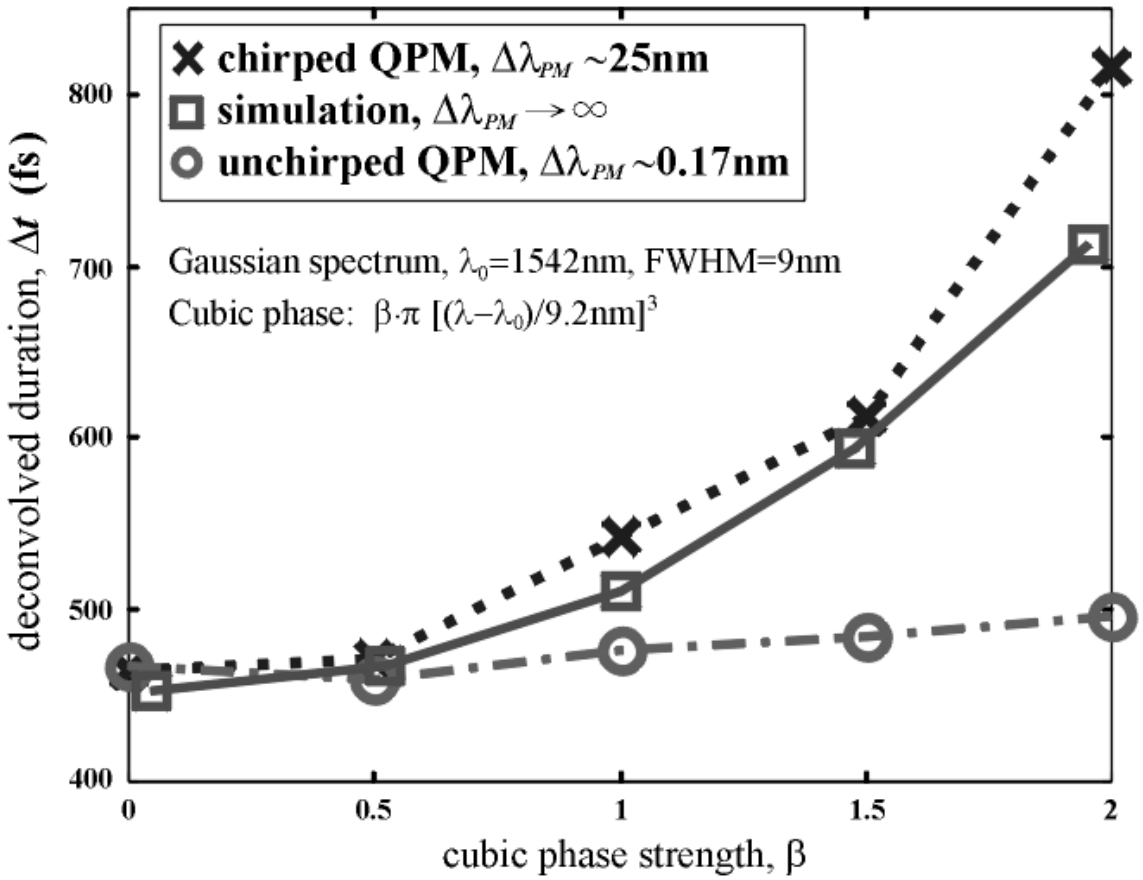

Fig. 3.15. Deconvolved pulse durations versus cubic phase strength of input pulse measured by unchirped (circle) and chirped (cross) QPM $LiNbO_3$ waveguides. Simulation result assuming infinite PM BW is also shown in the figure (square). The pulses have a common Gaussian power spectrum but different cubic phase strengths defined in eq. (3.17). Unchirped QPM guide is nearly insensitive to the pulse broadening arising from cubic phase modulation.

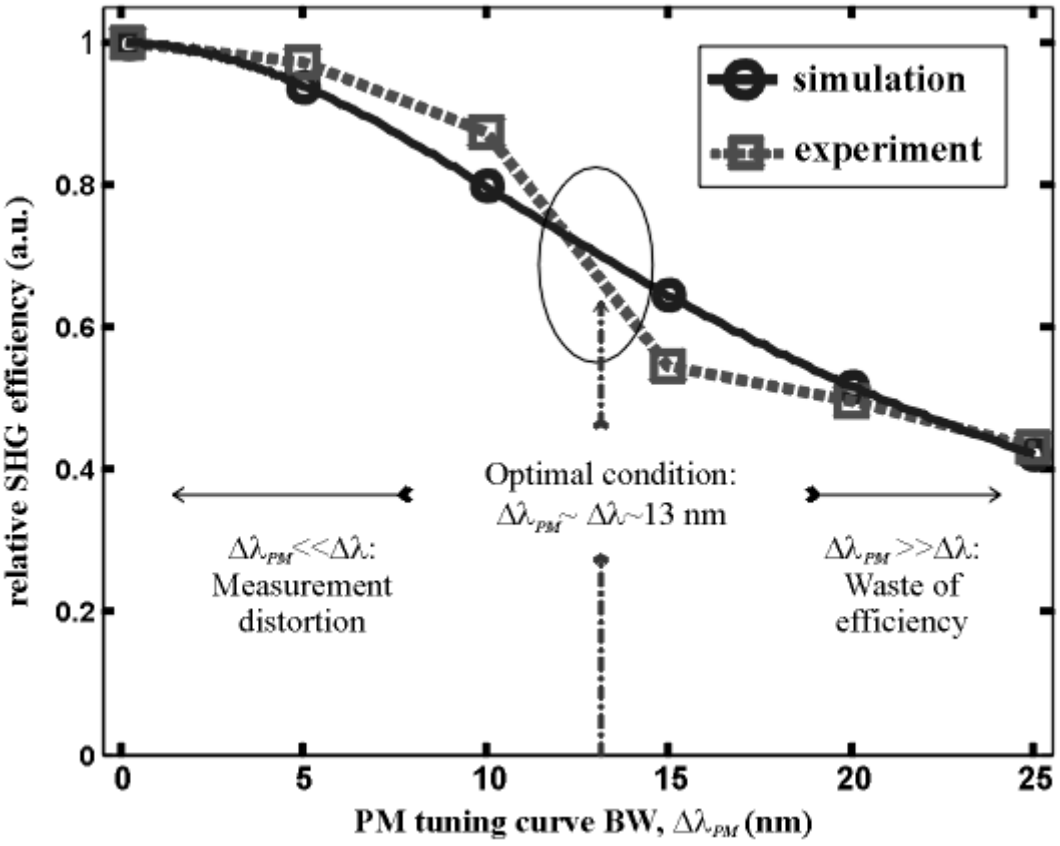

Fig. 3.16. Relative SHG efficiency versus PM tuning curve BW $\Delta\lambda_{PM}$ for unchirped ($\Delta\lambda_{PM}$ ~0.17 nm) and chirped ($\Delta\lambda_{PM}$ ~5, 10, 15, 20, 25 nm) QPM waveguides. $\Delta\lambda$ denotes the FWHM of the FH power spectrum. The simulation (circle) assumes a square-shaped $|H(\omega)|^2$ with different widths but constant spectral area: $\int |H(\omega)|^2 d\omega$. Optimal condition takes place at $\Delta\lambda_{PM}$ ~$\Delta\lambda$~13 nm, where accurate traces are obtainable and the SHG efficiency remains ~70 % of that of an unchirped QPM guide.

4. EXPERIMENTAL STUDIES OF FREQUENCY-RESOLVED OPTICAL GATING

We have discussed the conventional noncollinear SHG FROG in Sec. 2.4. This technique, along with a family of its varieties, has evolved as one of the standard tools to retrieve intensity and phase of ultrashort optical pulses. Greatly simplified configuration (GRENOUILLE) even becomes commercially available [58-59]. The corresponding sensitivity achieved by conventional bulk crystals, however, is limited by ~500 mW^2 [1]. Although the FWM FROG technique using 22-km-long DSF [18] has a sensitivity (0.2 mW^2) over three orders of magnitude better than that of conventional scheme, the performance is still insufficient to characterize weak signal pulses in some applications, such as signal monitoring in the intermediate or receiving end of a lightwave communication system. In this chapter, we will discuss the problems and our solutions in implementing the SHG FROG using the chirped QPM $LiNbO_3$ waveguides. Experimental results show that our scheme improves on the previous sensitivity record of FROG measurements by 75,000 times (2.7 μW^2) [23-24], which enables complete characterizations of optical pulses used in high-speed telecommunications with ~1-μW average power.

4.1 Collinear SHG FROG with Uneven PM Curve

We have shown that the chirped QPM waveguides permit large SHG efficiency and broad PM BW simultaneously. Nevertheless, their application in SHG FROG encounters two major technical problems: (i) interferometric fringes and signal background due to the collinear geometry adopted by the straight waveguides; (ii)

spectral distortion caused by the uneven PM curve of the chirped QPM waveguides. We will analyze these problems and propose solutions in the following text.

4.1.1 Collinear SHG FROG trace

A difficulty encountered by SHG FROG measurements using waveguide devices is the invalidity of noncollinear geometry, since crossing the input beams and selecting the output SH beam corresponding to the field product term ($a(t)\cdot a(t-\tau)$ in eq. (4.1)) in the waveguides require excessive efforts [60]. Although collinear type II phase matching was demonstrated to achieve signal gating in bulk crystals [61], this is inapplicable in the proton-exchanged $LiNbO_3$ waveguides where only TM modes are guided. The additional GVM between two fundamental pulses with different polarizations further restrict the nonlinear interaction length and SHG efficiency. As a result, our chirped QPM $LiNbO_3$ waveguide scheme still applies for the collinear geometry.

In collinear geometry (Fig. 4.1a), the nonlinear polarization results from the square of the summation of the two split fields, instead of their product:

$$\begin{aligned} P_{NL}(\omega,\tau) &= F_t\left\{\left[a(t)+a(t-\tau)e^{-j\omega_0\tau}\right]^2\right\} \\ &= F_t\left\{a^2(t)+a^2(t-\tau)\cdot e^{-j2\omega_0\tau}+2a(t)\cdot a(t-\tau)\cdot e^{-j\omega_0\tau}\right\} \\ &= P_{NL}^X(\omega,0)\cdot\left(1+e^{-j(\omega+2\omega_0)\tau}\right)+2P_{NL}^X(\omega,\tau)\cdot e^{-j\omega_0\tau} \end{aligned} \tag{4.1}$$

where $a(t)$ is the complex field envelope of the input pulse, τ indicates the relative delay introduced by the Michelson interferometer, ω_0 is the carrier angular frequency, and $P_{NL}^X(\omega,\tau)\propto F_t\{a(t)\cdot a(t-\tau)\}$ is the nonlinear polarization arising from the self-gated field (see eq. (2.81)). Assuming the PM power spectrum $|H(\omega)|^2$ is broad and uniform within the band where $P_{NL}^X(\omega,\tau)$ is not negligible, the measured interferometric FROG trace $I_{IFROG}(\omega,\tau)$ would be:

$$I_{IFROG}(\omega,\tau)=\left|P_{NL}(\omega,\tau)\right|^2\propto I_{FROG}(\omega,0)+2I_{FROG}(\omega,\tau) \tag{4.2}$$

$$+4\cdot\sqrt{I_{FROG}(\omega,0)\cdot I_{FROG}(\omega,\tau)}\cdot cos\left(\Delta\psi+\frac{\omega\tau}{2}\right)\cdot cos\left[\left(\frac{\omega}{2}+\omega_0\right)\tau\right]$$

$$+I_{FROG}(\omega,0)\cdot cos[(\omega+2\omega_0)\tau]$$

where

$$\Delta\psi\equiv\psi_{NL}^{X}(\omega,\tau)-\psi_{NL}^{X}(\omega,0),\ \ \psi_{NL}^{X}(\omega,\tau)\equiv\angle P_{NL}^{X}(\omega,\tau) \tag{4.3}$$

and $I_{FROG}(\omega,\tau)\equiv\left|P_{NL}^{X}(\omega,\tau)\right|^2$ is the standard noncollinear FROG trace defined in eq. (2.84). The terms in eq. (4.2) can be separated by taking 1-D Fourier transform with respect to τ $\left(\int I_{IFROG}(\omega,\tau)\cdot e^{-jk\tau}d\tau\right)$, from which five spectral strips are centered at k = 0, $\pm\omega_0$, $\pm2\omega_0$, respectively. Since the carrier frequency ω_0 is normally much higher than the pulse BW, the last two terms in eq. (4.2) contribute to fast oscillating fringes along the delay axis. Besides, the first term $I_{FROG}(\omega,0)$ represents a τ-independent signal background arising from two well-separated pulses. Fig. 4.1b-c illustrate a simulated interferometric FROG trace $I_{IFROG}(\omega,\tau)$, where the standard FROG trace $I_{FROG}(\omega,\tau)$ is "buried" by the fringes and background.

In principle, low-pass filtering (LPF) the interferometric trace $I_{IFROG}(\omega,\tau)$ can remove the fringes:

$$\bar{I}_{FROG}(\omega,\tau)\equiv LPF\{\,I_{IFROG}(\omega,\tau)\,\}\propto I_{FROG}(\omega,0)+2I_{FROG}(\omega,\tau) \tag{4.4}$$

Since the standard FROG trace vanishes when the delay τ is much greater than the pulse width Δt, i.e. $I_{FROG}(\omega,\tau>>\Delta t)\rightarrow 0$; the signal background $I_{FROG}(\omega,0)$ can be derived by a spectral slice of $\bar{I}_{FROG}(\omega,\tau)$ taken at large delay:

$$I_{FROG}(\omega,0)\approx\bar{I}_{FROG}(\omega,\tau>>\Delta t) \tag{4.5}$$

from which the standard FROG trace $I_{FROG}(\omega,\tau)$ can be recovered from $\bar{I}_{FROG}(\omega,\tau)$:

$$I_{FROG}(\omega,\tau)\propto\bar{I}_{FROG}(\omega,\tau)-\bar{I}_{FROG}(\omega,\tau>>\Delta t) \tag{4.6}$$

If the power ratio r of the two split pulses used in collinear SHG FROG measurements is unbalanced: $P_{NL}(\omega,\tau)=F_t\left\{\left[\sqrt{r}\cdot a(t)+a(t-\tau)e^{-j\omega_0\tau}\right]^2\right\}$, the above formulations are still valid except that the signal-to-background ratio is reduced:

$$I_{IFROG}(\omega,\tau) \propto \left(1+r^2\right)\cdot I_{FROG}(\omega,0) + 4r\cdot I_{FROG}(\omega,\tau) \tag{4.7}$$

$$+4\sqrt{r}\cdot\sqrt{I_{FROG}(\omega,0)\cdot I_{FROG}(\omega,\tau)}\left\{r\cdot cos\left(\omega_0\tau-\Delta\psi\right)+cos\left[\left(\omega+\omega_0\right)\tau+\Delta\psi\right]\right\}$$

$$+2r\cdot cos[(\omega+2\omega_0)\tau]\cdot I_{FROG}(\omega,0)$$

$$\bar{I}_{FROG}(\omega,\tau) \propto I_{FROG}(\omega,0)+\left(\frac{4r}{1+r^2}\right)I_{FROG}(\omega,\tau) \tag{4.8}$$

$$I_{FROG}(\omega,\tau) \propto \bar{I}_{FROG}(\omega,\tau)-\bar{I}_{FROG}(\omega,\tau>>\Delta t)\text{, even for } r\neq 1 \tag{4.9}$$

As a result, the same LPF and background subtraction procedures can be employed to get the standard FROG trace $I_{FROG}(\omega,\tau)$ without balancing the split powers. Fig. 4.2 illustrates the evolution of FROG trace processing discussed above (assuming r=1).

We should point out that interferometric terms in eq. (4.2) still contain useful pulse information. For example, MEFISTO technique uses the spectral strips centered at $k=\omega_0$ for non-iterative pulse reconstruction [62], while modified FROG algorithm can completely retrieve 9-fs pulses from fundamental-modulation (FM) FROG trace obtained by extracting spectral components around $k=\pm\omega_0$ from $I_{IFROG}(\omega,\tau)$ [63]. Here we focus on sensitivity issue, and try to get a standard SHG FROG trace for conventional pulse reconstruction.

4.1.2 Spectral distortion and frequency marginal correction

So far we have assumed that PM power spectrum $|H(\omega)|^2$ is broad and uniform within the band of interest, and plays no role in shaping the SHG power spectrum (eq. (2.39)). In reality, $|H(\omega)|^2$ of our chirped QPM waveguides is very uneven (see Fig. 3.6) and can distort the interferometric FROG trace through a spectral multiplication [64-65]:

$$\tilde{I}_{IFROG}(\omega,\tau)=I_{IFROG}(\omega,\tau)\times\left|H(\omega)\right|^2 \tag{4.10}$$

The LPF and background subtraction procedures discussed in Sec. 4.1.1 remain applicable in the presence of uneven $|H(\omega)|^2$:

$$\tilde{\bar{I}}_{FROG}(\omega,\tau)\equiv LPF\left\{\tilde{I}_{IFROG}(\omega,\tau)\right\}\propto\bar{I}_{FROG}(\omega,\tau)\times\left|H(\omega)\right|^2 \tag{4.11}$$

$$\propto \left(I_{FROG}(\omega,0)\times\left|H(\omega)\right|^2\right)+2\left(I_{FROG}(\omega,\tau)\times\left|H(\omega)\right|^2\right)$$

$$\equiv \widetilde{I}_{FROG}(\omega,0)+2\,\widetilde{I}_{FROG}(\omega,\tau) \tag{4.12}$$

$$\widetilde{I}_{FROG}(\omega,\tau)\propto \widetilde{\widetilde{I}}_{FROG}(\omega,\tau)-\widetilde{\widetilde{I}}_{FROG}(\omega,\tau>>\Delta t) \tag{4.13}$$

where $\widetilde{I}_{FROG}(\omega,0)$ and $\widetilde{I}_{FROG}(\omega,\tau)$ are the distorted signal background and FROG trace, respectively. Fig. 4.3 illustrates a simulated example where the three pseudo peaks in the distorted FROG trace $\widetilde{I}_{FROG}(\omega,\tau)$ actually result from the uneven PM curve, instead of the real signal. Pulse reconstruction would be incorrect if the spectral distortion is not eliminated before using the retrieval algorithm.

Fortunately, the SHG FROG can apply frequency marginal correction method [12, 35] to compensate the spectral distortion (as long as there is no dark response within the band of interest) with nominal experimental effort. Mathematically, the frequency marginal function $M(\omega)$ is defined as the delay integral of the FROG trace $I_{FROG}(\omega,\tau)$, which is equivalent to the autoconvolution of fundamental power spectrum $I_\omega(\omega) \equiv |A_\omega(\omega)|^2$:

$$M(\omega)\equiv\int_{-\infty}^{\infty} I_{FROG}(\omega,\tau)d\tau \tag{4.14}$$

$$=\int_{-\infty}^{\infty}\left|F_t\left\{a(t)a(t-\tau)\right\}\right|^2 d\tau=\int_{-\infty}^{\infty}\left|A_\omega(\omega)\otimes A_\omega(\omega)e^{-j\omega\tau}\right|^2 d\tau$$

$$=\int_{-\infty}^{\infty}\int_{-\infty}^{\infty}\int_{-\infty}^{\infty}A_\omega(\omega-\omega')A_\omega(\omega')A_\omega^*(\omega-\omega'')A_\omega^*(\omega'')e^{-j(\omega'-\omega'')\tau}d\omega'd\omega''d\tau$$

$$=\int_{-\infty}^{\infty}A_\omega(\omega-\omega')A_\omega(\omega')A_\omega^*(\omega-\omega')A_\omega^*(\omega')d\omega'=\int_{-\infty}^{\infty}\left|A_\omega(\omega-\omega')\right|^2\left|A_\omega(\omega')\right|^2 d\omega'$$

$$=I_\omega(\omega)\otimes I_\omega(\omega) \tag{4.15}$$

where the identity $\int_{-\infty}^{\infty}e^{-j(\omega'-\omega'')\tau}d\tau=\delta(\omega'-\omega'')$ is used. If some τ-independent power spectral modulation $|H(\omega)|^2$ imposes on the standard FROG trace $I_{FROG}(\omega,\tau)$, the frequency marginal function would be distorted as:

$$\widetilde{M}(\omega)\equiv\int_{-\infty}^{\infty}\widetilde{I}_{FROG}(\omega,\tau)d\tau=\int_{-\infty}^{\infty}\left[I_{FROG}(\omega,\tau)\cdot\left|H(\omega)\right|^2\right]d\tau=M(\omega)\cdot\left|H(\omega)\right|^2 \tag{4.16}$$

Note that the evaluation of $\widetilde{M}(\omega)$ is vulnerable to the residual background $\varepsilon(\omega)$ in $\widetilde{I}_{FROG}(\omega,\tau)$:

$$\widetilde{M}(\omega,\varepsilon)=\int_{-\infty}^{\infty}\left[\widetilde{I}_{FROG}(\omega,\tau)+\varepsilon(\omega)\right]d\tau=\widetilde{M}(\omega)+\varepsilon(\omega)\cdot\left(\int_{-\infty}^{\infty}d\tau\right) \tag{4.17}$$

where $\varepsilon(\omega)$ resulting from incomplete background subtraction in eq. (4.13) is amplified. Therefore, one has to carefully remove background before evaluating frequency marginal. In real experiments, we can directly measure $\widetilde{I}_{FROG}(\omega,\tau)$ and $I_{\omega}(\omega)$ (by an optical spectrum analyzer), then performing τ-integration and autoconvolution in software to get $\widetilde{M}(\omega)$ and $M(\omega)$, respectively. Spectral distortion $|H(\omega)|^2$ can thus be retrieved by eq. (4.16), and the distortion-free FROG trace is recovered by:

$$I_{FROG}(\omega,\tau)=\frac{\widetilde{I}_{FROG}(\omega,\tau)}{|H(\omega)|^2}=\widetilde{I}_{FROG}(\omega,\tau)\times\frac{I_{\omega}(\omega)\otimes I_{\omega}(\omega)}{\int_{-\infty}^{\infty}\widetilde{I}_{FROG}(\omega,\tau)d\tau} \tag{4.18}$$

Fig. 4.4 illustrates the flow chart and related traces/curves of the frequency marginal correction method.

The frequency marginal correction method formulated by eq. (4.18) only requires fundamental power spectral measurement (in addition to the FROG trace), which is very fast and easy to operate. Besides, $|H(\omega)|^2$ can characterize all types of spectral response (assuming the fundamental power spectrum can be measured accurately), such as the uneven quantum efficiency spectrum of the CCD detectors used in acquiring FROG traces. This is especially important when pulses as short as a few femtoseconds are involved, where most optical components in the setup present uneven spectral response within the extremely broad (hundreds of nanometers) bandwidth [64-65].

4.2 SHG FROG Experiments Using Chirped QPM $LiNbO_3$ Waveguides

Fig. 4.5 shows a schematic diagram of our SHG FROG experiments. We use a passively mode-locked fiber laser plus a band-pass filter to produce laser pulses with ~280-fs duration, 50-MHz repetition rate, 1538-nm central wavelength, and 11-nm

spectral width. The pulse train is sent into a modified collinear-type free-space Michelson interferometer (MI) to produce a pulse pair with variable delay τ. To remove the interferometric fringes by hardware, we use a piezoelectric transducer (PZT) driven by ~70-Vpp, ~180-Hz sinusoidal voltage to dither the fixed arm of the MI for a small displacement *dl* (see the subfigure in Fig. 4.5). In this way, the SH power spectrum taken at delay τ is actually the average of many spectra with slightly different delays $\tau + d\tau$ centered at τ, where $d\tau = 2dl/c$ (c is the speed of light in air). The delay dithering scheme is equivalent to low-pass filtering the interferometric trace in software, while prevents from recording and processing a huge amount of data needed to resolve the dense carrier fringes [66]. In our experiments, the dithering displacement is about one wavelength $dl \approx \lambda_o \approx 1.5$ μm, which is sufficient to average two carrier cycles and effectively remove the oscillating fringes along the delay axis (no additional low-pass filtering in software is required). Larger displacement *dl* gives better average at the cost of reduced temporal resolution, lower dithering frequency, and larger PZT driving voltage. Fringe removal does not function well if the delay dithering is performed in the variable arm, where the translation stage motion is coupled with the PZT dithering, and result in unexpected data noises.

The pulses from the modified MI are coupled into a chirped QPM $LiNbO_3$ waveguide with ~25-nm PM tuning curve BW $\Delta\lambda_{PM}$ (PM BW Δf_{PM} ~6.25 THz in SH band) to produce SHG signal. A spectrometer (Jobin Yvon TRIAX550, with a 1200-grooves/mm diffraction grating) and intensified CCD camera (Princeton Instruments PI·MAX:512 Gen III) are employed to record the SHG power spectrum for each delay τ, which yields the raw FROG trace (with background, see eq. (4.11)) $\tilde{\tilde{I}}_{FROG}(\omega,\tau)$. To even improve the fringe averaging, we continuously scan the translation stage of the variable arm without intermediate stopping, and grab one power spectrum for every 1 sec (camera exposure time is 800 ms per shot, the remaining 200 ms is mainly for data read-out). Therefore, each recorded spectrum is obtained by averaging the spectra corresponding to 80% delay increment $\Delta\tau$, which can further suppress the fringes. Note that $\Delta\tau$ is determined by the speed of the scanning stage v_{scan}. We normally set v_{scan}= 3 μm/s, such

that $\Delta\tau$ = 20 fs. Acquiring a raw FROG trace consisting of 128 spectra takes about 2 minutes.

The raw FROG trace $\tilde{\tilde{I}}_{FROG}(\omega,\tau)$ is processed in software to (i) subtract the signal background according to eq. (4.13), (ii) perform frequency marginal correction (eq. (4.17)) with the aid of fundamental power spectrum $I_\omega(\omega)$ measured by an OSA, (iii) retrieve the intensity and phase of the pulse in time and frequency domains by a commercial software (Femtosoft FROG 3). The pulse retrieval normally takes less than 1 minute to converge.

Fig. 4.6 illustrates measured (after background subtraction and frequency marginal correction) and retrieved FROG traces $I_{FROG}(\omega,\tau)$ (grid size 64×64) using the nearly BW-limited pulses with coupled pulse energies U of 9.5 fJ (a-b) and **124 aJ** (c-d), respectively. The latter is equivalent to **~970 photons per pulse**, 0.44-mW peak power, and 6.2-nW average power, corresponding to an unprecedented FROG sensitivity of **2.7 μW²**. Even with a 19-dB input power difference (38-dB difference for SHG powers), these FROG traces agree well with one another. The FROG errors G (defined in eq. (2.88)) are 0.0022 and 0.0032, respectively. Note that the error G scales as $1/\sqrt{N}$ for an $N\times N$ trace, and typical G values resulting from accurate retrieval of low-noise data with N=64 are ~0.007 [12]. The FROG error from our record-sensitive measurement remains well below the average, which proves the good integrity of experimental data and retrieval convergence.

Fig. 4.7 shows the retrieved pulses in (a) frequency-, and (b) time- domains at the two input power levels. An independently measured input power spectrum is plotted as a dotted curve in Fig. 4.7a for comparison. The retrieved spectral intensities closely approach this curve, except for the oscillatory fine structure, which arises due to interference between the main pulse and an attenuated satellite caused by reflections at the band-pass filer. Better spectral resolution and larger delay scanning range would be required to resolve these features in the measurement. The spectral phases are fitted with cubic polynomials, and the resulting quadratic phase coefficients are 2.60×10^{-3} ps^2, and 2.71×10^{-3} ps^2. The retrieved temporal profiles also overlap well with each other, where

the intensity FWHM values are essentially identical: 279 fs and 278 fs, respectively (time-reversal ambiguity exists as usual in SHG FROG).

To further verify the measurement capability, we inserted a section of 5-meter-long single mode fiber (SMF) into the link to increase the quadratic spectral phase, and performed the FROG measurement. The retrieved spectral intensity and phase profiles with coupled energy of 300-aJ per pulse are shown in Fig. 4.8. The spectral phase is predominately parabolic, where the anomalous dispersion of SMF uniquely determines the sign of the retrieved spectral phase. Fitting the spectral phase profile shows that the quadratic phase coefficient is increased to -4.36×10^{-2} ps^2. Disregarding the small chirp measured in Fig. 4 (whose sign is ambiguous), the 5-m-long SMF is estimated to introduce an accumulated dispersion of –70 fs/nm, close to the value predicted by the SMF specification (–83 fs/nm) around the 1538-nm band (actual dispersion could vary from fiber to fiber). The retrieved temporal FWHM is broadened to ~800 fs, also in good agreement with that predicted by the measured spectral width and dispersion.

In conclusion, we overcome the problems of interferometric fringes and uneven PM response by delay dithering and frequency marginal correction method to realize SHG FROG measurements using the chirped QPM $LiNbO_3$ waveguides. Our scheme achieves an unprecedented sensitivity of **2.7 μW^2**, improving on the previous record by **75,000 times**.

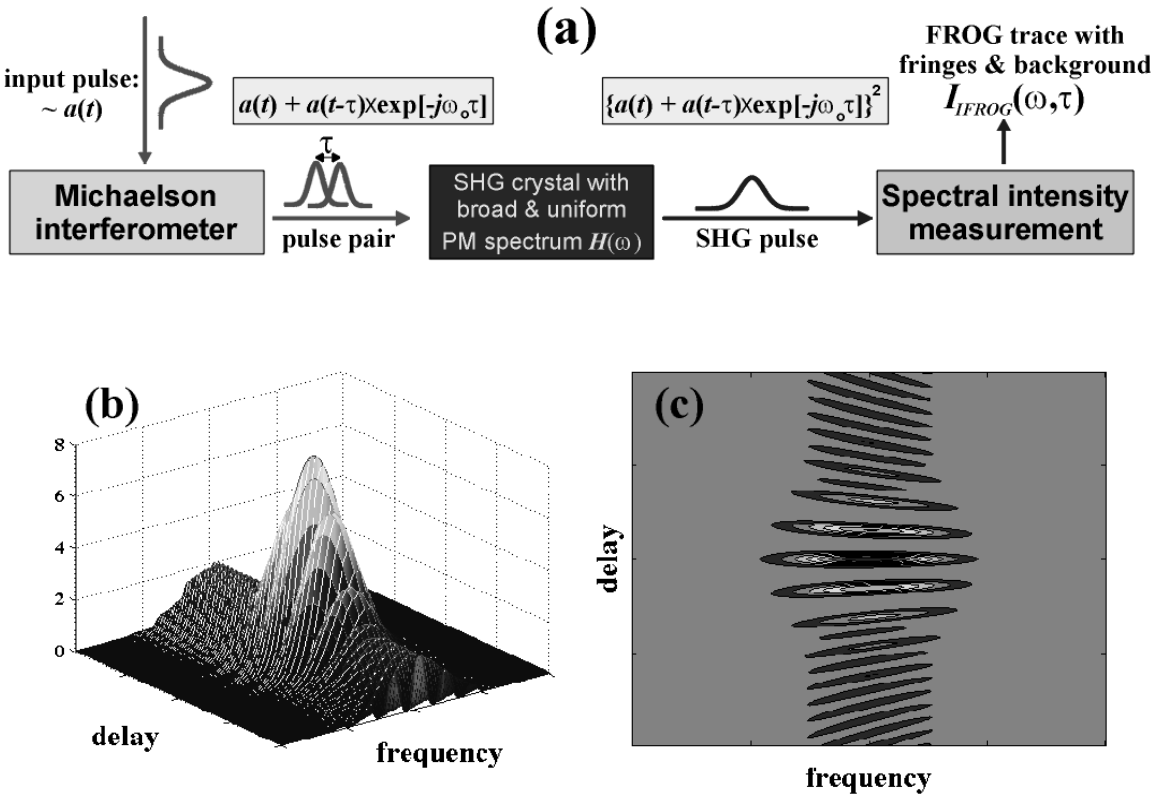

Fig. 4.1. (a) Schematic diagram of collinear SHG FROG measurements. A simulated interferometric FROG trace $I_{IFROG}(\omega,\tau)$ is shown in (b) mesh, and (c) contour plots, where the standard FROG trace is "buried" by the fast oscillating fringes along the delay axis and the delay-independent signal background.

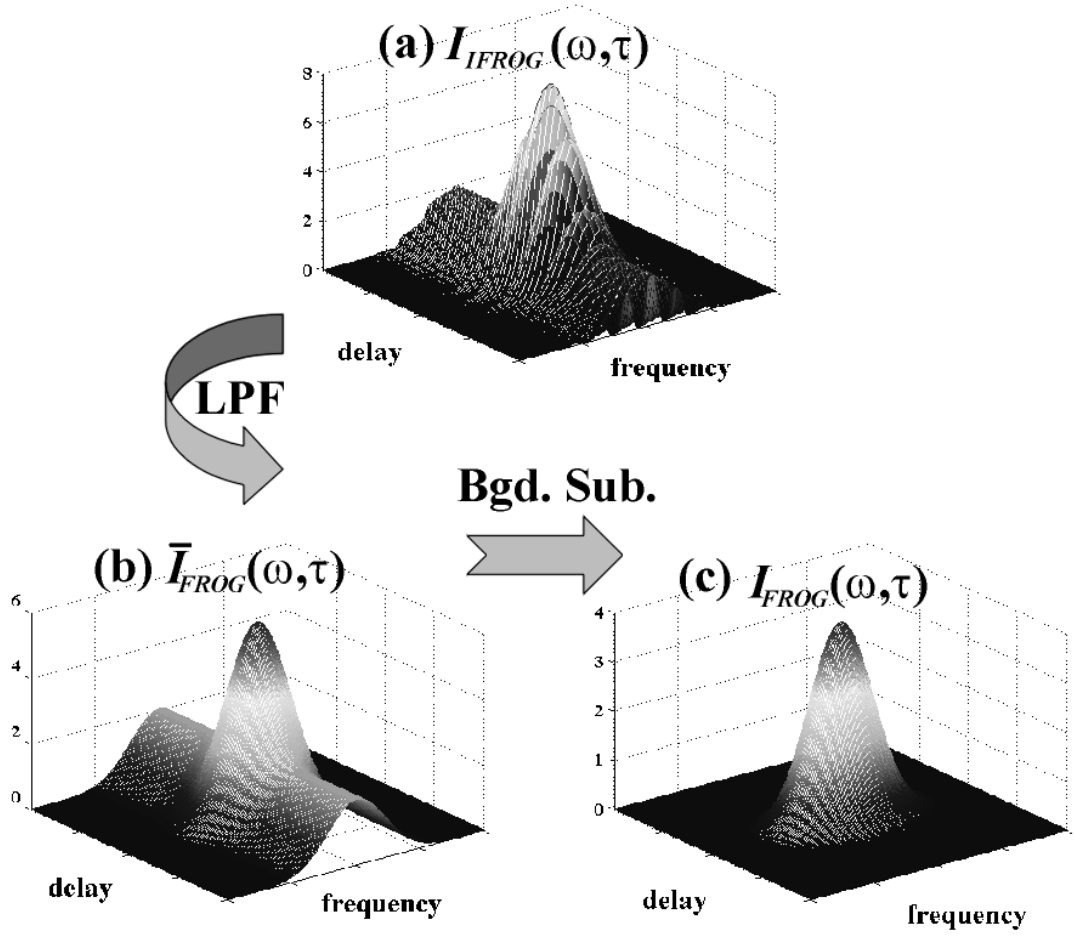

Fig. 4.2. Evolution of FROG trace post-processing: (a) original interferometric FROG trace, (b) after low-pass filtering (LPF), (c) after background subtraction (Bgd. Sub.). $I_{FROG}(\omega,\tau)$ is the standard noncollinear SHG FROG trace.

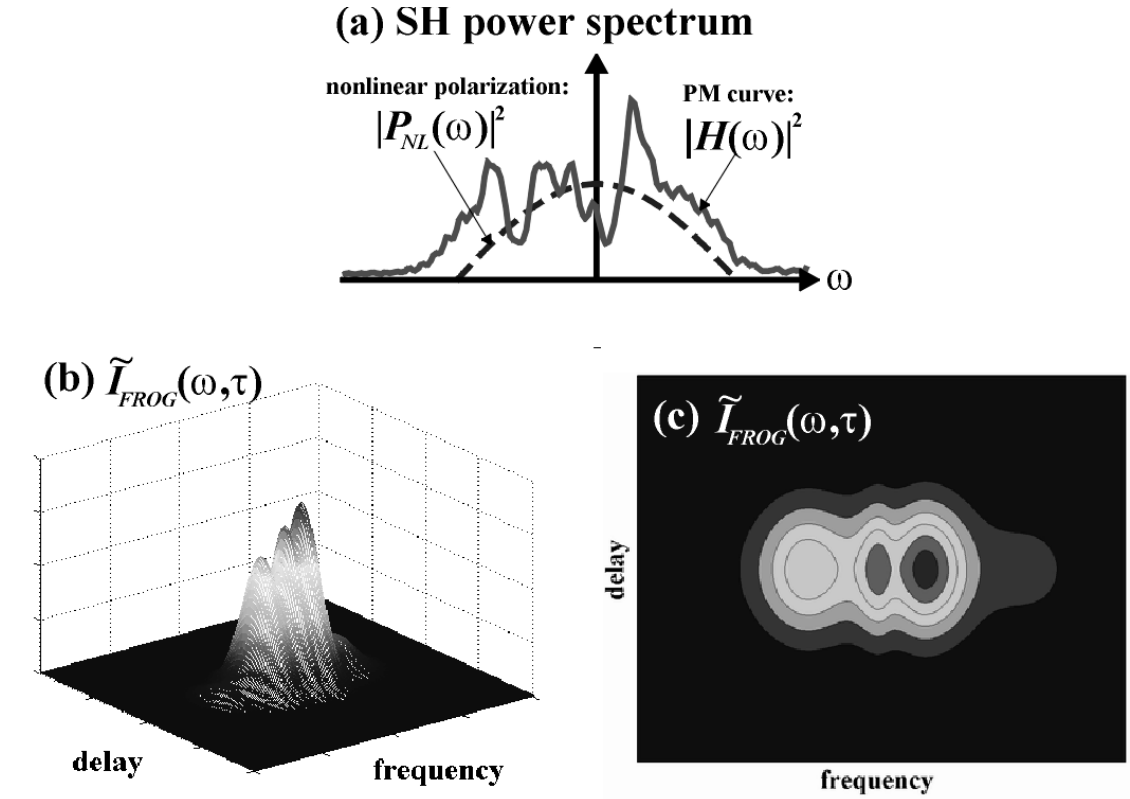

Fig. 4.3. Simulated example of spectral distortion due to an uneven PM curve: (a) second-harmonic power spectrum of a single input pulse: $|A_{2\omega}(\omega)|^2 \propto |P_{NL}(\omega)|^2 \times |H(\omega)|^2$, where the fluctuation of PM curve $|H(\omega)|^2$ can deviate $|A_{2\omega}(\omega)|^2$ from the nonlinear polarization $|P_{NL}(\omega)|^2 \equiv A_{\omega}(\omega) \otimes A_{\omega}(\omega)$; (b) mesh, and (c) contour plots of the FROG trace $\tilde{I}_{FROG}(\omega,\tau)$ spectrally distorted by the uneven PM curve $|H(\omega)|^2$, where the three pseudo peaks come from $|H(\omega)|^2$.

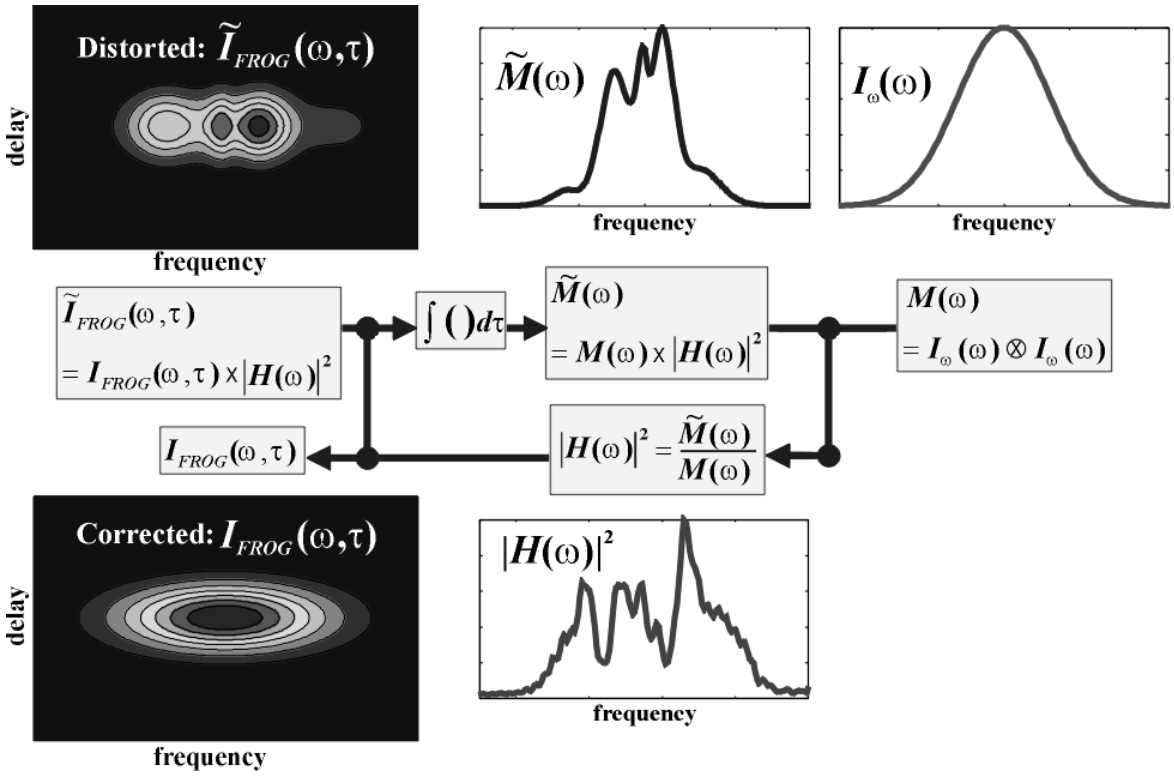

Fig. 4.4. Flow chart of frequency marginal correction method.

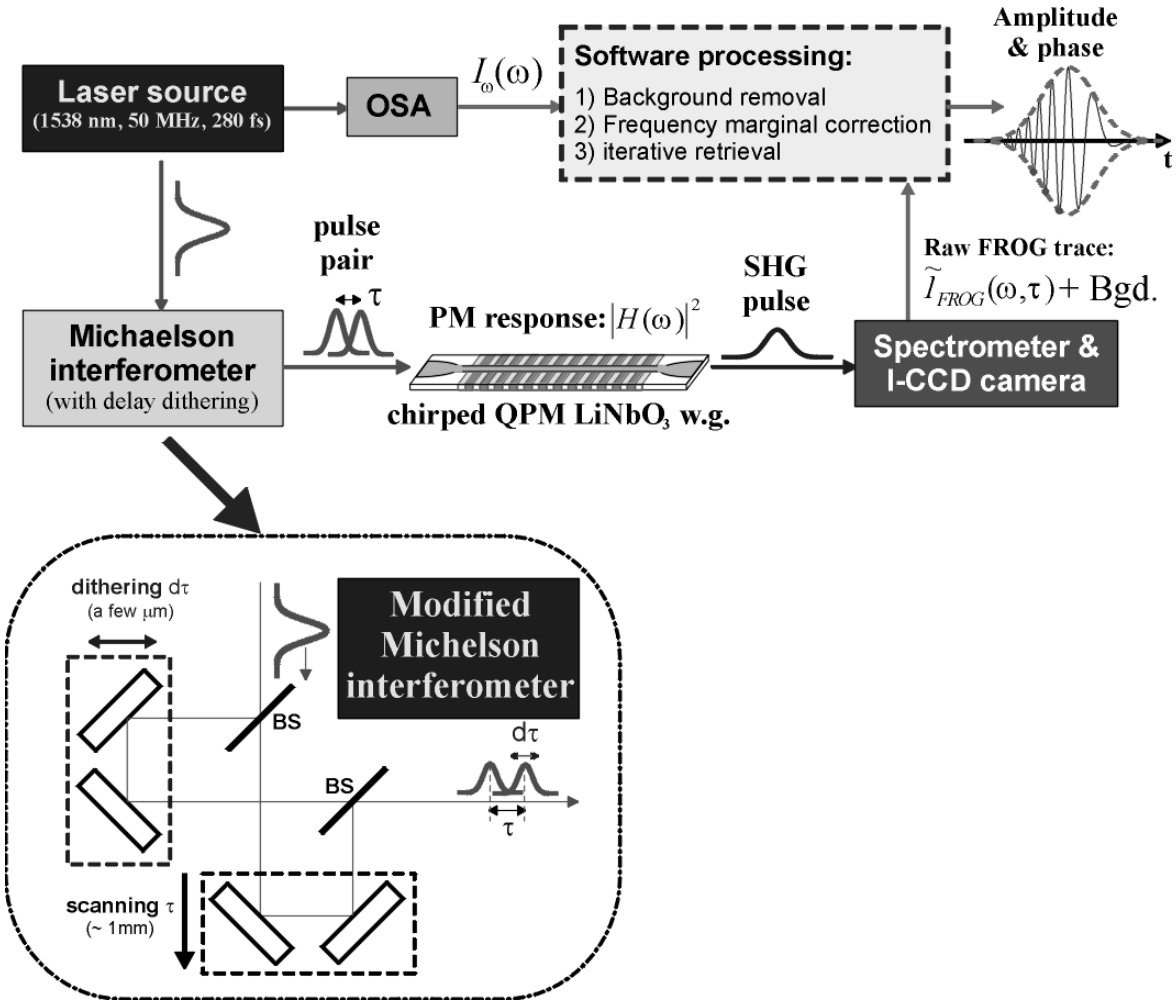

Fig. 4.5. Schematic diagram of our SHG FROG experiments. OSA: optical spectrum analyzer, I-CCD: intensified charge-coupled device.

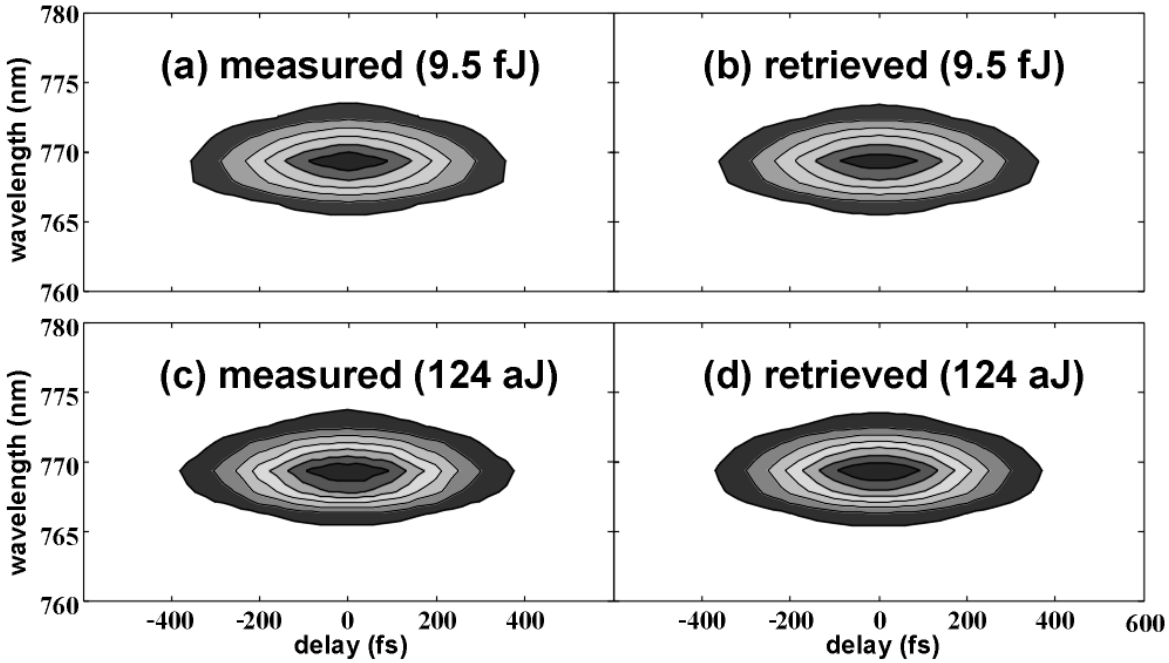

Fig. 4.6. FROG traces of (a) measured, (b) retrieved, at U=9.5 fJ; and (c) measured, (d) retrieved, at U=124 aJ, where U is the coupled energy per input pulse.

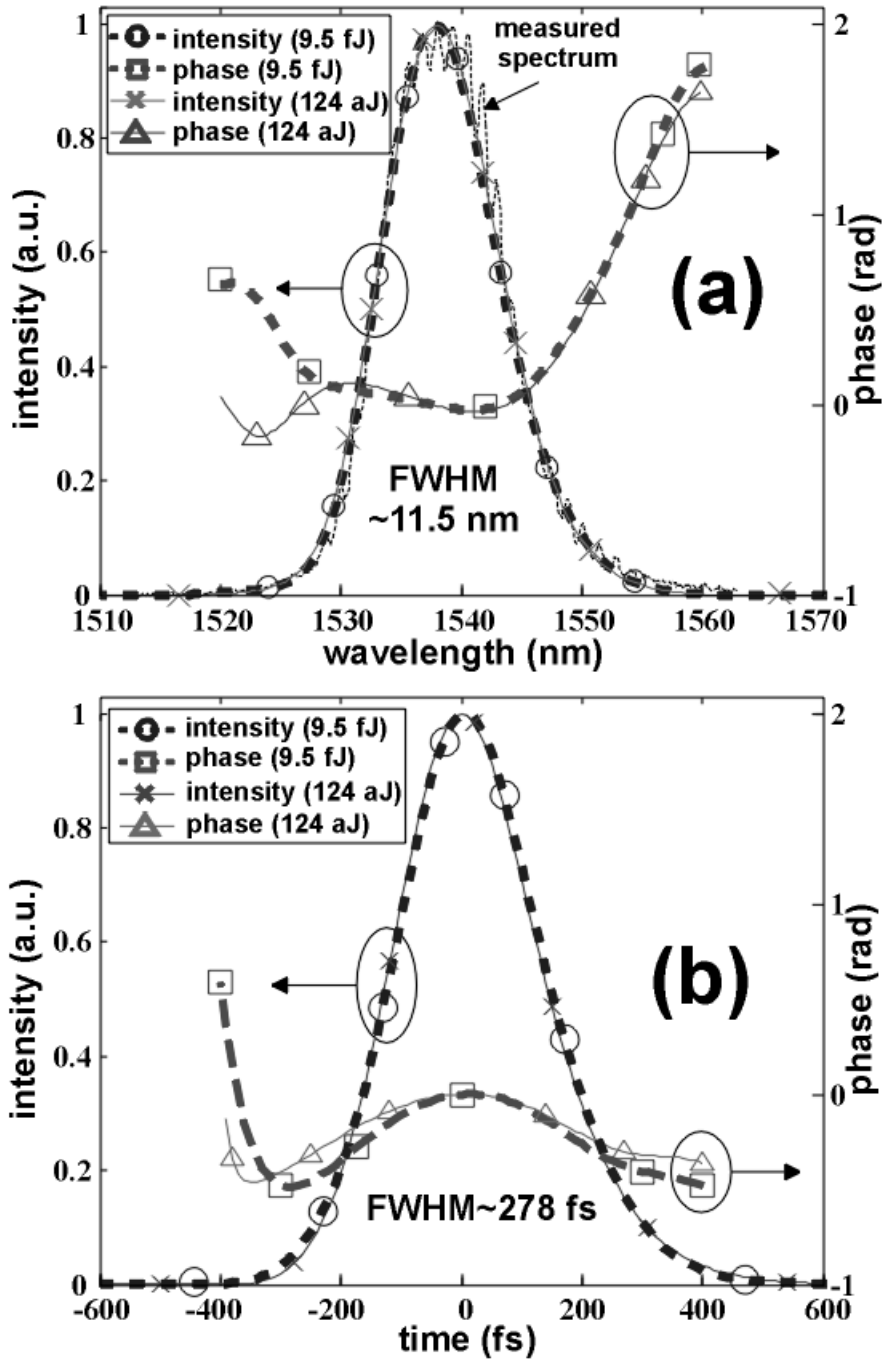

Fig. 4.7. Retrieved pulse depicted in: (a) frequency domain, and (b) time domain for both 9.5-fJ and 124-aJ coupled pulse energies. Dotted curve in (a) represents the independently measured power spectrum from an optical spectrum analyzer.

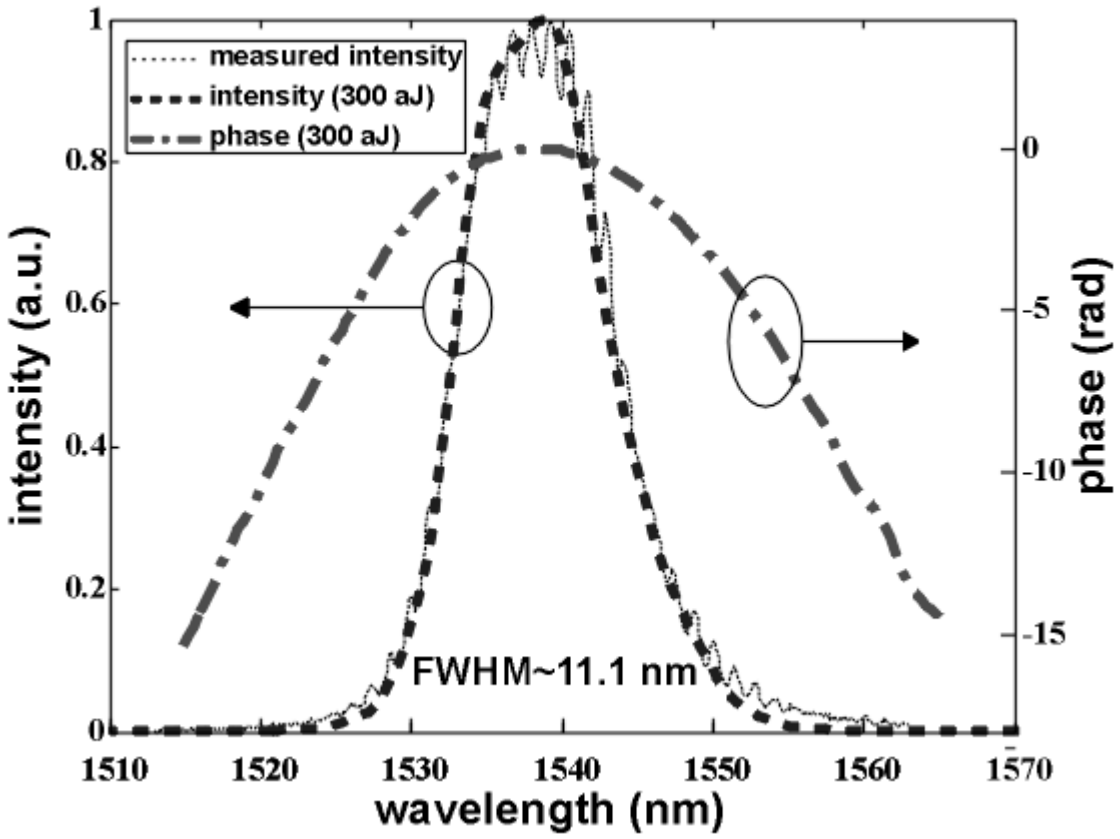

Fig. 4.8. Retrieved spectral intensity and phase of the pulse dispersed by a 5-m-long SMF measured at 300-aJ coupled pulse energy. The pulse dispersion is estimated as -70 fs/nm.

5. CONCLUSION AND PERSPECTIVE

We have experimentally demonstrated chromatic dispersion monitoring, intensity autocorrelation, and SHG FROG with unprecedented low-power requirements by using chirped QPM $LiNbO_3$ waveguides. The achieved measurement sensitivities of the latter two experiments are **0.32 μW²** and **2.7 μW²**, improving on the previous records by **500** and **75,000** times, respectively. The minimum measurable pulse duration Δt_{min} is limited by the GVD-induced input pulse broadening, while the PM BW can be extended by chirping the QPM periods even more strongly. For congruent $LiNbO_3$ at room temperature, Sellmeier equation of extraordinary refractive index $n_e(\lambda)$ [67] predicts that GVD is ~0.1 fs/THz/mm at 1.55-μm central wavelength. As a result, our ~6-cm-long $LiNbO_3$ waveguides correspond to an accumulated dispersion of ~6 fs/THz, which only slightly broadens the ~250-fs pulses (spectral BW Δf ~1.38 THz) in our experiments. Δt_{min} can be less than **100 fs** in the 1.55-μm telecommunication band, but becomes longer for the near infrared pulses because of the larger GVD (~0.37 fs/THz/mm at 800-nm central wavelength).

The chirped QPM waveguide scheme can be even improved in the following aspects:

(a) Modulating the duty cycle of QPM grating periods to apodize the nonlinear coefficient strength $|d_{eff}(z)|$ and suppress the ripple of PM spectrum. This will reduce the spectral distortion in FROG traces and increase the spectral resolution of the pulse reconstruction.

(b) Using fiber-pigtailed waveguides to realize a fiber-based collinear SHG FROG setup (Fig. 5.1). In this scheme, the demanding free-space alignment (~1-μm displacement tolerance for input coupling) would be largely alleviated. No realignment is

required when the oven is activated to change the crystal temperature and central PM wavelength. A fiber stretcher driven by a PZT actuator can act as a delay dithering module, with no beam path fluctuation introduced by the dithering, and the dithered delay amplitude can be easily multiplied by winding more fibers around the stretcher. This configuration will largely facilitate the FROG trace acquisition.

(c) Realizing noncollinear SHG FROG by using chirped QPM waveguides with asymmetric Y-junctions mode sorters [60]. This new device was pioneered by our Stanford collaborators, which could realize the noncollinear FROG by waveguide devices. In Fig. 5.2, TM_{00} (even) mode launched into the broader even port is unchanged, but is converted into TM_{10} (odd) mode when launched into the narrow odd port of an asymmetric Y junction. If we view the scheme in the reciprocal direction, it shows that even and odd modes could be spatially separated by the asymmetric Y junction. This mode-converting property is very useful in separating self- and cross-terms in the collinear SHG process. As shown in Fig. 5.3, the even-mode FH pulses $a_1(t)$, $a_2(t-\tau)$ from the two arms of the Michelson interferometer enter the input Y junction (designed for 1550-nm band) through different ports. The upper $a_1(t)$ is converted into odd mode, while the lower $a_2(t-\tau)$ remains even. Therefore, the nonlinear polarizations originating from the self-square terms $P_{NL,11} \equiv a_1^2(t)$, $P_{NL,22} \equiv a_2^2(t-\tau)$ are both even functions, whereas that from cross term $P_{NL,12} \equiv a_1(t) \cdot a_2(t-\tau)$ becomes odd. All nonlinear polarization components are phase-matched by the QPM grating during the central interaction region and generate SH fields with the (even/odd) modes identical to the corresponding nonlinear polarizations. Then the output Y junction (designed for 775 nm) can spatially separate the even SH fields (driven by $P_{NL,11}$ and $P_{NL,22}$) from the odd SH field (driven by $P_{NL,12}$). As a result, we can measure the standard FROG trace (related to $P_{NL,12}$) at the odd output port without interference. Chirped QPM waveguide with asymmetric Y junctions can simplify the setup (no delay dithering), speed up the retrieval process, and reduce the measurement errors arising from non-ideal fringe and background suppression. The limited dynamic range (the ratio between maximum and minimum resolvable signal

levels) in collinear geometry can be largely increased by the background-free traces from this noncollinear configuration.

Finally, the ultrasensitive SHG FROG measurements can be combined with the pulse shaping technique to realize a versatile optical signal processor to dynamically generate arbitrary optical pulses, which would be very desirable in the applications when precisely controlled optical waveforms are involved.

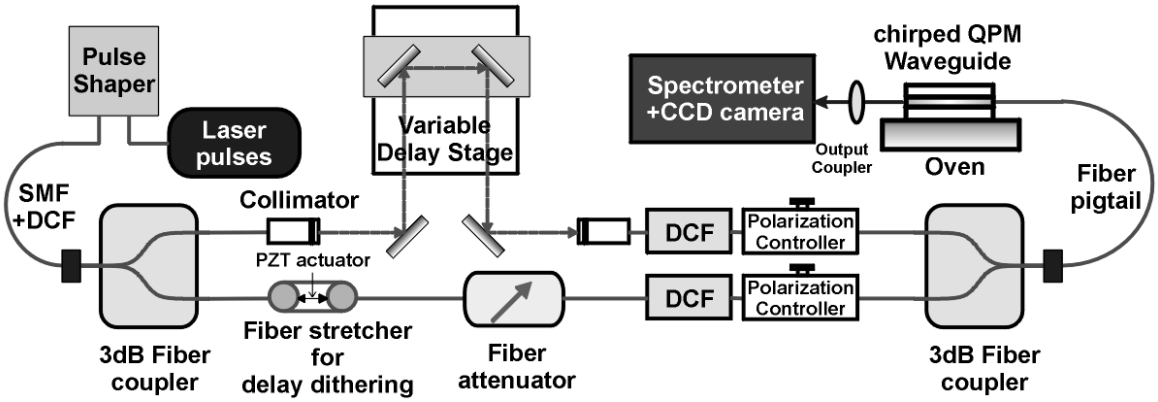

Fig. 5.1. Fiber-based collinear SHG FROG setup using fiber-pigtailed QPM $LiNbO_3$ waveguide. SMF: single mode fiber, DCF: dispersion compensating fiber, PZT: piezoelectric transducer.

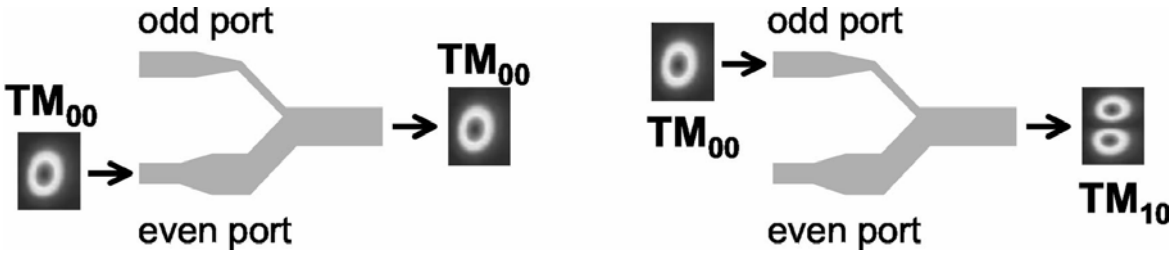

Fig. 5.2. Schematic diagram of mode conversion by asymmetric Y junction [60].

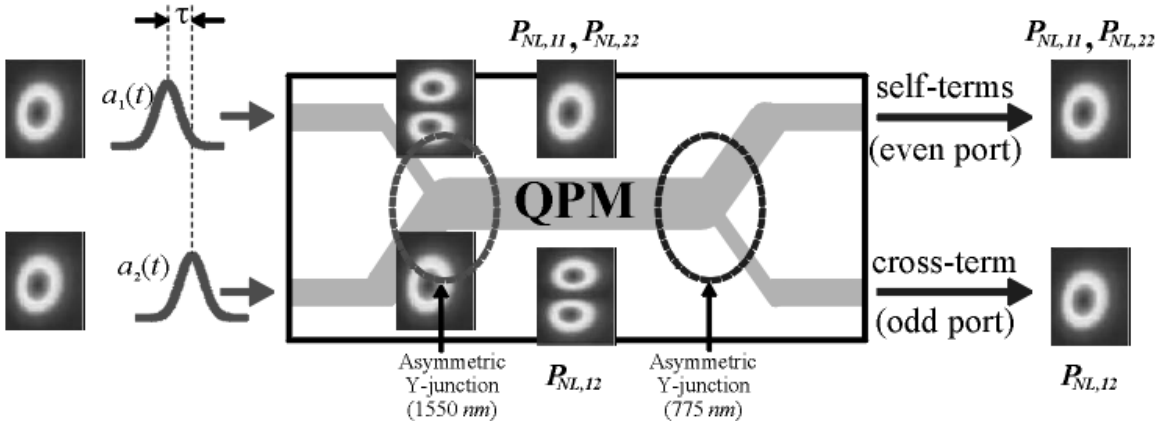

Fig. 5.3. Schematic diagram of mode sorting for spatially separating SH fields generated by self- and cross- nonlinear polarizations, where nonlinear polarization $P_{NL,ij} \equiv a_i(t) \cdot a_j(t-\tau)$. This double Y-junction device can realize non-collinear geometry for optical gating, intensity autocorrelation, and FROG measurements.

LIST OF REFERENCES

LIST OF REFERENCES

[1] B. C. Thomsen, D. A. Reid, R. T. Watts, L. P. Barry, J. D. Harvey, "Characterization of 40-Gbit/s pulses using a lithium niobate modulator at 1550 nm using frequency resolved optical gating", *IEEE Trans. on Instrum. Meas.*, **53**(1), pp. 186-191, 2004.

[2] Z. Jiang, D. S. Seo, S.-D. Yang, D. E. Leaird, R. V. Roussev, C. Langrock, M. M. Fejer, A. M. Weiner, "Four-user, 2.5-Gb/s, spectrally coded OCDMA system demonstration using low-power nonlinear processing", *J. Lightw. Technol.*, **23**(1), pp. 143-158, 2005.

[3] Z. Jiang, D. S. Seo, S.-D. Yang, D. E. Leaird, R. V. Roussev, C. Langrock, M. M. Fejer, A. M. Weiner, "Four-user, 10-Gb/s spectrally phase-coded O-CDMA system operating at ~30 fJ/bit", *IEEE Photon. Technol. Lett.*, **17**(3), pp. 705-707, 2005.

[4] N. Belabas, M. Joffre, "Visible-infrared two-dimensional Fourier-transform spectroscopy", *Opt. Lett.*, **27**(22), pp. 2043-2045, 2002.

[5] C. Dorrer, I. Kang, "Simultaneous temporal characterization of telecommunication optical pulses and modulators by use of spectrograms", *Opt. Lett.*, **27**(15), pp. 1315-1317, 2002.

[6] C. Dorrer, I. Kang, "Real-time implementation of linear spectrograms for the characterization of high bit-rate optical pulse trains", *IEEE Photon. Technol. Lett.*, **16**(3), pp. 858-860, 2004.

[7] C. Dorrer, "Investigation of spectrogram technique for the characterization of picosecond optical pulses", *in Proc. Conf. Optical Fiber Communications*, Mar. 2005.

[8] D.N. Fittinghoff, J.L. Bowie, J.N. Sweetser, R.T. Jennings, M.A. Krumbugel, K.W. DeLong, R. Trebino, I.A. Walmsley, "Measurement of the intensity and phase of ultraweak, ultrashort laser pulses", *Opt. Lett.*, **21**(12), 884-886, 1996.

[9] J.-Y. Zhang, A.P. Shreenath, M. Kimmel, E. Zeek, R. Trebino, S. Link, "Measurement of intensity and phase of attojoule femtosecond light pulses using optical-parametric-amplification cross-correlation frequency-resolved optical gating", *Opt. Express*, **11**(6), pp. 601-609, 2003.

[10] A.M. Weiner, “Ultrafast Optics”, course notes.

[11] A.M. Weiner, “Effect of group velocity mismatch on the measurement of ultrashort optical pulses via second harmonic generation”, *IEEE J. Quantum Electron.,* **19**(8), pp. 1276-1283, 1983.

[12] R. Trebino, *Frequency-resolved optical gating: the measurement of ultrashort laser pulses*. Boston, MA, USA: Kluwer Academic Publishers, 2000.

[13] J.D. Harvey, J.M. Dudley, D.C. Thomsen, L.P. Barry, “Ultra-sensitive autocorrelation using two photon absorption”, *in Proc. Conf. Optical Fiber Communications*, Mar. 1999.

[14] C. Xu, J.M. Roth, W.H. Knox, K. Bergman, “Ultra-sensitive autocorrelation of 1.5μm light with single photon counting silicon avalanche photodiode”, *Electron. Lett.,* **38**(2), pp. 86-88, 2002.

[15] J.M. Roth, T.E. Murphy, C. Xu, “Ultrasensitive and high-dynamic-range two-photon absorption in a GaAs photomultiplier tube”, *Opt. Lett.,* **27**(23), pp. 2076-2078, 2002.

[16] L.P. Barry, B.C. Thomsen, J.M. Dudley, J.D. Harvey, “Autocorrelation and ultrafast optical thresholding at 1.5μm using a commercial InGaAsP 1.3μm laser diode”, *Electron. Lett.,* **34**(4), pp. 358-360, 1998.

[17] P.-A. Lacourt, M. Hanna, J. M. Dudley, “Broad-band and ultrasensitive pulse characterization using frequency-resolved optical gating via four-wave mixing in a semiconductor optical amplifier”, *IEEE Photon. Technol. Lett.,* **17**(1), pp. 157-159, 2005.

[18] P.-A. Lacourt, J. M. Dudley, J-M. Merolla, H. Porte, J-P. Goedgebuer, W. T. Rhodes, “Milliwatt-peak-power pulse characterization at 1.55 μm by wavelength-conversion frequency-resolved optical gating”, *Opt. Lett.,* **27**(10), pp. 863-865, 2002.

[19] M. Dinu, F. Ouochi, “Amplitude sensitivity limits of optical sampling for optical performance monitoring”, *J. Optical Networking,* **1**(7), pp. 237-248, 2002.

[20] K.R. Parameswaran, J.R. Kurz, R.V. Roussev, M.M. Fejer, “Observation of 99% pump depletion in single-pass second-harmonic generation in a periodically poled lithium niobate waveguide”, *Opt. Lett.,* **27**(1), pp. 43-45, 2002.

[21] G. Imeshev, M. A. Arbore, M. M. Fejer, A. Galvanauskas, M. Fermann, D. Harter, “Ultrashort-pulse second-harmonic generation with longitudinally nonuniform quasi-

phase-matched gratings: pulse compression and shaping", *J. Opt. Soc. Amer. B*, **17**(2), pp. 304-318, 2000.

[22] S.-D. Yang, A. M. Weiner, K. R. Parameswaran, M. M. Fejer, "400-photon-per-pulse ultrashort pulse autocorrelation measurement with aperiodically poled lithium niobate waveguides at 1.55 μm", *Opt. Lett.*, **29**(17), pp. 2070-2072, 2004.

[23] S.-D. Yang, A. M. Weiner, K. R. Parameswaran, M. M. Fejer, "Ultra-sensitive frequency-resolved optical gating at 1.55 μm by aperiodically poled lithium niobate waveguides", *in Proc. Conf. Lasers and Elec. Optics*, May 2005.

[24] S.-D. Yang, A. M. Weiner, K. R. Parameswaran, M. M. Fejer, "Ultra-sensitive frequency-resolved optical gating by aperiodically poled $LiNbO_3$ waveguides at 1.5 μm", *Opt. Lett.*,: To be published, 2005.

[25] S.-D. Yang, Z. Jiang, A. M. Weiner, K. R. Parameswaran, M. M. Fejer, "Extremely low-power intensity autocorrelation and chromatic dispersion monitoring for 10-GHz, 3-ps optical pulses by aperiodically poled lithium niobate (A-PPLN) waveguide", *in Proc. Conf. Optical Fiber Communications*, Mar. 2005.

[26] S.-D. Yang, Z. Jiang, A. M. Weiner, K. R. Parameswaran, M. M. Fejer, "Ultrasensitive chromatic dispersion monitoring for 10-GHz pulse train by quasi-phase matched $LiNbO_3$ waveguides", *Electron. Lett.*, **41**(9), pp. 554-556, 2005.

[27] A. M. Weiner, "Femtosecond pulse shaping using spatial light modulators", *Rev. Sci. Instr.*, **71**(5), pp. 1929-1960, 2000.

[28] R. D. Nelson, D. E. Leaird, A. M. Weiner, "Programmable polarization-independent spectral phase compensation and pulse shaping", *Opt. Express*, **11**(15), pp. 1763-1769, 2003.

[29] F. G. Omenetto, A. J. Taylor, "Adaptive control of femtosecond pulse propagation in optical fibers", *Opt. Lett.*, **26**(12), pp. 938-940, 2001.

[30] Z. Zheng, A. M. Weiner, "Coherent control of second harmonic generation using spectrally phase coded femtosecond waveforms", *Chem. Phys.*, **267**, pp. 161-171, 2001.

[31] R.W. Boyd, *Nonlinear optics*, San Diego, CA, USA: Academics Press, 1992.

[32] H. Wang, A.M. Weiner, "Efficiency of short-pulse type-I second-harmonic generation with simultaneous spatial walk-off, temporal walk-off, and pump depletion", *IEEE J. Quantum Electron.*, **39**(12), pp. 1600-1618, 2003.

[33] A. K. Sharma, P. A. Naik, P. D. Gupta, “Simple and sensitive method for visual detection of temporal asymmetry of ultrashort laser pulses”, *Opt. Express,* **12**(7), pp. 1389-1396, 2004.

[34] R. Trebino, D.J. Kane, “Using phase retrieval to measure the intensity and phase of ultrashort pulses: frequency-resolved optical gating”, *J. Opt. Soc. Amer. A,* **10**(5), pp. 1101-1111, 1993.

[35] G. Taft, A. Rundquist, M.M. Murnane, I.P. Christov, H.C. Kapteyn, K.W. DeLong, D.N. Fittinghoff, M.A. Krumbugel, J.N. Sweetser, R. Trebino, “Measurement of 10-fs laser pulses”, *IEEE J. Sel. Topics Quantum Electron.,* **2**(3), pp. 575-585, 1996.

[36] K.W. DeLong, D.N. Fittinghoff, R. Trebino, “Practical issues in ultra-short laser-pulse measurement using frequency-resolved optical gating”, *IEEE J. Quantum Electron.,* **32**(7), pp. 1253-1264, 1996.

[37] C. Iaconis, I. A. Walmsley, “Spectral phase interferometry for direct electric-field reconstruction of ultrashort optical pulses”, *Opt. Lett.,* **23**(10), pp. 792-794, 1998.

[38] C. Iaconis, I. A. Walmsley, “Self-referencing spectral interferometry for measuring ultrashort optical pulses”, *IEEE J. Quantum Electron.,* **35**(4), pp. 501-509, 1999.

[39] L. Gallmann, D. H. Sutter, N. Matuschek, G. Steinmeyer, U. Keller, C. Iaconis, I. A. Walmsley, “Characterization of sub-6-fs optical pulses with spectral phase interferometry for direct electric-field reconstruction”, *Opt. Lett.,* **24**(18), pp. 1314-1316, 1999.

[40] K. W. DeLong, D. N. Fittinghoff, R. Trebino, B. Kohler, K. Wilson, “Pulse retrieval in frequency-resolved optical gating based on the method of generalized projections”, *Opt. Lett.,* **19**(24), pp. 2152-2154, 1994.

[41] D. Kane, “Real time measurement of ultrashort laser pulses using principal component generalized projections”, *IEEE J. Sel. Top. Quant. Electron.,* **4**(2), pp. 278-284, 1998.

[42] D. J. Kane, “Recent progress toward real-time measurement of ultrashort pulses”, *IEEE J. Quantum. Electron.,* **35**(4), pp. 421-431, 1999.

[43] B. Seifert, H. Stolz, M. Tasche, “Nontrivial ambiguities for blind frequency-resolved optical gating and the problem of uniqueness”, *J. Opt. Soc. Amer. B,* **21**(5), pp. 1089-1097, 2004.

[44] M. A. Arbore, O. Marco, M. M. Fejer, "Pulse compression during second-harmonic generation in aperiod quasi-phase-matching gratings", *Opt. Lett.,* **22**(12), 8pp. 65-868, 1997.

[45] M. A. Arbore, A. Galvanauskas, D. Harter, M. H. Chou, M. M. Fejer, "Engineerable compression of ultrashort pulse by use of second-harmonic generation in chirped-period-poled lithium niobate", *Opt. Lett.,* **22**(17), pp. 1341-1343, 1997.

[46] L. Gallmann, G. Steinmeyer, G. Imeshev, J.P. Meyn, M.M. Fejer, U. Keller, "Sub-6-fs blue pulses generated by quasi-phase-matching second-harmonic generation pulse compression", *Applied Physics B – Lasers and Optics*, **74**, pp. 237-243, 2002.

[47] J. G. Proakis, D. G. Manolakis, *Digital signal processing: principles, algorithms, and applications, 3rd ed.* Upper Saddle River, NJ, USA: Prentice-Hall, 1996.

[48] M. M. Fejer, G. A. Magel, D. H. Jundt, R. L. Byer, "Quasi-phase-matched second harmonic generation: tuning and tolerances", *IEEE J. Quantum Electron.*, **28**(11), pp. 2631-2654, 1992.

[49] L. E. Myers, R. C. Eckardt, M. M. Fejer, R. L. Byer, W. R. Bosenburg, J. W. Pierce, "Quasi-phase-matched optical parametric oscillators in bulk periodically poled $LiNbO_3$", *J. Opt. Soc. Amer. B*, **12**(11), pp. 2102-2116, 1995.

[50] K. R. Parameswaran, R. K. Route, J. R. Kurz, R. V. Roussev, M. M. Fejer, M. Fujimura, "Highly efficient second-harmonic generation in buried waveguides formed by annealed and reverse proton exchange in periodically poled lithium niobate", *Opt. Lett.,* **27**(3), pp. 179-181, 2002.

[51] R. V. Roussev, private communication.

[52] H. Ooi, K. Nakamura, Y. Akiyama, T. Takahara, T. Terahara, Y. Kawahata, H. Isono, G. Ishikawa, "40-Gb/sWDM transmission with virtually imaged phased array (VIPA) variable dispersion compensators", *J. Lightw. Technol.*, **20**(12), pp. 2196-2203, 2002.

[53] J.-X. Cai, K.-M. Feng, A. E. Willner, V. Grubsky, D. S. Starodubov, J. Feinberg, "Simultaneous tunable dispersion compensation of many WDM channels using a sampled nonlinearly chirped fiber Bragg grating", *IEEE Photon. Technol. Lett.,* **11**(11), pp. 1455-1457, 1999.

[54] I. Brener, M. H. Chou, E. Chaban, K. R. Parameswaran, M. M. Fejer, D. L. Pruitt, "Polarization-insensitive wavelength converter based on cascaded nonlinearities in $LiNbO_3$ waveguides," *Electron. Lett.,* **36**(1), pp. 66-67, 2000.

[55] K. W. DeLong, R. Trebino, J. Hunter, W. E. White, "Frequency-resolved optical gating with the use of second-harmonic generation", *J. Opt. Soc. Amer. B,* **11**(11), pp. 2206-2215, 1994.

[56] S. Wielandy, M. Fishteyn, B. Zhu, "Optical performance monitoring using nonlinear detection", *J. Lightw. Technol.*, **22**(3), pp. 784-793, 2004.

[57] S. Wielandy, M. Fishteyn, T. Her, D. Kudelko, C. Zhang, "Real-time measurement of accumulated chromatic dispersion for automatic dispersion compensation", *Electron. Lett.*, **38**(20), pp. 1198-1199, 2002.

[58] P. O'Shea, M. Kimmel, X. Gu, R. Trebino, "Highly simplified device for ultrashort pulse measurement", *Opt. Lett.*, **26**(12), pp. 932-934, 2001.

[59] Swamp Optics, http://www.swampoptics.com/

[60] J. R. Kurz, J. Huang, X. Xie, T. Saida, M. M. Fejer, "Mode multiplexing in optical frequency mixers", *Opt. Lett.,* **29**(6), pp. 551-553, 2004.

[61] L. Gallmann, G. Steinmeyer, D. H. Shutter, N. Matuschek, U. Keller, "Collinear type II second-harmonic-generation frequency-resolved optical gating for the characterization of sub-10-fs optical pulses", *Opt. Lett.,* **25**(4), pp. 269-271, 2000.

[62] I. Amat-Roldan, I. G. Cormack, P. Loza-Alvarez, "Measurement of electric field by interferometric spectral trace observation", *Opt. Lett.,* **30**(9), pp. 1063-1065, 2005.

[63] G. Stibenz, G. Steinmeyer, "Interferometric frequency-resolved optical gating", *Opt. Express,* **13**(7), pp. 2617-2626, 2005.

[64] A. Baltuska, M. S. Pshenichnikov, D. A. Wiersma, "Amplitude and phase characterization of 4.5-fs pulses by frequency-resolved optical gating", *Opt. Lett.*, **23**(18), pp. 1474-1476, 1998.

[65] A. Baltuska, M. S. Pshenichnikov, D. A. Wiersma, "Second-harmonic generation frequency-resolved optical gating in the single-cycle regime", *IEEE J. Quantum Electron.*, **35**(4), pp. 459-478, 1999.

[66] I. Amat-Roldan, I. G. Cormack, P. Loza-Alvarez, "Ultrashort pulse characterization with SHG collinear-FROG", *Opt. Express,* **12**(6), pp. 1169-1178, 2004.

[67] D. H. Jundt, "Temperature-dependent Sellmeier equation for the index of refraction, n_e, in congruent lithium niobate", *Opt. Lett.,* **22**(20), pp. 1553-1555, 1997.

VITA

VITA

Shang-Da Yang was born in Chiayi city, Taiwan (Republic of China) in 1975. He graduated from Chiayi Senior High School as a valedictorian in 1993. He received his B.S. degree in Electrical Engineering from National Tsing-Hua University, Hsinchu, Taiwan in 1997, and the M.S. degree in Electro-optical Engineering from National Taiwan University, Taipei, Taiwan in 1999, respectively. He then served the Army of Taiwan from 1999 to 2001, and earned the medal of single-precious-star for his contribution in constructing computer-based training system for mobile communication forces. He enrolled in the Ph.D. program of the School of Electrical and Computer Engineering, Purdue University, West Lafayette, Indiana since August 2001. His research interests focus on ultrasensitive optical pulse characterizations and optical code-division multiple access system. He won the first place in Sigma Xi Graduate Student Poster Competition of Purdue University in 2005, and has published 20 articles in conferences and journals. He is a student member of Optical Society of America and IEEE/LEOS.